META-ELECTROMAGNETICS FOR SCATTERING ENGINEERING AND WAVEFRONT MANIPULATIONS

A Dissertation

Presented to the Faculty of the Graduate School

of Cornell University

in Partial Fulfillment of the Requirements for the Degree of

Doctor of Philosophy

by

Aobo Chen

August 2021

META-ELECTROMAGNETICS FOR SCATTERING ENGINEERING AND WAVEFRONT MANIPULATIONS

Aobo Chen, Ph.D.

Cornell University 2021

The past twenty years have witnessed the advent and extensive study of metamaterials and, more recently, metasurfaces. These concepts have widely extended the range of available material properties and have enabled new or enhanced wave-propagation effects, from negative refraction and invisibility to light trapping and antenna beam shaping. In this dissertation, we use, or take inspiration from, metamaterials and metasurfaces to engineer the electromagnetic scattering and the wavefront of propagating waves for various relevant applications. We note that the "optical theorem" of scattering theory relates the concepts of scattering engineering and wavefront manipulation and provides a general framework for many of the ideas discussed in this dissertation. While this work is mostly theoretical and computational, considering the potential experimental demonstration of the proposed ideas, we focused on realistic material platforms and structures that can be fabricated with state-of-the-art technologies.

The first part of this dissertation is devoted to one of the most important scattering-engineering problems, namely, scattering/reflection reduction and invisibility. To demonstrate the practical potential of ideas borrowed from the field of metamaterials, we apply the concept of scattering-cancellation cloaking to design modified near-field probes that are effectively invisible and may enable non-perturbative near-field measurements. We then tackle a major chal-

lenge of linear passive cloaking devices, namely, their narrow bandwidth, and show that the "Bode-Fano limit" can be overcome through the design of active scattering-cancellation cloaks. We show that active cloaks indeed exhibit wider cloaking bandwidths; however, stability issues ultimately limit their performance. We then study another relevant application of the Bode-Fano bound in the context of broadband impedance matching of lossy films and solar cells, and we calculate the maximum solar power absorption for ultrathin solar cells made of different common materials and with arbitrary anti-reflection coatings.

The second part of this dissertation focuses on wavefront manipulation for two relevant applications. We first propose a general platform, based on metasurfaces in waveguide networks, for analog optical computing. Based on this idea, we design compact devices for fractional calculus, optical PID controllers, and equation solvers. Finally, we design dielectric nonlocal metasurfaces that implement the transfer function of free space over a much shorter length. Such space-compression metasurfaces provide a solution to realize compact, fully solid-state, planar structures for focusing, imaging, and magnification.

We believe the results of this dissertation may open many new opportunities for different engineering applications in electromagnetics, optics, and photonics.

BIOGRAPHICAL SKETCH

Aobo Chen received the B.S. and M.S. degrees in physical electronics from the University of Electronic Science and Technology of China (UESTC), Chengdu, China, in 2013 and 2016, respectively. He is currently a Ph.D. candidate in electrical and computer engineering at Cornell University, Ithaca, NY, USA.

His research interest includes electromagnetic theory, computational electromagnetics, signal and power integrity, metamaterials, scattering engineering, wavefront manipulations, solar cells, etc.

To the people who have loved, inspired, and supported me through all the years.

ACKNOWLEDGEMENTS

First of all, I would like to sincerely thank my PhD advisor, Prof. Francesco Monticone, for guiding and supporting me through these years. His passion for research and pursuit of excellence have had a great impact on me. Working with him, I not only accomplished this dissertation, but also got a thorough training on how to propose, analyze, and solve problems and how to present the results. I learned from him many ways of thinking, as well as practical research skills, including pushing parameters to the extreme, using simple lumped circuit models to rationalize complex problems, methods for effective debugging, and more. These gains will be invaluable in my future career.

It is my great honor to have Prof. Edwin Chihchuan Kan and Prof. Debdeep Jena as my committee members. I would like to thank them for their comments and suggestions on this dissertation. I also learned a lot from them about RF systems and solid state physics, which broadened my horizon.

I want to thank my colleagues and friends in Monticone research group, Dr. S. Ali Hassani Gangaraj, Kunal Shastri, Mohamed Ismail Abdelrahman, and Zeki Hayran, for a lot of mutual inspiration, discussions, and learning experiences.

I thank my friends in different fields related to my research, Dr. Xiaonan Hui, Zexuan Zhang, Yifei Geng, Xinyi Wang, and Dr. Chao Ning, who provided help in RF systems, mathematics, physics, discrete signal processing, and optimization.

The first semester in UT Austin was very impressive to me. I thank Prof. Andrea Alù for his wonderful course, which lead me into the field of metamaterials. I am still remembering the insightful discussions with him that helped me build intuitions. I thank Zhicheng Xiao and other colleagues in Alù research

group, who helped me at the start of my PhD.

I thank Dr. Sander Mann for collaborating on the solar cell project, and Dr. Felipe Bernal Arango and Prof. L. (Kobus) Kuipers for collaborating on the cloaked sensor project.

At last, I want to thank my parents and family members for their unconditional love and supports.

TABLE OF CONTENTS

LIST OF FIGURES

CHAPTER 1

INTRODUCTION

Section 1.1 defines the term ″meta-electromagnetics″ and briefly reviews the field of electromagnetic metamaterials. Section 1.2 explains the concepts of ″scattering engineering″ and ″wavefront manipulation″ and elucidates the relation between these two concepts through the optical theorem of scattering theory. Section 1.3 discusses some relevant physical limitations that play an important role in our research work. Section 1.4 outlines the organization of this dissertation.

1.1 What is meta-electromagnetics?

The term ″meta-electromagnetics″ first appeared in Ref. [3], used by Prof. Nader Engheta, one of the pioneers of the field of complex media and metamaterials. In this dissertation, ″meta-electromagnetics″ generally indicates the sub-field of electromagnetics, where metamaterials or inspirations from the concept of metamaterials are used for the analysis and design of electromagnetic wave propagation phenomena for potential engineering applications.

The basic laws governing classical electromagnetic fields and wave propagation are the Maxwell Equations. The standard macroscopic form of Maxwell equations is [4, 1]

$$\nabla \times \mathbf{H} = \mathbf{J} + \frac{\partial \mathbf{D}}{\partial t}, \tag{1.1}$$

$$\nabla \times \mathbf{E} = \frac{\partial \mathbf{B}}{\partial t}, \tag{1.2}$$

$$\nabla \cdot \mathbf{B} = 0, \tag{1.3}$$

$$\nabla \cdot \mathbf{D} = \rho, \tag{1.4}$$

where **H** and **E** are the magnetic and the electric fields (sometimes called magnetic and electric field strengths); **B** and **D** are the magnetic and electric flux densities; **J** and ρ are the electric current and charge densities. In free space, the field flux densities **B** and **D** and the field strengths **H** and **E** are related by

$$\mathbf{B} = \mu_0 \mathbf{H}, \tag{1.5}$$

$$\mathbf{D} = \epsilon_0 \mathbf{E}, \tag{1.6}$$

where μ_0 and ϵ_0 are the magnetic permeability and the electric permittivity of free space, respectively. In media, the field flux densities and the field strengths are related by more general constituent relation, which in the most general case can be written as $\mathbf{B} = f(\mathbf{E}, \mathbf{H}, \mathbf{r}, t)$ and $\mathbf{D} = g(\mathbf{E}, \mathbf{H}, \mathbf{r}, t)$, where f and g are generic functions of the field strengths, the position vector **r**, and the time variable t. Constituent relations are said to be *linear* if the functions f and g are linear in the fields [5], *passive* if no electromagnetic energy is generated, *causal* if a generic output cannot temporally precede a generic input, *reciprocal* if exchanging source and detector leads to the same output to input ratio [6], *temporal/frequency dispersive* if the temporal impulse response is not a delta function in time [4, 1], *spatially dispersive (nonlocal)* if the spatial impulse response is not a delta function in space [7], *anisotropic* if the functions f and g depend on the field polarization [4, 1], *chiral (bi-isotropic)* if the functions f and g depend on both **E** and **H** (magneto-electric coupling) [8], *bi-anisotropic* if the material is both chiral and anisotropic, *time-varying* if the functions f and g themselves change with time [9, 10], *inhomogoeneous* if the functions f and g themselves change in space, etc.

Among this broad range of possible properties that electromagnetic materials can have, some of them can be readily found in nature (e.g., anisotropic

crystals or chiral materials are common), while others are only accessible in engineered materials, or metamaterials [11]. In artificial metamaterials with complex properties, electromagnetic fields and waves exhibit a variety of effects not commonly found in nature, with great opportunities for scientific explorations and engineering applications. As some notable examples, in the past two decades, electromagnetic metamaterials have been extensively studied to realize super-resolution imaging [12, 13], invisibility cloaking [14, 14, 15, 16], light trapping and bound states in continuum [17, 18, 19], and have led to the development of entire sub-fields, including *non-Hermitian photonics* which leverage the peculiar wave physics near "exceptional points" [20], *metasurfaces and metalenses* to control light with thin patterned membranes [21, 22, 23], *topological photonics*, which translates relevant concepts of topological condensed-matter physics to the photonics domain [24, 25, 26, 27], *space-time metamaterials* using time as an additional degree of freedom to, among other things, break reciprocity constraints [9, 10], etc.

Within this broad context, in this dissertation, we have studied the general problems of scattering engineering and wavefront manipulations using suitable structures composed of dielectric and plasmonic materials and, in some cases, gain media, with various goals for different engineering applications. We focus on materials that are readily found in nature, but we get physical insights, intuitions and design inspirations from the field of metamaterials. The materials considered in this dissertation are linear, passive / active, reciprocal, frequency dispersive, local, isotropic, non-chiral, time-invariant, and non-magnetic. Under these assumptions, it is convenient to study the electromagnetic problem in the frequency domain. The relation between the frequency-domain electric flux density $\mathbf{D}$ and the electric field strength $\mathbf{E}$ can be written as a simple product

with the frequency domain permittivity:

$$\mathbf{D}(\omega) = \varepsilon(\omega)\mathbf{E}(\omega), \tag{1.7}$$

where ω is the radian frequency. The permittivity $\varepsilon(\omega)$ of a material (or metamaterial) can generally be expressed in the form of a multi-oscillator Lorentz model [1]

$$\varepsilon(\omega) = 1 + \sum_i \frac{f_i \omega_{pi}^2}{\omega_{0i}^2 - \omega^2 + j\omega\gamma_i}, \tag{1.8}$$

where ω_{0i} and γ_i are the resonant frequency and the resonance linewidth, respectively, for the i-th resonator (corresponding to some material resonance at the mesoscopic, molecular, or atomic level); f_i is the resonator strength, and ω_{pi}^2 is the plasma frequency. When f_i is positive (negative), the medium is passive (active). The frequency domain permittivity is generally a complex number whose real and imaginary part are associated with, among other things, the stored electromagnetic energy (with some subtleties in the dispersive case) and the absorbed/gained energy in the material, respectively. Moreover, real and imaginary parts of $\varepsilon(\omega)$ are not independent functions due to the analytic properties of causal, bounded, transfer functions, as discussed in Section 1.3.1.

1.2 Scattering engineering and wavefront manipulation

When a material is uniform in the spatial domain, the allowed electromagnetic modes are the eigensolutions of the wave equation in the homogeneous media, i.e., propagating and evanescent plane waves. However, when there are inhomogeneities in the permittivity distribution, the electromagnetic wave will be scattered by these inhomogeneities, which therefore act as scatterers, as shown in Fig. 1.1.

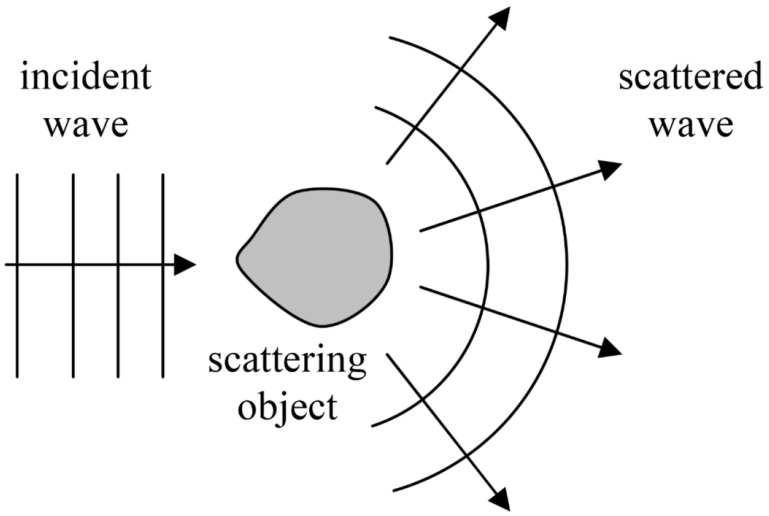

Figure 1.1: Schematic of a generic scattering problem [1].

Suppose the incident wave is a propagating plane wave (if not, we can expand the incident wave into a weighted sum of plane waves [28] and use the superposition principle to find the total field). Without loss of generality, we can write the electric field of the incident wave as

$$\mathbf{E}_{inc} = \hat{\mathbf{x}} E_0 e^{-j\mathbf{k}\cdot\mathbf{r}}, \tag{1.9}$$

where E_0 is the amplitude, $\mathbf{k}$ is the wave vector (spatial frequency or linear momentum of the wave), and $\mathbf{r}$ is the position vector. If the size of the scattering object is finite, we can draw a spherical surface enclosing the scatterer. Then, the electric field of the scattered wave, in the region outside the sphere (assumed homogeneous) can always be expressed as a superposition of weighted spherical harmonics [29]

$$\mathbf{E}_s = E_0 \left[\sum_{n=1}^{\infty} c_n^{TM} \nabla \times \nabla \times \left(\mathbf{r} \psi_n^1 \right) - j\omega\mu_0 \sum_{n=1}^{\infty} c_n^{TE} \nabla \times \left(\mathbf{r} \psi_n^1 \right) \right], \tag{1.10}$$

where ψ_n^m are the scalar spherical harmonics; c_n^{TM} and c_n^{TE} are the scattering coefficients of the TM (to $\hat{\mathbf{r}}$) modes and the TE (to $\hat{\mathbf{r}}$) modes, respectively. Ana-

lytical solutions exist for the scattering coefficients of canonical configurations (e.g., spheres and cylinders), whereas for more general cases numerical methods may be needed, such as the method of moments applied to a volume integral equation formulation of the scattering problem [30].

Based on the scattering coefficients, c_n^{TE} and c_n^{TM}, we can then readily calculate the total scattering cross section of the scattering object [29]

$$\sigma_{scat} = \frac{\lambda_0^2}{2\pi} \sum_{n=1}^{\infty} (2n+1) \left(\left| c_n^{TE} \right|^2 + \left| c_n^{TM} \right|^2 \right), \tag{1.11}$$

the forward scattering cross section [29]

$$\sigma_{fw} = \frac{\lambda_0^2}{4\pi} \left| \sum_{n=1}^{\infty} (2n+1) \left(c_n^{TE} + c_n^{TM} \right) \right|^2, \tag{1.12}$$

the extinction cross section [29]

$$\sigma_{ext} = -\frac{\lambda_0^2}{2\pi} \sum_{n=1}^{\infty} (2n+1) \operatorname{Re} \left[c_n^{TE} + c_n^{TM} \right], \tag{1.13}$$

and the absorption cross section [29]

$$\sigma_{abs} = \sigma_{ext} - \sigma_{scat}, \tag{1.14}$$

where λ_0 is the free-space wavelength. All this quantities are in units of m^2 and provide a measure of how strongly the scatterer perturbs the incident energy flow. Due to the wave properties of light, all these cross section are not bounded by the geometrical cross section of the scatterer itself: they can be much smaller or much larger depending on the specific geometry and material composition of the scatterer (an interesting example is the case of a single two-level atom, which has a scattering cross section, near resonance, much larger than its actual size [31].)

One of the most important result of scattering theory is the fact that the extinction cross section, σ_{ext}, is related to the normalized scattering amplitude po-

larized in parallel with the impinging field in the forward direction, which is known as the *optical theorem* [4, 1, 32, 29]

$$\sigma_{ext} = -\frac{\lambda_0^2}{\pi} \operatorname{Im}\left[s_\theta\left(0,0\right)\right], \tag{1.15}$$

where $s_\theta\left(0,0\right)$ means the θ component of the normalized scattering amplitude at $\theta = 0$ and $\phi = 0$. An intuitive explanation of this theorem is that the shadow cast by an object (i.e., the forward scattering) must be proportional to the total energy removed from the incident wave, either scattered in other directions or absorbed (i.e., the extinction cross section).

This dissertation work is articulated around different projects, related to the analysis and design of wave propagation in complex structures and (meta-) materials, which can be seen as different forms of "scattering engineering" in extreme or anomalous ways. Through the optical theorem, these activities can also be seen as forms of "wavefront manipulations" as they involve the design of structures to engineer the forward scattering, and therefore the transmitted wavefront. However, in a narrower sense, we use the term "scattering engineering" specifically for the analysis and design of the scattering properties of a 3-D object, and "wavefront manipulations" for the engineered output of planar metasurfaces.

We would also like to note that the optical theorem, relating the topics of scattering engineering and wavefront manipulations in this dissertation, is very general and widely applicable since it directly originates from the conservation of energy, for classical wave scattering, or from the conservation of probability, in the quantum-mechanical scattering case [33, 34]. Many of the ideas and designs put forward in this dissertation can therefore be extended and translated to different realms of classical and quantum wave physics.

1.3 Physical limitations in scattering engineering and wavefront manipulation

As mentioned in the previous sections, the vast range of properties that can be implemented with electromagnetic (meta)materials enables us to control and tailor the flow of electromagnetic waves in new and anomalous ways. Clearly, however, there are certain physical bounds that ultimately limit what is possible and constrain the ability to realize arbitrary forms of scattering engineering and wavefront manipulation. A major theme of this dissertation has been the analysis of the relevant physical limitations in different areas of meta-electromagnetics, as well as novel efforts to break, or bypass, these physical limitations by relaxing their basic assumptions, with the general goal to enable new possibilities. In this section, we outline two of the most important physical limitations related to our works in the following chapters.

1.3.1 Causality: Kramers-Kronig relations

Consider the permittivity of a linear frequency-dispersive isotropic material, $\varepsilon(\omega)$, which is a complex function of frequency. As a physically realizable function, $\varepsilon(\omega)$ must be the Fourier transform of a causal function. Indeed, in time domain the system's output (material polarization or electric flux density) should be zero before the input (electric field) is applied. As a result, the temporal impulse response of the system must be a unilateral function, identically zero along the negative time axis. This has important consequences for the analytic properties of its Fourier transform. In particular, in frequency domain, the re-

gion of convergence of $\varepsilon(\omega)$ should be the right-half plane to the right most pole, in the complex plane of the Laplace variable $s = \sigma + j\omega$. If the system is stable, the function is therefore analytic in the entire half-plane to the right of the imaginary axis. Then, analyticity of $\varepsilon(\omega)$ and its bounded nature (in the sense of square integrability) requires that its real and imaginary parts satisfy so-called "Kramers-Kronig relations" (also known as Hilbert transforms or Plemelj formulas) [4, 1]

$$\mathrm{Re}\left[\varepsilon(\omega)\right] = 1 - \frac{2}{\pi}\,\mathrm{PV}\int_0^\infty \frac{\Omega\,\mathrm{Im}\left[\varepsilon(\omega)\right]}{\Omega^2 - \omega^2} d\Omega, \tag{1.16}$$

$$\mathrm{Im}\left[\varepsilon(\omega)\right] = \frac{2}{\pi}\,\mathrm{PV}\int_0^\infty \frac{\omega\,\mathrm{Re}\left[\varepsilon(\omega)\right] - 1}{\Omega^2 - \omega^2} d\Omega, \tag{1.17}$$

where PV denotes the Cauchy principal value integral. Interestingly, similar relations are also valid for the impedance function in circuit theory, a result that is known as the Foster's reactance theorem [35].

Kramers-Kronig relations have many crucial implications on the permittivity function in frequency domain, and related quantities, which further set limitations on the ability to engineer the scattering properties of a given physical object. First, the real and imaginary parts of the frequency-domain permittivity function are not independent with each other. If we know the real (imaginary) part over all frequencies, we readily know the imaginary (real) part (or an approximation if the integrals are truncated on a finite frequency range, as usually done in practice). Typically, causal and linear permittivity functions follow a multi-resonator Lorentz model, as shown in Eq. (1.8), which may include Drude terms (Lorentz terms with resonant frequency set to zero) in the presence of free electrons. Second, if the medium is *passive*, then in a low-loss frequency window, a suitable differentiation of the Kramers-Kronig relations shows that the

following inequalities hold [7, 36]

$$\frac{\partial \varepsilon(\omega)}{\partial \omega} \geq 0, \quad \text{and} \quad \frac{\partial \varepsilon(\omega)}{\partial \omega} \geq \frac{\varepsilon_0 - \varepsilon}{\omega}, \tag{1.18}$$

which imply that $\varepsilon(\omega)$ must have a positive non-zero slope in any low-loss window (normal dispersion) and, for any permittivity value below ε_0, the slope has a positive lower bound. This is one of the fundamental limits that hinder broadband passive invisibility cloaking [16, 36], as we will discuss in Chapter 3 in details.

1.3.2 Bode-Fano limit of broadband impedance matching and its validity for non-reciprocal matching

Another important theoretical limit that is relevant for this dissertation work is the Bode-Fano limit for broadband impedance matching in circuit/microwave theory [37, 38, 39]. With reference to the schematic in Fig. (1.2), for a physically realizable load, described by an impedance function with a finite number of zeros and poles in the complex Laplace plane, there is a limit on the reflection coefficient Γ, for a generic linear, causal and reactive (i.e., lossless) matching network, which can be expressed as an integral inequality

$$\int_0^\infty \ln \frac{1}{|\Gamma|} \, \mathrm{d}\omega \leq \text{constant}. \tag{1.19}$$

where the right-hand-side depends uniquely on the properties of the load and is instead independent of the matching network. The Bode-Fano limit can then be readily used to determine the maximum possible bandwidth over which a specified level of reflection can be attained. We note that this limit can also be applied in optics to determine the maximum bandwidth of, for example,

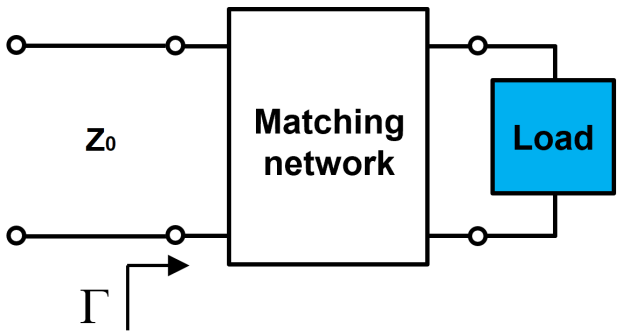

Figure 1.2: Illustration of the problem of impedance matching between a load and an input transmission line or source impedance through a generic matching network. The Bode-Fano limit of broadband impedance matching applies to problems of this type if the matching network is linear, causal, and reactive (matching through interference, not absorption).

anti-reflection coatings, or any other device that suppress the reflection through an interference effect (not absorption, since the matching network in Fig. (1.2) needs to be lossless).

While the Bode-Fano limit will be further discussed and used in Chapters 3 and 4 of this dissertation, here we take the opportunity to discuss in more details the scope of applicability of this bound for different classes of matching networks. We also believe this is relevant and instructive to understand better the main assumptions of this important result. The derivation of the Bode-Fano limit in Fano's original paper [38] assumes a reciprocal lossless matching network. However, in recent years, increasing attention has been devoted to wave propagation in nonreciprocal systems [40, 9, 10, 25], including in the context of invisibility cloaking [41]. Thus, one may wonder whether the Bode-Fano limit is still valid when the matching network is nonreciprocal. To answer this relevant question, here we prove the validity of this limit for any lossless nonreciprocal

matching network, under the conditions of linearity, causality, passivity, and time-invariance.

Our main idea is to show that the two key intermediate results in Fano's derivation [38] remain true when reciprocity is broken. Following Fano's original work, the impedance function of a physically realizable load is represented (Darlington representation [42]) as a purely-reactive network N′, terminated in a pure resistor, which can be taken as equal to unity. The load is driven by a Thevenin source with 1 Ω impedance. To minimize reflection, a lossless matching network N″ is inserted between the Thevenin source and the load. Different from Fano's original derivation, here we allow N″ to be non-reciprocal. As illustrated in Fig. 1.3, the cascade connection of networks N′ and N″ form network N, which is, therefore, lossless and nonreciprocal as well. The scattering parameters of the networks N, N′ and N″ are expressed as

$$S = \begin{pmatrix} \Gamma_1 & t_{12} \\ t_{21} & \Gamma_2 \end{pmatrix}, \tag{1.20}$$

$$S' = \begin{pmatrix} \Gamma'_1 & t' \\ t' & \Gamma'_2 \end{pmatrix}, \tag{1.21}$$

$$S'' = \begin{pmatrix} \Gamma''_1 & t''_{12} \\ t''_{21} & \Gamma''_2 \end{pmatrix}, \tag{1.22}$$

The Bode-Fano limit sets restrictions on the physical realizability of $|\gamma_2|$, i.e., on the amplitude of the reflection coefficient of the matched load.

Since the network N is lossless but not reciprocal, the scattering matrix of N is unitary but not symmetric. An arbitrary unitary matrix can be expressed as

$$\begin{pmatrix} a & b \\ -e^{j\varphi}b^* & e^{j\varphi}a^* \end{pmatrix}, \ |a|^2 + |b|^2 = 1, \tag{1.23}$$

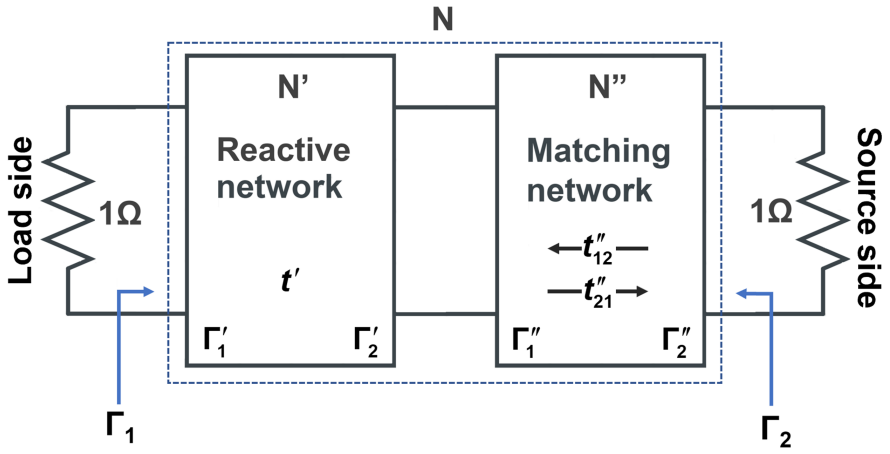

Figure 1.3: Circuit topology for the derivation of the Bode-Fano limit, for either a reciprocal or nonreciprocal lossless matching network.

which means that the amplitude of Γ_2 is equal to that of Γ_1, whereas there may be a significant phase difference. This is the first important point of this derivation. Indeed, the Bode-Fano limit is expressed only on the amplitude of the reflection coefficient, while the phase is unconstrained. The equality of the amplitudes of Γ_2 and Γ_1 allows us to turn the network end to end and to regard the limit on the amplitude of Γ_1 as the limit on the amplitude of Γ_2, just as done in Fano's paper. An arbitrary phase difference between these reflection coefficients is not important.

Then, we write the expression of Γ_1 in terms of the scattering parameters of N′ and N″:

$$\Gamma_1 = \Gamma'_1 + \Gamma''_1 \frac{(t')^2}{1 - \Gamma'_2 \Gamma''_1}, \tag{1.24}$$

which remains the same independently of the reciprocal or non-reciprocal nature of the matching network. This is the second important result of the derivation, which allows us to use the intrinsic properties of the load, N′, to derive constraints on the overall network N. Specifically, as recognized by Fano, if t' has a zero of multiplicity n, then Γ_1 and its first $2n - 1$ derivatives are equal,

respectively, to Γ_1' and its corresponding derivatives; hence, these transmission zeros can be used to derive realizability conditions on the reflection coefficient independently of the matching network.

These two important results allow us to follow the rest of Fano's derivation, based on Cauchy's integral relations, without any modification, and obtain the same limits on the amplitude of Γ_1. This derivation shows that, as a result of energy conservation in lossless systems (unitarity of S matrix), the Bode-Fano limit remains valid also for lossless nonreciprocal matching networks.

We should also stress that, if the nonreciprocal matching network was, instead, lossy, as in the case of an electromagnetic isolator used for impedance matching, the Bode-Fano limit would not apply, as it is invalid for any type of absorbing matching strategy, reciprocal or not. Moreover, we also note that if reciprocity was broken via temporal modulation, conventional Bode-Fano limit would apply only if the system could still be modeled with a unitary scattering matrix (which is usually not possible since a time-varying system generates different frequencies, corresponding to additional network ports and decaying channels).

1.4 Organization of the dissertation

After the brief Introduction provided in this chapter, the next two chapters are devoted to one of the most important scattering-engineering problems: the problem of scattering reduction and invisibility. Chapter 2 presents our work on applying ideas from metamaterial invisibility cloaks (scattering cancellation cloaking) to the problem of making the probe of a near-field scanning optical

microscope effectively invisible (without preventing its ability to measure) with the goal of enabling non-perturbative near-field measurements. This invisibility effect is achieved by modifying an aperture probe by cutting slits on its aluminum shell. Specifically, by modulating the length of the slits, we managed to control the electric dipole polarizability of the probe tip.

Chapter 3 covers the general problem of broadband scattering cancellation cloaking, and discusses our efforts to use active media to break the Bode-Fano bounds for passive cloaking. When the passivity assumption is relaxed, it becomes crucial to assess whether the system remains stable (absence of unbounded oscillations). Interestingly, we found that, while the bandwidth may be broadened with respect to the passive case, stability issues limit the maximum bandwidth of the cloaking effect, and we determined an approximate, yet quantitative, limit of the cloaking bandwidth.

Chapter 4 presents another relevant application of the Bode-Fano bound in a different context. We analyze the problem of broadband impedance matching of lossy films, e.g., ultra-thin solar cells, covered by arbitrary anti-reflection coatings. We calculated the maximum solar power absorption for ultrathin solar cells made of different common materials.

The second part of this dissertation is devoted to our work on wavefront manipulation with novel metasurfaces for two relevant applications. Chapter 5 proposes a compact analog optical computing platform based on metasurfaces in waveguide networks. With the proposed platform, we show design examples to perform fractional calculus of an arbitrary order, to calculate a weighted sum of proportional-integral-derivative (PID) operations an input function, and to solve fractional calculus equations.

In Chapter 6, we discuss our design of dielectric nonlocal metasurfaces that implement the transfer function of free space over a much shorter length. This allows compressing arbitrarily long free-space volumes and miniaturize complex optical systems. We derive a fundamental trade-off between the length of compressed free space and the operating angular range, and we then propose a solution to relax this trade-off inspired by coupled-resonator-based band-pass microwave filters. Our space-compression metasurfaces provide a solution to realize compact, fully solid-state, planar structures for focusing, imaging, and magnification.

Chapter 7 concludes this dissertation and offers an outlook on the future of this area of research.

CHAPTER 2

MINIMALLY PERTURBATIVE NEAR-FIELD SENSORS BASED ON SCATTERING-CANCELLATION CLOAKING

2.1 Introduction

In this section, we first briefly review the two most popular approaches to reduce the total scattering cross section of an object and achieve invisibility using metamaterials, i.e., transformation-based cloaking and scattering-cancellation cloaking. Then, by applying and adapting the scattering cancellation approach, we propose a fabrication-compatible technique to cloak the probe of a near-field scanning optical microscope (NSOM) with the goal of minimizing scattering-induced perturbations and artifacts during measurements [43].

2.2 Two types of invisibility cloaks

The advent of metamaterials at the beginning of the century has enabled great progress in the quest for electromagnetic invisibility, a topic that has attracted huge attention and research efforts in the past two decades [11, 44, 14, 45, 46, 47, 15, 48, 49, 50, 51, 52, 43, 53, 54, 55, 56, 57, 58, 59, 60, 61, 62, 16, 63, 64, 65]. By covering an object with a suitably engineered invisibility cloak, the total scattering cross section (SCS) of the object can be drastically suppressed, making the cloaked object invisible for any observer and illumination [44]. Based on the mechanism of operation, the most popular cloaking strategies can be divided into two main categories, i.e., transformation-based cloaking [14, 45, 46, 47] and

scattering-cancellation cloaking [15, 48, 49, 50]. Transformation-based schemes seek to redirecting an incident electromagnetic wave around a scatterer using suitably-designed inhomogeneous and anisotropic permittivity and permeability distributions [14, 45, 46, 47]. In principle, this strategy works perfectly at a single frequency, independently of the size of the scatterer. However, transformation-optics cloaks are very difficult to implement in practice. In addition, typical cloaks of this type completely shield the scatterer from the incident field, making it essentially "blind" to the external environment. In contrast, scattering-cancellation cloaking techniques seek to suppress the dominant scattering components in a multipolar expansion of the scattered field, using either homogeneous isotropic plasmonic layers [15, 48] or thin frequency-selective surfaces or metasurfaces [49, 50]. Therefore, drastic scattering suppression can be obtained, with much lower system complexity, for objects that are smaller or comparable in size to the wavelength. Most importantly, because the scatterer covered by the cloak is still polarized by the incident field, scattering-cancellation cloaking can be employed to realize invisible sensors [51, 52, 43] and low-scattering antennas [44, 53, 54, 55, 56]. In this chapter, we apply the concept of scattering cancellation to design cloaked NSOM probes with minimized scattering.

2.3 Cloaked near-field probe design

2.3.1 Overview of near-field scanning optical microscopes

Subwavelength optical imaging at the nanoscale is widely needed in different scientific scenarios, e.g., to detect structures on the surface of cells, and to study nanophotonic devices. Different schemes have been developed in recent decades to break Abbe's diffraction limit of optical imaging, among which two main strategies exist that only require linear media: (i) a perfect negative-refraction lens [12] allows recovering (enhancing) the near-field information (evanescent components) in the far field, whereas (ii) a near-field scanning optical microscope (NSOM) [66] allows obtaining the near-field information directly by introducing a near-field probe that converts evanescent waves into propagating waves. A lossless negative-index lens works perfectly in theory (no resolution limits), but its performance degrades rapidly when considering practical implementations with any level of losses or imperfections [67, 68]. The concept of near-field probes first appeared at the beginning of the 20th century, when it was proposed by Synge based on suggestions from Einstein [69]. Thanks to advances in nanotechnology, near-field probes are now a mature technology and NSOM systems have been used in many different scenarios [70, 71, 72, 73, 74, 75, 76, 77, 78, 79, 80, 81]. There are two main classes of probe tips, i.e., aperture type and apertureless type. For an aperture-type probe, an aperture at the end of the tip is used to collect the electromagnetic field of an illuminated sample (converting the evanescent near-field into guided modes propagating in a tapered optical fiber) and/or to illuminate a surface under study. In contrast, an apertureless tip is designed as a small-volume high-efficiency

scatterer to convert the evanescent near-field into propagating scattered waves that are then collected in the far-field. Although an apertureless tip can usually provide higher spatial resolution for sub-diffractive imaging, aperture-type tips require lower system complexity and have higher signal-to-noise ratio (the signal is directly collected by the tapered optical fiber).

Despite decades of developments, aperture-type probes still suffer from basic limitations that strongly affect their performance: in collection mode, when the probe tip is brought close to an illuminated structure under study, the field distribution pattern is significantly disturbed by the tip itself [82, 83]. The perturbation originates directly from the electromagnetic scattering of the tip interacting with the field distribution under study, changing the original field distribution pattern. Since the size of probe tip is much smaller than the operating wavelength, which results in subwavelength resolution, the electric dipole moment induced on the tip dominate the scattering effect [4]. Therefore, our goal is to control and suppress the dipolar scattering of the tip to a large extent, while, at the same time, preserving the ability of the tip to measure fields (namely, the external sources should be allowed to polarize the tip and induce internal fields).

A solution to this problem was proposed in [52, 84] for aperture-type probes and in [85] for apertureless probes based on the concept of "cloaked sensors" [51, 86]: by surrounding the tip with a plasmonic shell with suitable negative permittivity, the total dipole moment of the cloaked object is strongly suppressed, while the internal fields are nonzero. As a result, the tip is able to measure a given field distribution with minimal perturbations. Unfortunately, however, low-loss plasmonic materials with the desired negative permittivity can-

not be readily found in certain frequency ranges, such as at infrared frequencies where most near-field probes are actually used. To overcome this problem, here we present a novel and general method to make near-field probes invisible at infrared frequencies, without using any plasmonic materials or metamaterials. To obtain this effect, we control the electric dipole polarizability and impedance of the probe by suitably carving slits on its aluminum shell, as detailed in the following section. Interestingly, both resonant scattering enhancement and scattering suppression are observed for different slit lengths. At the cloaking condition, the scattering of the probe tip is drastically suppressed, even if substantial power is captured by the probe and delivered to the "load" (i.e., the detectors in the far-field). This "cloaking"' method is feasible with current nanofabrication technology [76] and can readily be implemented to engineer the scattering of optical nano-probes, and achieve advanced optical imaging at deeply subwavelength scales [43].

2.3.2 Slitted tip to suppress scattering

In a typical aperture-type NSOM probe, the tip of a tapered optical fiber is covered by an aluminum shell, with a subwavelength aperture at the end that captures the fields as the tip is scanned above the illuminated sample. When the tip is illuminated frontally, an electric dipole moment is induced on the aperture

$$\mathbf{p} = \alpha_e \mathbf{E}_{loc}, \tag{2.1}$$

where is the polarizability of the tip for the considered incident polarization, and $\mathbf{E}_{loc}$ is the local electric field intensity. Since the electric polarization current $j\omega\mathbf{p}$ (under an $e^{j\omega t}$ time-harmonic convention) is proportional to the local electric field intensity, we can regard the polarizability as an admittance relating the

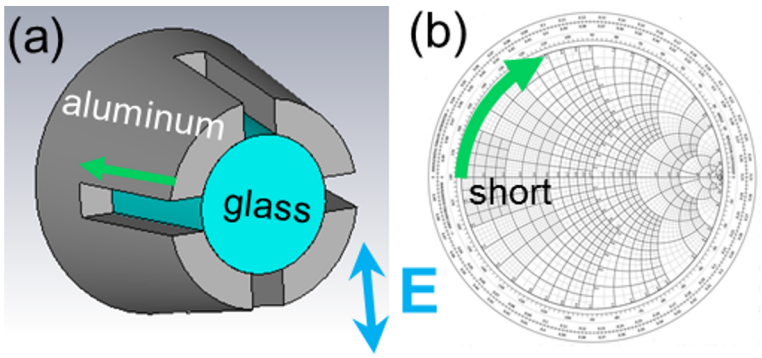

Figure 2.1: Schematic of the considered 'slitted' near-field probe tip and heuristic explanation based on the Smith chart. The slits qualitatively act as shorted transmission lines for the incident electric field perpendicular to them. By controlling the slit length (green arrow), the input reactance can be controlled and tailored to compensate the capacitive aperture.

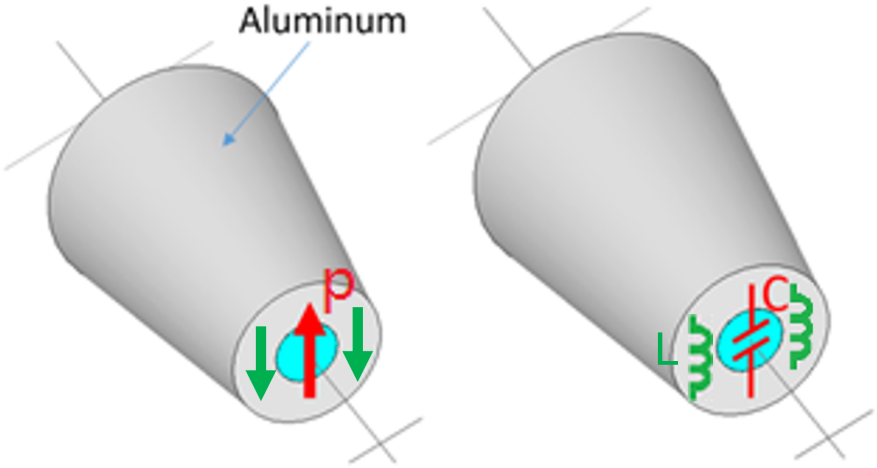

Figure 2.2: Schematic of cloaked NSOM tip based on scattering cancellation cloaking

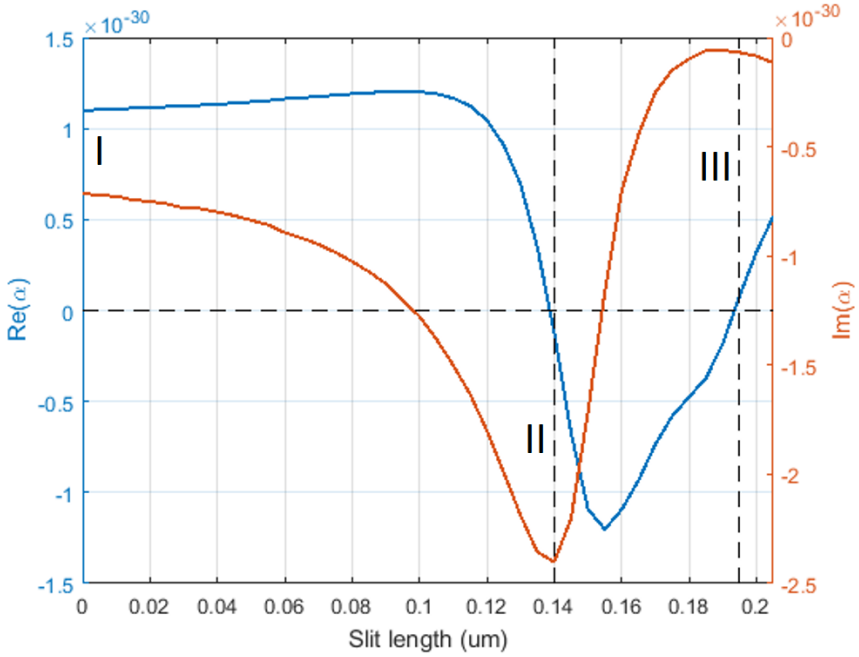

Figure 2.3: Real (blue) and imaginary (red) parts of the electric dipolar polarizability of the tip, varying the slit length.

polarization current and local electric field. Thus, an object with positive (negative) real part of polarizability can be considered capacitive (inductive) with respect to this field-current relation. For an aperture-type probe, the tip is usually capacitive, which is essentially the capacitance of a metallic tube. Intuitively, if we carve slits (four slits, each 90° apart from the neighboring ones, taking care of both polarization directions) along the aluminum shell of the tip, as shown in Figure 2.1 (a), and we illuminate the aperture frontally with electric field orthogonal to the slits, the two carved slits act as transmission lines terminated with a short circuit (assuming the metal to be a good conductor). According to transmission-line theory, we can then modify the input reactance of the slits by changing the length of the transmission line (as sketched on the Smith chart in Figure 2.1 (b)). Since the aperture has capacitive impedance, we aim at compen-

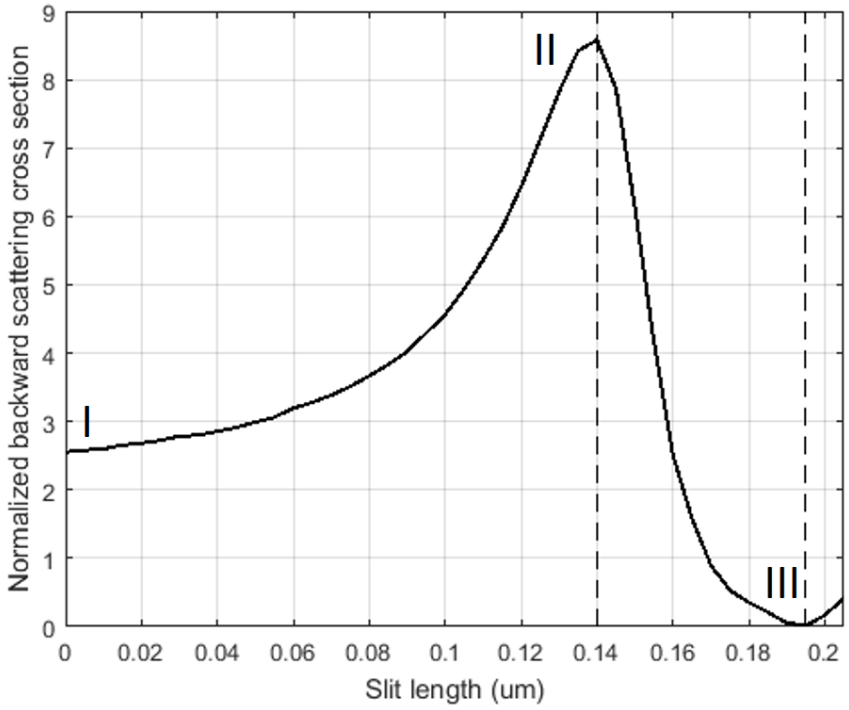

Figure 2.4: Backward scattering cross section of the probing tip with respect to the slit length (normalized by the geometrical cross section of the smallest sphere enclosing the tip).

sating it with an inductive impedance contribution from the slits. From a different, but equivalent, perspective, we aim at inducing dipole moments on the slits that oscillate out-of-phase with the dipole moment induced on the aperture, so that the total dipolar response of the tip is minimized, while the aperture is still polarized by the incident field. This is similar to the mechanism at the basis of scattering-cancellation cloaking, but without the need of introducing plasmonic media or elaborated mantle cloaks (see Figure 2.2).

To confirm this heuristic explanation, we extract the polarizability of an NSOM tip from numerical simulations using CST Microwave Studio, a time-domain commercial solver. The shape of the tip is a circular truncated cone,

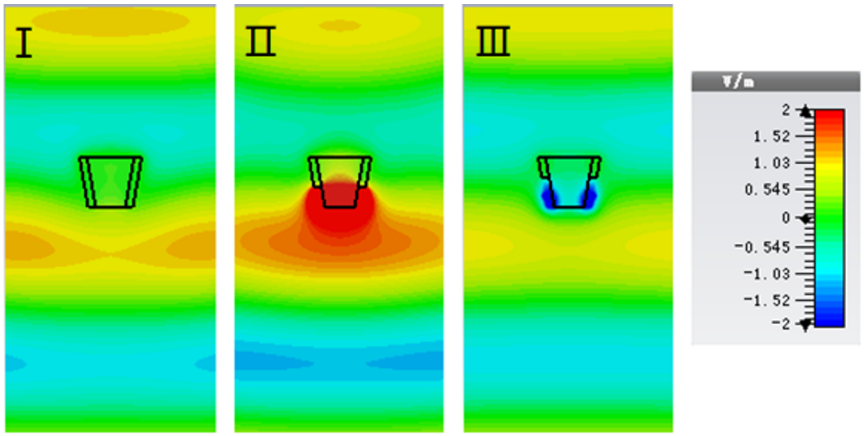

Figure 2.5: Time-snapshots of the electric field distribution around an illuminated tip, for three different slit lengths, under a plane wave excitation.

with a vertex angle of 20°. The aperture at the end of the tip is a circle with diameter 0.2 um. The thickness of aluminum shell is 0.05 um. In the simulation the aperture is frontally illuminated by a linearly polarized plane wave at 196 THz, with electric field perpendicular to the slits (since any polarization direction can be decomposed into two orthogonal directions, the results do not change with polarization directions, which is verified by simulation). Assuming purely dipolar scattering, we can derive the polarizability of the probe tip from the far-field results obtained in the simulation. We write the polarizability as

$$\alpha_e = \left(\alpha_{stat}^{-1} + j\frac{k_0^3}{6\pi\varepsilon_0} + j\gamma \right)^{-1}. \tag{2.2}$$

The first term inside the parentheses is purely real, representing the quasi-static polarizability of a dipolar scatterer (here the probe tip) from the far field results in the simulation. The second term is the well-known expression for the radiation loss ("radiation correction") for an arbitrary electric dipole radiator, where k_0 and ε_0 are the wave number and permittivity in background medium

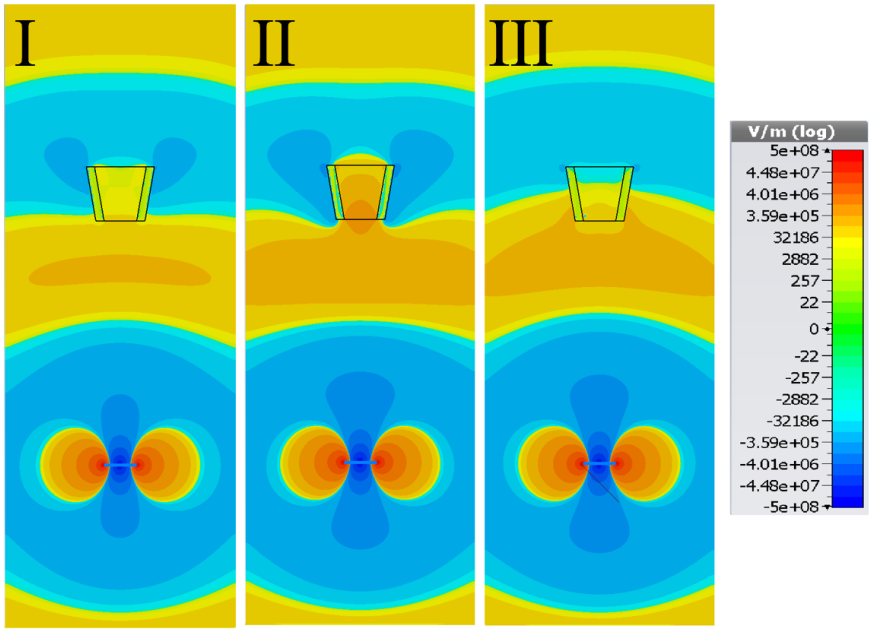

Figure 2.6: Time-snapshots of the electric field distribution around an illuminated tip, for three different slit lengths, under a spherical wave excitation.

(this terms only depends on the properties of the surrounding medium, i.e., free space in the present case). The third term accounts for the powered delivered to (absorbed by) the detector, modeling the fact that a sensor must absorb some energy to detect a signal. The power delivered to the detector load is $\frac{\omega}{2}\gamma|\alpha_e|^2|E_{loc}|^2$.

The dipolar polarizability and corresponding backward scattering cross section (SCS) is shown in Figures 2.3 and 2.4, as a function of the length of slits carved on the aluminum shell. It is clear from the results that the polarizability and thus the backward SCS is controlled to a large extent by the slit length, consistent with the qualitative discussions above. Three relevant cases are highlighted by roman numerals in the Figures 2.3 and 2.4, and time-snapshots of the electric field distribution around an illuminated tip are shown in Figure 2.5

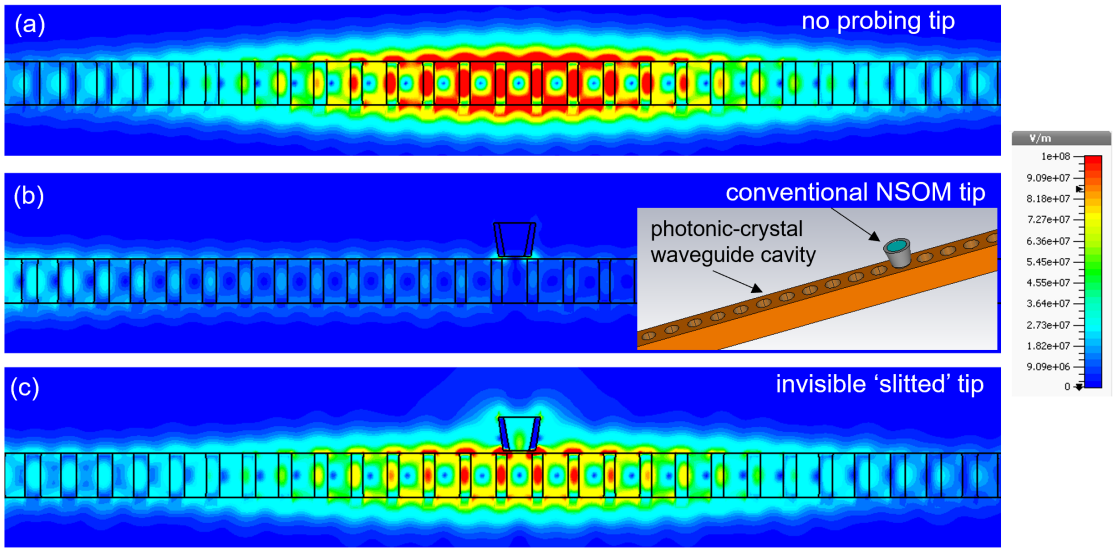

Figure 2.7: (a) Resonant field distribution (amplitude, at 196 THz) of an optical cavity formed by a defect in a photonic-crystal waveguide. (b) The field distribution is disrupted due to the presence of a conventional NSOM tip (schematic in the inset). The tip changes the resonant frequency of the cavity. (c) The field distribution is largely restored by using the proposed 'slitted' tip, with slit length as at point III. The fields inside the low-scattering tip are actually enhanced.

and 2.6 for each cases, under plane wave and spherical wave excitations. On Case (I), without slit, the tip is capacitive (positive real part of polarizability). The scattering is significant, which strongly disturbs the field distribution pattern. On Case (II), when the slit length is 0.135 um, the tip exhibits a resonance, the real part of polarizability vanishing and the imaginary part of polarizability reaching a peak. The electric dipole induced on the tip oscillates in quadrature with the local incident field, and thus power is extracted from the incident field in the form of scattering. The field distribution pattern is disturbed to the maximum extent. When the slit length is even longer, the real part of the polarizability is negative, i.e., the tip becomes inductive. When the slit length

reaches 0.195 um on Case (III), both the real and imaginary part of the polarizability vanishes, which means that the overall induced dipole moment is zero. The capacitance induced on the metallic tube is compensated by the inductance provided by the slits. From another point of view, the overall dipole moment is suppressed (the induced dipole moment in the shell oscillates out of phase with the dipole moment induced on the aperture), so the overall dipolar scattering vanishes. This is exactly the desired cloaking condition. The field distribution pattern is perturbed to the minimum extent, and meanwhile the induced field inside the aperture is not zero, preserving the ability to detect and measure the field distribution under study.

As an example of application, we show in Figure 2.7 the effect of placing an NSOM tip near a resonant cavity formed by a defect in a photonic-crystal waveguide, a typical example of system used in nano-electromagnetics. From perturbation theory, when a dipolar scatterer is placed near a photonic-crystal waveguide resonator, the resonant frequency and Q factor perturbation is

$$\frac{\Delta\omega}{\omega} + \frac{j}{2}\Delta\frac{1}{Q} \approx -\frac{\alpha_{re}|E_0|^2 + j\alpha_{im}|E_0|^2}{\int_v \left[\mu|H_0|^2 + \varepsilon|E_0|^2\right] dv}. \tag{2.3}$$

Clearly, the perturbation of real resonant frequency and reciprocal value of Q factor of a resonant cavity is linearly determined by the real and imaginary part of dipolar polarizability of the scatterer. It is clear that bringing the uncloaked tip near the cavity (Figure 2.7 (b)) disrupts the resonant field distribution under consideration. Instead, by using the designed 'slitted' tip (Figure 2.7 (c)), the field is largely restored. More generally, as studied in the theory of perturbations in microwave cavities [87], the shift in resonance frequency (and quality factor) of a perturbed cavity directly depends on the polarizability of the perturbation. Therefore, we can use the proposed 'slitted' tip to tune the resonance

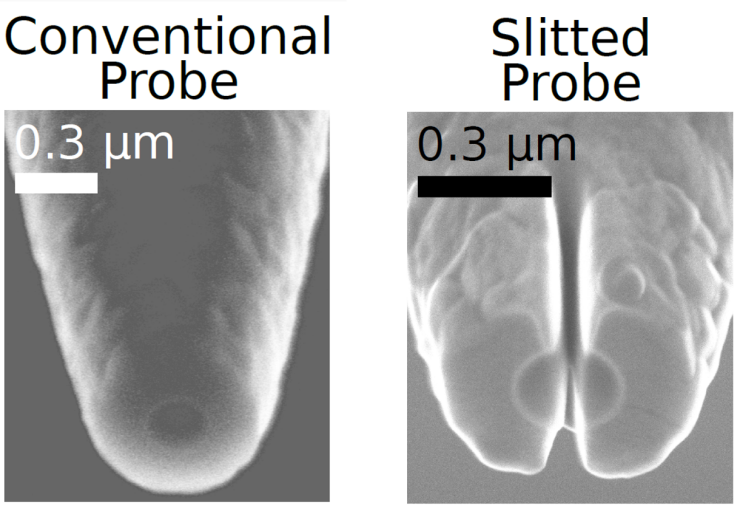

Figure 2.8: SEM pictures of a conventional probe (left) and a slitted nanostructured probe (right).

of an optical cavity at will, as well as to modify its Q factor, increasing or decreasing the radiation loss, by simply changing the slit length [88].

2.4 Conclusion

We have proposed a novel method, inspired by impedance concepts and transmission-line theory, to make a near-field probe invisible at infrared frequencies, without the need for plasmonic materials or metamaterials. The proposed structure can readily be fabricated with existing nanotechnology. Our work opens new possibilities for cloaking technology to have real practical impact in nano-electromagnetics and for optical imaging. We have collaborated with Prof. L. (Kobus) Kuipers group on experimentally fabricating and testing the proposed cloaked NSOM probes (Figure 2.8). Characterization and testing are currently underway.

CHAPTER 3

ACTIVE SCATTERING-CANCELLATION CLOAKING: BROADBAND INVISIBILITY AND STABILITY CONSTRAINTS

3.1 Introduction

While great progress has been made in the theory and realization of invisibility devices, this technology has been severely hindered by fundamental difficulties in realizing broadband scattering suppression, especially when the object to be concealed is electrically large, an issue that appears independent of the cloaking techniques being considered [57, 58, 59, 60, 61, 62]. Indeed, physical bounds have been recently reported, based on the Bode-Fano theory of broadband impedance matching, that set a hard upper limit on the operating bandwidth of a generic cloaking system, assuming only linearity, causality, and passivity [16]. It should also be noted that, although the original derivation of the Bode-Fano limit assumes reciprocity (symmetry of the scattering matrix), lossless nonreciprocal matching is still bounded by the same Bode-Fano limit. A proof of this statement is provided in Section (1.3.2). Therefore, to realize a broadband invisibility device, beyond these strict limits, the only option is to break at least one of the three assumptions underpinning these physical bounds, namely, causality, linearity, and passivity. (i) Causality is an intrinsic feature that any physically realizable system must respect. While it may be possible to break a relative definition of causality in scenarios with a background medium supporting waves with velocity lower than the speed of light in vacuum (e.g., in a high-index background), as suggested in [60], most cases of interest involve an object to be concealed in free space, for which the speed of light in vacuum sets

an insurmountable causality constraint. (ii) Breaking linearity means introducing frequency harmonics and distorting the incident signals, which is typically undesired. (ii) Breaking passivity, therefore, appears to be the most promising option to realize broadband invisibility. Indeed, some pioneering works have already explored the potential of active cloaking [57, 63, 64, 65], without, however, quantifying the performance against the passivity bounds and without a comprehensive investigation of the stability issues involved with active scattering systems. These research activities are also part of broader efforts aimed at increasing the bandwidth and robustness of metamaterial systems based on active and non-Foster structures [89, 90, 91, 92, 93, 94, 95].

In this chapter, we fully investigate the broadband scattering performance and the stability issues of active scattering-cancellation cloaking, using the simplest possible, yet general, model system, namely, a single-layer homogenous active cloak. We theoretically demonstrate active scattering-cancellation cloaks in both 1-D and 3-D scenarios, and we compare their scattering performance with the one of their passive plasmonic counterparts, and against the Bode-Fano bound. In addition, stability issues are thoroughly analyzed in terms of geometrical and material parameters. Owing to the simplicity of the considered cloaking configuration, we are able to derive closed-form stability constraints and offer qualitative guidelines on how to ensure stability. The proposed one-layer active cloaks show the performance baseline of active scattering-cancellation cloaking, which may then be improved with more complex designs [36].

The rest of the chapter is organized as follows: In Section 2 we demonstrate the necessity of using active media to achieve broadband cloaking, and we discuss a general permittivity dispersion model for active media, i.e., the active

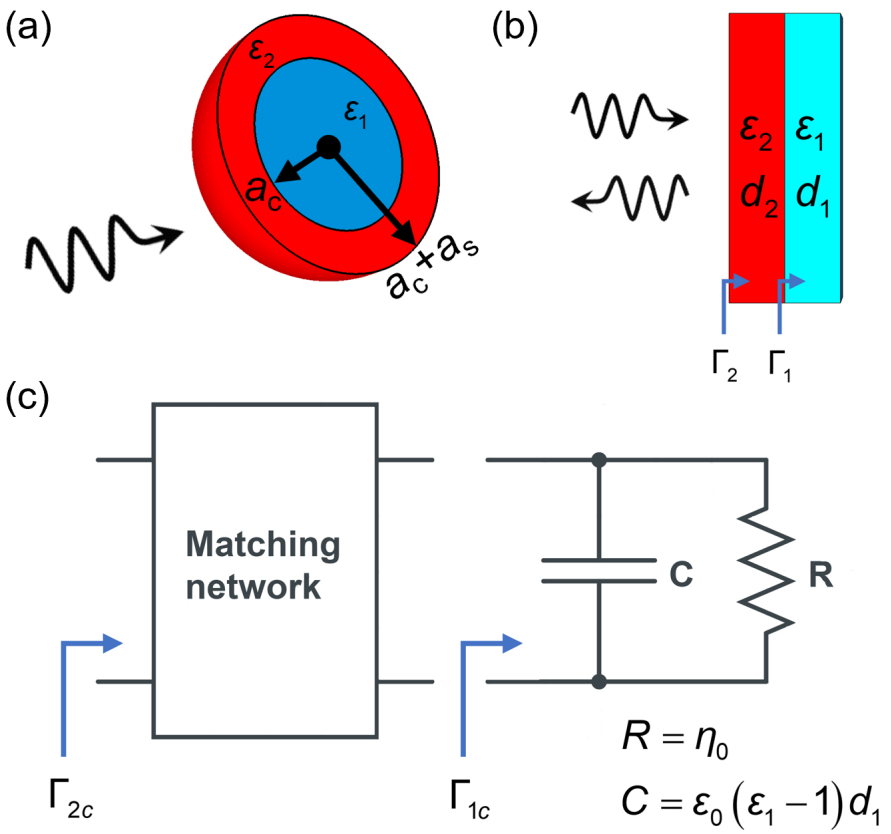

Figure 3.1: (a) Sketch of a 3-D spherical scatterer (blue) covered by a spherical concentric one-layer cloak (red) under plane-wave incidence. The relative permittivity and radius of the core and shell are ε_1, a_c, ε_2 and a_s, respectively. (b) Sketch of a 1-D dielectric planar slab (light blue) covered by a one-layer cloaking slab (red) under normal plane-wave incidence. The relative permittivity and thickness of the dielectric and cloaking slabs are ε_1, d_1, ε_2 and d_2, respectively. The reflection coefficients seen from the un-cloaked dielectric slab and from the cloaked slab are Γ_1 and Γ_2, respectively. (c) Corresponding lumped circuit model for 1-D scattering. The values of R and C are indicated in the figure, and the reflection coefficients seen from the un-matched circuit and the matched circuit are Γ_{1c} and Γ_{2c}, respectively.

Lorentz model. Then, in Sections 3 and 4, we report and discuss the broadband scattering performance of optimized one-layer active cloaks in 1-D and 3-D, and we analyze the stability constraints of these active systems. Finally, in Section 5, we offer some concluding remarks on active scattering-cancellation cloaking. In the Appendix, we provide the geometrical and material parameters of all the cloaking designs.

3.2 Can active media improve the cloaking bandwidth?

Let us first examine why a generic passive cloak cannot be arbitrarily broadband. Consider an electrically small dielectric spherical scatterer, whose dominant scattering contribution is the electric dipolar component. If the scatterer is covered by a cloak made of an isotropic, homogeneous, and non-magnetic concentric shell, the condition to cancel the electric dipolar scattering, in the quasi-static regime, is given by [15]

$$\left(\frac{a_c}{a_c + a_s}\right)^3 = \frac{(\varepsilon_2 - \varepsilon_0)(2\varepsilon_2 + \varepsilon_1)}{(\varepsilon_2 - \varepsilon_1)(2\varepsilon_2 + \varepsilon_0)}, \tag{3.1}$$

where a_c and $a_c + a_s$ are the radii, and ε_1 and ε_2 are the relative permittivity of the spherical scatterer and the concentric shell cloak, respectively (Fig. 3.1 (a)). Considering a dielectric ($\varepsilon_1 > \varepsilon_0$) or a perfectly conducting ($\varepsilon_1 \to -\infty$) core, Eq. 3.1 predicts that, to obtain arbitrarily-broadband cloaking operation, the cloak would need to have frequency-constant real permittivity, with value $\varepsilon_2 < \varepsilon_0$. If dynamic effects (i.e., retardation) are non-negligible, negative permittivity dispersion (negative slope of $\varepsilon_2(\omega)$) in a lossless frequency window may even be required. These requirements directly violate the constraints on the permittivity

dispersion function imposed by energy-conservation in passive structures [7]:

$$\frac{\partial \varepsilon(\omega)}{\partial \omega} \geq \frac{\varepsilon_0 - \varepsilon}{\omega}, \tag{3.2}$$

which implies that $\varepsilon(\omega)$ must have a positive non-zero slope for any permittivity value below ε_0. It is therefore necessary to break the assumption of passivity in order to meet the requirements of Eq. 3.1 over any non-zero bandwidth. Indeed, if the cloak is made of a suitable active (gain) medium, its permittivity function can be flat, or even have negative slope, in the desired frequency window.

The permittivity dispersion of any, active or passive, material can be approximately modeled using the generalized classical Lorentz model, which is a good approximation to more rigorous quantum-mechanical methods (density-matrix equations of motion for a weakly perturbed two-level system) [96, 5, 97, 98]. In the Lorentz model, each resonant process in the medium is modeled as a classical harmonic oscillator (a classical model of a two-level atomic/molecular system). Considering the contribution of all resonance processes, the relative permittivity of a medium can be expressed as [32, 4]

$$\varepsilon = 1 + \sum_i \frac{f_i \omega_{pi}^2}{\omega_{0i}^2 - \omega^2 + j\omega\gamma_i}, \tag{3.3}$$

where ω is the radian frequency; ω_{0i} and γ_i are the resonant frequency and the resonance linewidth, respectively, for the i^{th} resonator; f_i is the so-called resonator strength, and ω_{pi} is the plasma frequency defined as

$$\omega_{pi}^2 = \frac{N_i e^2}{\varepsilon_0 m}, \tag{3.4}$$

where N_i is the number density of resonating atoms / molecules, e is the electron charge, m is the electron mass, and ε_0 is the free space permittivity. Throughout the chapter we assume and suppress a e^{+st} time dependence, where we have defined a Laplace complex variable, $s = \sigma + j\omega$, to represent complex frequency. If

the resonator is passive (active), f_i is positive (negative) [97, 98, 99, 100]. A negative oscillator strength models the effect of population inversion in an active material, namely, the fact that the atoms / molecules of the medium exist in an excited energy state, rather than in the ground state (which clearly requires an external energy pump) [97, 98, 99, 100]. Note that the effective permittivity dispersion of an active metamaterial comprised of resonant meta-atoms can also be expressed by the same Lorentz model, with ω_{pi}, ω_{0i} and γ_i depending on the polarizability of the meta-atoms and their density, following well-established homogenization procedures [101]. The active Lorentz model has been successfully used in numerical calculations of wave propagation in active materials and metamaterials [99, 100], and to study parity-time-symmetric photonic structures [102, 103].

Other classical dispersion models can be obtained as limiting cases of the Lorentz model. For instance, the Drude model for free-electron plasmas and plasmonic media is obtained by setting the resonant frequency to zero [32, 4]. In the cloaking designs considered in the next two sections, the permittivity dispersion of the passive plasmonic cloak used as a benchmark follows a classical Drude model

$$\varepsilon_2 = 1 - \frac{\omega_p^2}{\omega^2 - j\omega\gamma}. \tag{3.5}$$

Instead, in our active cloaking designs, we consider an active material with a permittivity dispersion containing both a normal Lorentzian and an anti-Lorentzian:

$$\varepsilon_2 = 1 + \frac{f_1\omega_{p1}^2}{\omega_{01}^2 - \omega^2 + j\omega\gamma_1} + \frac{f_2\omega_{p2}^2}{\omega_{02}^2 - \omega^2 + j\omega\gamma_2}, \tag{3.6}$$

where $f_1 > 0$, $f_2 < 0$ and $\omega_{01<\omega_{02}}$. In this active scenario, Kramers-Kronig relations and energy conservation allow the presence of a locally flat and low-loss/gain dispersion window between the two resonances, which may enable a broad-

band cloaking effect, as discussed in the next two sections.

Before investigating active cloaking designs and their stability issues, it is relevant to check the stability of the permittivity function itself, treated as a system function relating the electric displacement field (output) to the electric field (input). The position of the poles associated with the anti-Lorentzian in the s-plane is given by

$$\sigma + j\omega = \frac{-\gamma_2 \pm j\sqrt{4\omega_{02}^2 - \gamma_2^2}}{2}, \tag{3.7}$$

Since γ_2, which represents the resonance linewidth, is positive by definition, the real part of the position of the pole is always negative, indicating that the permittivity function of the active medium is intrinsically stable, as it corresponds to decaying oscillations in time (not in space) under a spatially-uniform temporal impulse response. However, as shown in the next sections, the stability of the permittivity of the active medium does not guarantee that a system containing such a medium would always be stable. This is because of the complex feedback mechanism introduced by any finite geometrical configuration. In fact, the stability of the entire system depends on both its specific geometrical structure and the anti-Lorentzian parameters, ω_{p2}, ω_{02}, and γ_2.

3.3 One-dimensional active cloaking

In this section, we show that a simple one-layer active cloak can indeed overcome the bandwidth limit of 1-D passive cloaks, and we assess its stability.

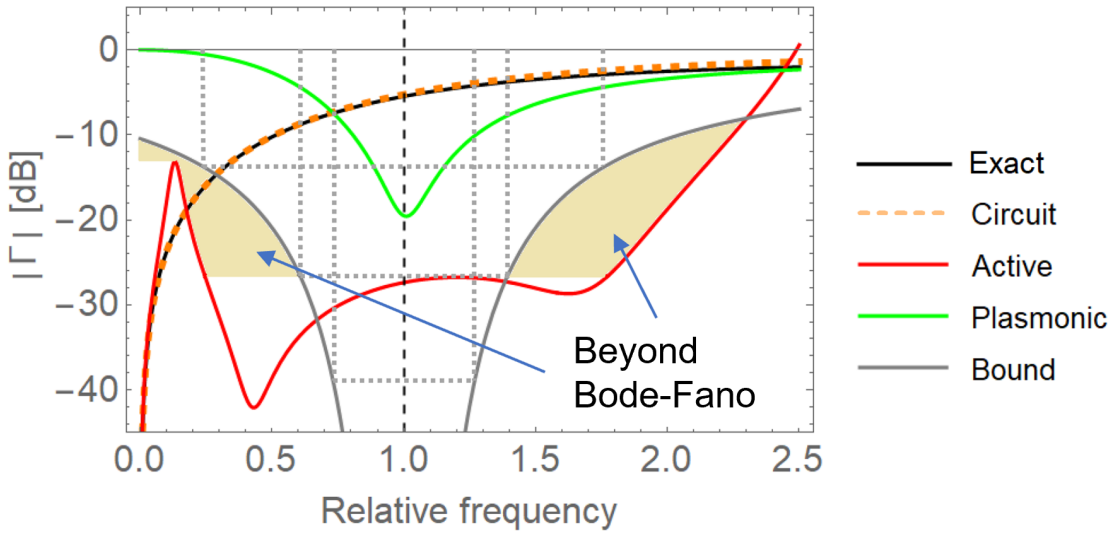

Figure 3.2: Magnitude of the reflection coefficient of a dielectric slab in free space (calculated with exact formulas and using a lumped-element circuit model) and of the same slab cloaked by an active layer and by a passive plasmonic layer, compared against the Bode-Fano bound. All the geometrical and material parameters are given in the Appendix of this chapter.

3.3.1 Broadband scattering behavior

Consider a dielectric slab in free space with an electromagnetic wave impinging on it normally, as illustrated in Fig. 3.1(b). Since this 1-D transversely invariant scattering problem has only one scattering channel, namely, the specular reflection, we use the reflection coefficient to describe its scattering behavior. In front of the dielectric slab, we introduce a cloaking slab to suppress the overall reflection. A 1-D wave-propagation problem of this type can be modeled and analyzed, exactly, using transmission-line theory. Each slab is modeled by a segment of transmission line. The ABCD parameters of a cascade of transmission-

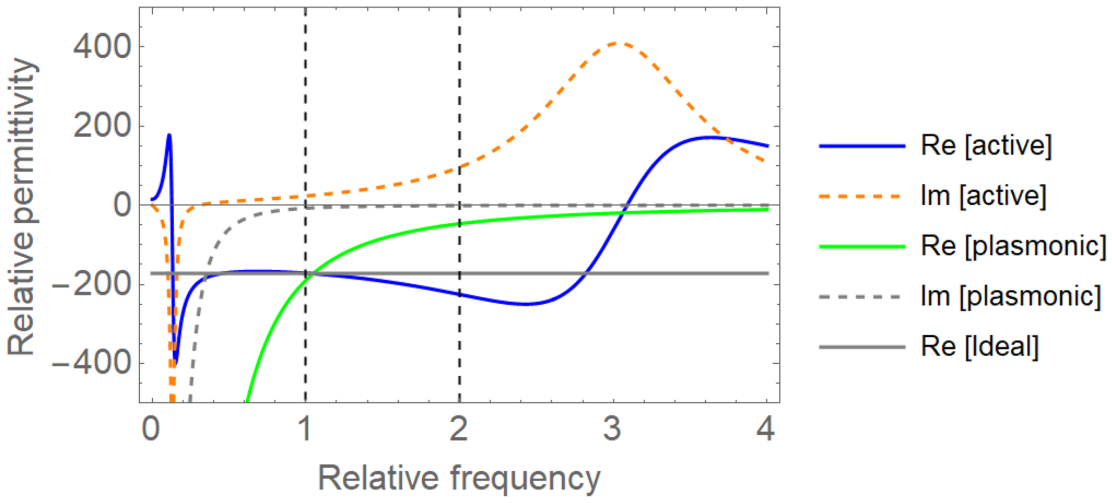

Figure 3.3: Permittivity (real and imaginary part) of an active medium and a passive plasmonic medium, corresponding to the materials used for the 1-D cloaking design in Fig. 3.2. The horizontal gray line indicates the required permittivity for arbitrarily broadband invisibility.

line segments is then given by [39]

$$\begin{pmatrix} A & B \\ C & D \end{pmatrix} = \prod_i \begin{pmatrix} \cos k_i d_i & jZ_i \sin k_i d_i \\ jZ_i^{-1} \sin k_i d_i & \cos k_i d_i \end{pmatrix}, \tag{3.8}$$

where k_i is the complex propagation constant (wavenumber), d_i is the thickness, and Z_i is the wave impedance, respectively, of the i^{th} slab. From the ABCD parameters, we can directly calculate the reflection coefficient as [39]

$$\Gamma = \frac{A + B/\eta_0 \; - C\eta_0 - D}{A + B/\eta_0 \; + C\eta_0 + D}, \tag{3.9}$$

where η_0 is the free-space wave impedance. The amplitude of the reflection coefficient of an uncloaked dielectric slab is shown in Fig. 3.2 with a solid black line, for a slab thickness $d_1 = \lambda_c/40$ (at the central free-space wavelength λ_c), and permittivity $\varepsilon_1 = 10$.

While the transmission-line model above is exact, we can approximately

model the slab, around the frequency of interest, as a lumped-element circuit, which allows us to apply the analytical Bode-Fano theory of broadband matching. In particular, if the slab thickness d is subwavelength, the circuit model of a lossless dielectric slab is simply a shunt capacitor of value [101],

$$C = \varepsilon_0 (\varepsilon - 1) d, \tag{3.10}$$

connected with a resistor modeling the semi-infinite space behind the slab, as illustrated in Fig. 3.1 (c). The amplitude of the reflection coefficient calculated from this circuit model is shown in Fig. 3.2 with an orange dashed line. We see that the calculations based on transmission lines and lumped elements are in good agreement, which indicates that the lumped-element model captures the local response accurately. Next, we calculate the Bode-Fano limit based on this circuit model, which can be expressed as an integral inequality [39, 37, 38]

$$\int_0^\infty \ln \frac{1}{|\Gamma_{2c}|} d\omega \leq \frac{\pi}{RC}. \tag{3.11}$$

The optimal tradeoff between reflection suppression and bandwidth is obtained by solving the integral in Eq. 3.11 considering an ideal box-like frequency response for $|\Gamma_{2c}|$ with constant reflection coefficient inside the working bandwidth and unitary reflection outside (see [39]) since this response makes full use of the available bandwidth. The resulting Bode-Fano bound is shown in Fig. 3.2 (grey solid lines) in the form of an optimal trade-off between $|\Gamma_{2c}|$ and the bandwidth over which this level of reflection can be sustained.

We then design and optimize a passive plasmonic cloak and an active cloak for the slab based on materials with permittivity given by Eqs. 3.5 and 3.6, respectively, at the same central frequency ω_c. To show the potential of active cloaking, we deliberately choose an extreme situation in which the required cloak permittivity, which can be approximately calculated as $\varepsilon_2 = \varepsilon_0 -$

$(\varepsilon_1 - \varepsilon_0)\, d_1/d_2$, is very negative: $\varepsilon_2 \approx -170\varepsilon_0$ using the parameters given in Appendix B. For such a negative permittivity, the minimum slope of the dispersion function for any passive material, given by Eq. 3.2, would be very large and positive, which suggests that, with passive designs, good cloaking performance can be obtained only over a very narrow bandwidth around ω_c.

The optimized permittivity dispersion functions for the passive and active cloaks are shown in Fig. 3.3. We see that the passive plasmonic medium is highly dispersive around the central frequency, with a monotonically increasing permittivity, as expected. In contrast, the active medium supports an approximately flat dispersion window, in a region with low loss or gain ($0.2 < \omega/\omega_c < 1.8$), which approximates much better the required permittivity for arbitrarily-broadband cloaking (horizontal gray line). The resulting reflection coefficients of the passively- and actively cloaked slab are reported in Fig. 3.2. We see that the bandwidth of the plasmonic cloak is well within the Bode-Fano bound, as expected, whereas the bandwidth of the active cloak is significantly beyond the bound. This simple example shows the potential of active cloaking to realize ultra-broadband invisibility.

3.3.2 Stability analysis

We investigate the stability of the active cloaking system by analyzing the poles of the reflection coefficient in the s-plane (Fig. 3.4(a)). In the s-plane, a pole on the left (right) half-plane is associated with decaying (growing) oscillations in time, namely, with a stable (unstable) response. The case of a pole on the imaginary axis in the s-plane corresponds to the lasing threshold, where gain

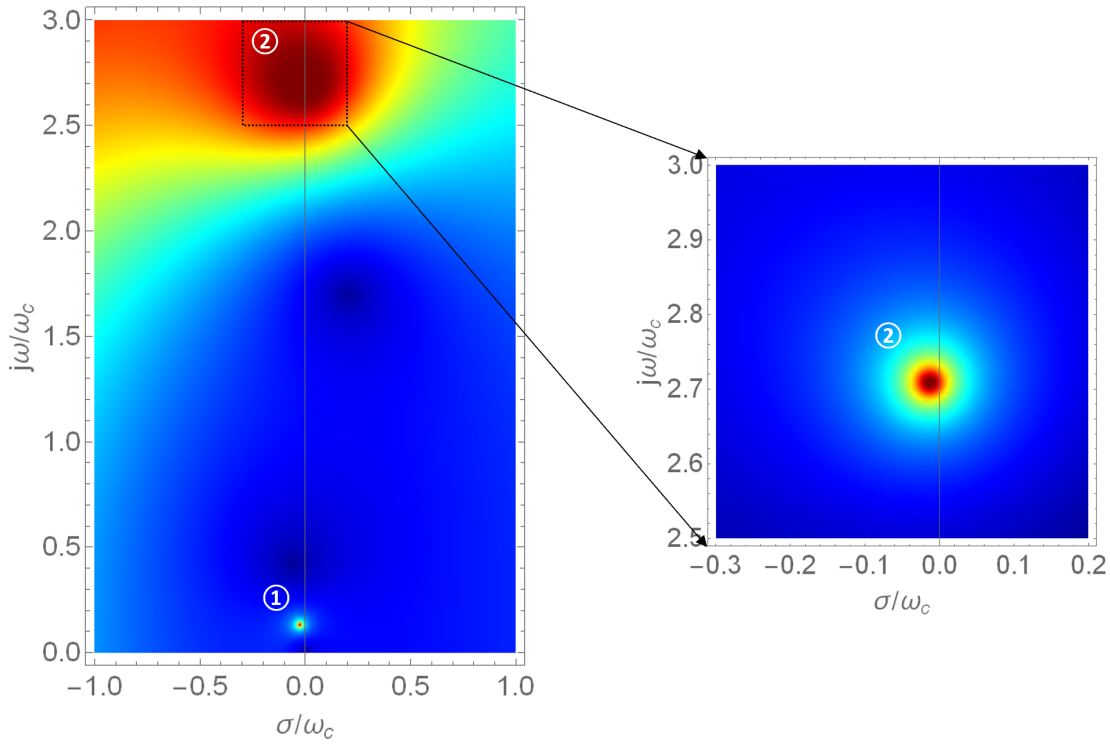

Figure 3.4: Magnitude of the reflection coefficient, for the dielectric slab with active cloak in Fig. 3.3, plotted in the s-plane, with two poles highlighted. Pole 2, associated with the active Lorentzian resonance of the cloak permittivity, governs the stability of this active system.

fully compensates any loss channel. For a subwavelength slab (far from any Fabry-Perot resonance), Pole 1 and Pole 2 in Fig. 3.4(a) are mainly associated, respectively, with the normal Lorentzian resonance and the anti-Lorentzian resonance of the permittivity of the active cloaking layer [Eq. 3.6]. While Pole 1 is usually stable, due to passivity, Pole 2 can be either stable or unstable.

The location of Pole 2 in the s-plane can be obtained, in closed-form, under some reasonable simplifying assumptions. First, instead of using full dynamic formulas, we can use the lumped-circuit model shown in Fig. 3.1(c), which captures the local response of the system in the long-wavelength regime. Second,

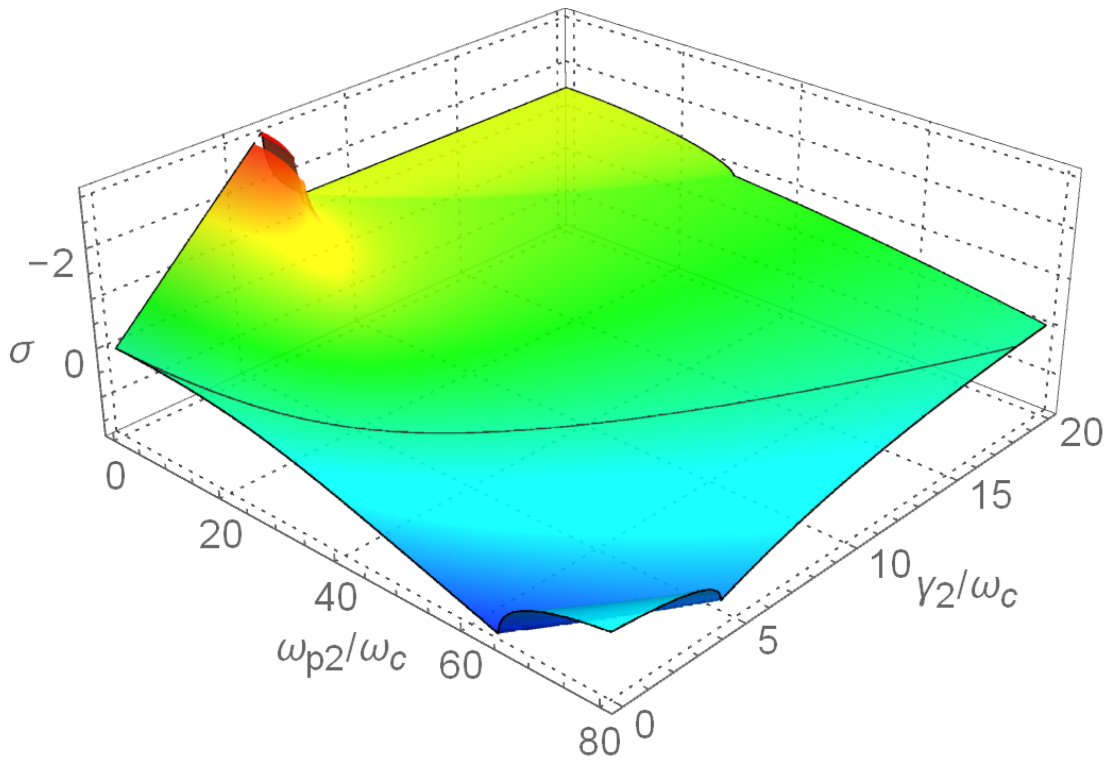

Figure 3.5: σ of the location of Pole 2 in the s-plane as a function of ω_{p2} and γ_2.

the normal Lorentzian resonance and the anti-Lorentzian resonance of the active medium can be assumed to be sufficiently well separated in frequency (which is indeed required to achieve broadband cloaking as in Fig. 3.1). The resulting expression is simple but lengthy, so we do not show it here for conciseness. Instead, we plot the position σ of Pole 2 as a function of ω_{p2} and γ_2 in Fig. 3.5. From the figure, we see that as ω_{p2} increases, we need larger and larger γ_2 to ensure a negative σ, i.e., stability. For a given ω_{p2}, we can always find γ_2 large enough to ensure stability. Interestingly, as we will see in the following, this is not the case in a 3-D scattering system.

For our design with $\omega_{p2} = 38.5\omega_c$, σ of the location of Pole 2 in the s-plane

is a monotonically decreasing function with respect to the resonance linewidth γ_2, as seen in Fig. 3.5: with $\gamma_2 = 0$, the pole is in the right half of the s-plane and the system is unstable; then, as γ_2 is increased above a certain threshold 1.16 ω_c, Pole 2 moves across the imaginary axis into the stable half plane. The larger γ_2 is, the farther the pole moves away from the imaginary axis, making the system more robustly stable. This behavior is not surprising since an active resonance with larger lifetime (i.e., smaller resonance linewidth γ_2) is expected to be associated with higher instabilities as the electromagnetic wave would spend more time interacting with the gain medium. Increasing γ_2 is, therefore, beneficial in terms of stability, but is detrimental to the performance of the cloaking device since it increases the imaginary part of the permittivity within the cloaking bandwidth, which leads to higher absorption/emission, rather than a reduction of scattering.

3.4 Three-dimensional active cloaking

In this section, we apply active cloaking to realize broadband scattering suppression in a 3-D scenario, and we assess the stability of this active scattering system.

3.4.1 Broadband scattering behavior

Consider an electrically small spherical scatterer made of a homogeneous isotropic material, surrounded by free space, illuminated by a plane electromagnetic wave (equivalent to an infinite discrete sum of spherical harmonics). The

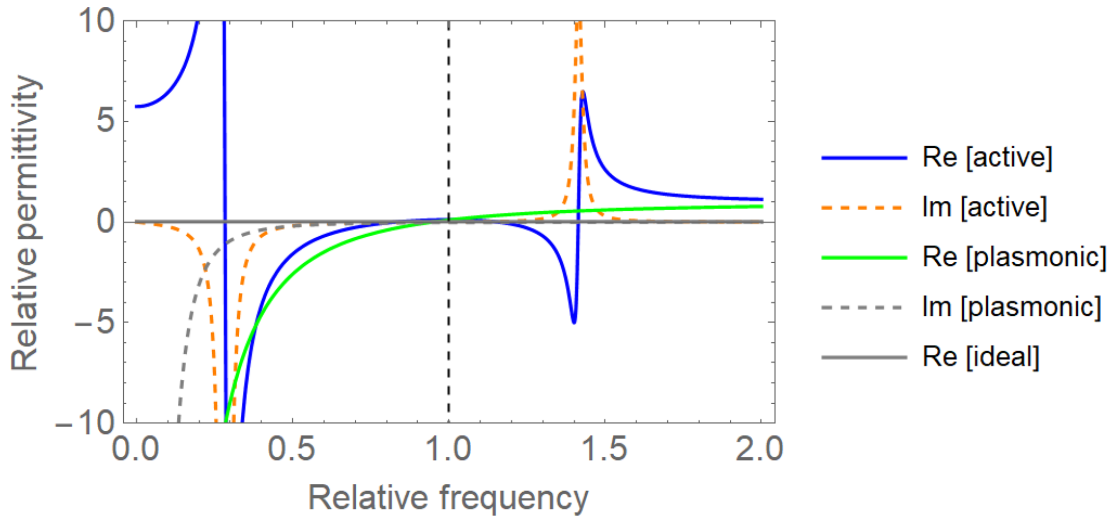

Figure 3.6: Permittivity (real and imaginary part) of an active medium and a passive plasmonic medium, corresponding to the materials used for the 3-D cloaking design in. The horizontal gray line indicates the required permittivity, given by Eq. 3.1, for arbitrarily-broadband invisibility.

induced conduction or polarization current, which can be expanded into multipolar contributions, re-radiates energy in the form of a scattered wave. If the structure is rotationally invariant, each multipolar component acts as an independent scattering source, responding to and scattering into only one spherical harmonic, forming different orthogonal scattering channels. An induced electric dipole radiates a TM spherical wave of first order, a magnetic dipole a TE spherical wave of the first order, etc. [104]. If the size of the spherical scatterer is subwavelength, the dominant scattering contribution is typically the one originating from the induced electric dipole. Following the conventional design process of scattering-cancellation cloaking, we cover the spherical scatterer with a concentric one-layer spherical shell, composed of a homogeneous, isotropic and non-magnetic medium. The structure is shown in Fig. 3.1(a). The shell should then be designed such that the overall polarizability of the cloaked

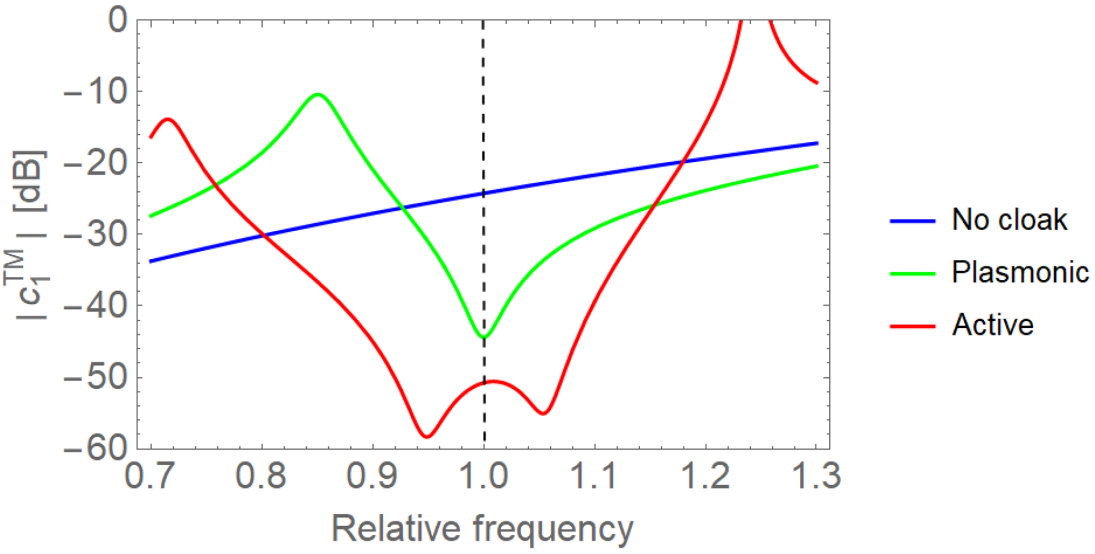

Figure 3.7: Magnitude of the electric-dipolar scattering coefficient, c_1^{TM}, for an electrically small spherical PEC scatterer in free space, and for the same scatterer cloaked by an active shell and by a passive plasmonic shell. All the geometrical and material parameters are given in the Appendix of this chapter.

object vanishes as the electric dipole moments induced on the shell and on the core compensate each other. Based on this strategy, the overall scattering can be suppressed drastically. While this heuristic explanation is valid for small objects of different shapes, for a spherically-symmetric scattering problem of the type considered here, the scattering cross section of the cloaked object can be calculated exactly using Mie theory [32, 105]. The scattering coefficients for TM and TE spherical harmonics of nth order are given by [15]

$$c_n^{TM} = -\frac{U_n^{TM}}{U_n^{TM} - jV_n^{TM}}, c_n^{TE} = -\frac{U_n^{TE}}{U_n^{TE} - jV_n^{TE}}, \tag{3.12}$$

where U and V are matrix determinants derived from the electromagnetic boundary conditions at the spherical interfaces (their definition can be found

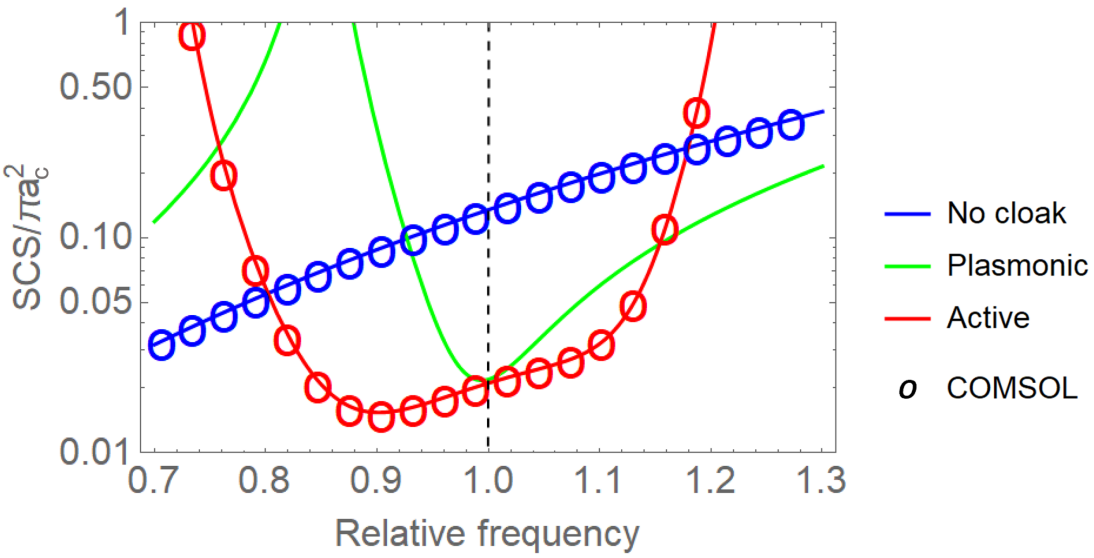

Figure 3.8: Normalized scattering cross section (SCS) of the spherical PEC scatterer in Fig.3.7, and of the same scatterer cloaked by an active shell and by a passive plasmonic shell. SCS is normalized by the geometrical cross-section. Solid curves: analytical calculations. Markers: numerical full-wave simulations.

in [15]). The total scattering cross section (SCS) is then calculated as

$$\mathrm{SCS} = \frac{\lambda_0^2}{2\pi} \sum_{n=1}^{\infty} (2n+1) \left(\left| c_n^{TM} \right|^2 + \left| c_n^{TE} \right|^2 \right), \tag{3.13}$$

where λ_0 is the free-space wavelength.

We then design and optimize a passive plasmonic cloak and an active cloak for an electrically small PEC sphere ($a_c = \lambda_c/15$). The optimized permittivity dispersions for both cases are shown in Fig. 3.6, compared to the ideal permittivity required to have arbitrarily-broadband invisibility 0.14, according to Eq.3.1. As for the planar case, we consider a permittivity dispersion for the active medium containing a normal Lorentzian (resonant process with loss) and an anti-Lorentzian (resonant process with gain), located at about $0.3\omega_c$ and $1.4\omega_c$, respectively. Between the two resonances, the permittivity dispersion around

the central frequency is relatively flat, and the loss or gain is very low. As for the 1-D case in Section 3.3, this permittivity dispersion is suitable for broadband cloaking, since it matches the required permittivity profile predicted by Eq.3.1 much more closely. In contrast, the dispersion of the passive plasmonic medium has large positive slope around the central frequency.

The dominant scattering coefficient c_1^{TM} for the passive and active cloaked object is reported in Fig. 3.7. These results clearly show that the optimized active cloak, despite its simplicity, already exhibits a significantly broader bandwidth compared to the passive plasmonic cloak. Yet, unlike the 1D case, we find that the scattering performance of this active cloak are still well within the approximate Bode-Fano limit for this 3-D case [16], which predicts, for example, a maximum achievable bandwidth of $1.4\omega_c$ for $\left|c_1^{TM}\right| = -50$ dB (beyond the frequency range considered in Fig. 3.7). Our investigations suggest that increasing the bandwidth to values near the bound, while also keeping stability (additional details below), appears to be impossible with this single-layer active cloak. Further investigations, beyond the scope of this work, are needed to verify whether multi-layered active cloaks may allow approaching and surpassing the physical bound. We also note that, outside the working bandwidth, the scattering coefficient of the cloaked sphere is generally larger than the one of the uncloaked spheres. At some frequencies, for example at $1.24\omega_c$, the magnitude of the scattering coefficient of the object with active cloak is even larger than unity, due to the fact that active media can pump energy from an external source into the electromagnetic field, amplifying the field intensity outside the cloaking bandwidth.

In Fig. 3.8, we also show the total scattering cross section (SCS) of the spher-

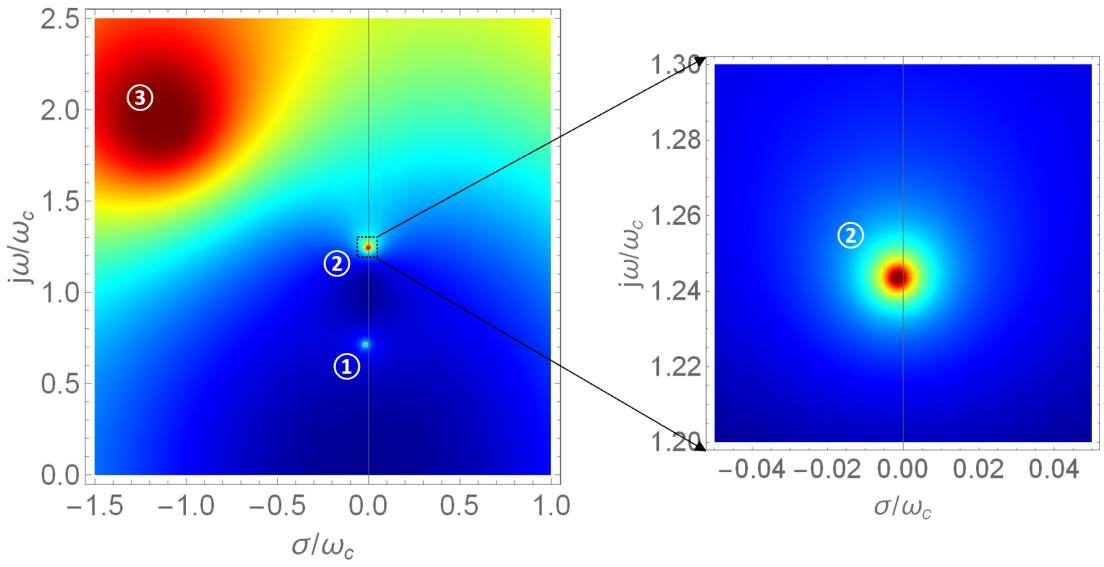

Figure 3.9: Magnitude of the scattering coefficient, c_1^{TM}, for the spherical PEC scatterer with active cloak.

ical scatterer with and without cloaks. Even when all scattering contributions are included, our active cloaking design shows significant scattering suppression over a much broader bandwidth compared to a typical passive plasmonic cloak, which means that higher-order scattering contributions are not enhanced by the presence of the active cloak. We also validate the performance of the designed active cloak with full-wave numerical simulations using a commercial software based on the finite-element method (COMSOL Multiphysics [106]). As seen in Fig. 3.8, perfect agreement is obtained.

3.4.2 Stability analysis

Compared with its 1-D counterpart, the stability of a 3-D active cloak is more difficult to analyze and enforce. Besides the linewidth γ_2, there are extra restric-

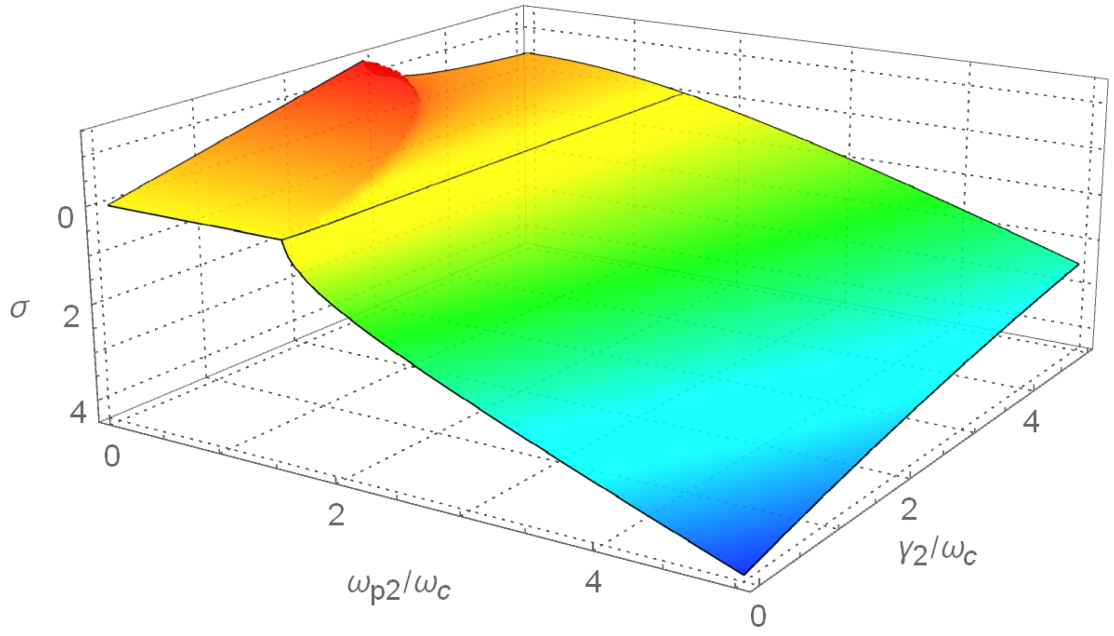

Figure 3.10: σ of the location of Pole 2 in the s-plane as a function of ω_{p2} and γ_2.

tions on ω_{p2} with respect to ω_0, as discussed below.

Fig. 3.9 show the lowest-frequency poles of c_1^{TM} in the s-plane . Poles 1 and 2 are mainly associated with the Lorentzian and anti-Lorentzian resonances in Eq. 3.6, respectively, whereas Pole 3 represents the first dynamic resonance of the core-shell structure [18]. All the scattering poles of our optimized cloaking design are stable, as shown in the figure. It is, however, relevant to investigate the stability condition more generally, with the goal of obtaining qualitative insight into what parameters govern the stability of the system and about whether the cloaking bandwidth may be further increased.

Similar to the 1-D case, for electrically small scatterers, the stability is mostly governed by the pole associated with the anti-Lorentzian resonance (Pole 2), which is the closest to the real frequency axis as seen in Fig. 3.9. We calculate

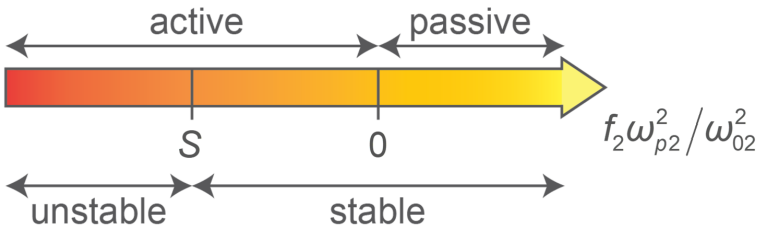

Figure 3.11: Schematic of the passive/active and stable/unstable behavior of the scattering system with respect to the parameter $f_2\omega_{p2}^2/\omega_{02}^2$.

the imaginary part of the position of Pole 2 analytically, under some approximations. First, considering that the size of the core-shell structure is much smaller than the operating wavelength, it is safe to use small-argument approximations for the spherical Bessel functions that appear in the expression of the scattering coefficients [28]. This approximation is similar to the lumped circuit model in 1-D. Second, as is done in 1-D, the contribution of the normal Lorentzian is considered small enough to be ignored (see Fig. 3.6). Third, we neglect radiative losses in the calculation of the scattering coefficients, which corresponds to defining the coefficients as [107, 52]

$$c_1^{TM} = -jU_1^{TM}/V_1^{TM}, \tag{3.14}$$

instead of using the exact form in Eq. 3.12. This approximation, which makes the scattering coefficient purely imaginary in the lossless case (and the electric-dipole polarizability purely real), is equivalent to the Rayleigh approximation of scattering theory [24]. This is also equivalent to removing the so-called Sipe-Kranendonk radiation correction to the expression of the quasi-static electric-dipole polarizability [107, 52, 108].

Under these reasonable approximations, we can calculate the position of Pole 2 in the s-plane by equating the denominator of the scattering coefficient to

zero. We obtain a closed-form expression for the pole in the s-plane as

$$\sigma + j\omega = -\frac{\gamma_2}{2} \pm \sqrt{\frac{\gamma_2^2}{4} - \omega_{02}^2 - \frac{1}{3}\left(1 + \frac{2}{x^3}\right) f_2 \omega_{p2}^2}, \tag{3.15}$$

where x is the geometrical aspect ratio $(a_c + a_s)/ac$. The position σ of Pole 2 is plotted as a function of ω_{p2} and γ_2 in Fig. 3.10. We see that, different from the 1-D case, here, when ω_{p2} is larger than a threshold, σ is always positive, no matter how large γ_2 is, meaning the system is always unstable. From the figure, we see that the threshold is not dependent on γ_2, so we assume that the term $\gamma_2^2/4$ under the square root is negligibly small for simplicity. If the argument of the square root is positive, there will be two poles on the real axis, symmetrically located around $-\gamma_2/2$, with one pole likely to fall into the right (unstable) half plane. Instead, if the square root argument is negative, the two poles will have the same real part equal to $-\gamma_2/2$, which is negative, and opposite imaginary parts, which implies that the two poles are stable. As a result, we can write an approximate stability condition:

$$-\omega_{02}^2 - \frac{1}{3}\left(1 + \frac{2}{x^3}\right) f_2 \omega_{p2}^2 < 0, \tag{3.16}$$

which can also be written, in more compact form, as

$$\frac{f_2 \omega_{p2}^2}{\omega_{02}^2} > -\frac{3}{1 + 2/x^3} = S, \tag{3.17}$$

where we have defined the parameter S as the stability threshold. Since the aspect ratio $x \in [1, +\infty)$, we can also write a stricter stability condition as $f_2 \omega_{p2}^2/\omega_{02}^2 > -1$. We also would like to note that, despite having used similar approximations, we managed to write a simple closed-form stability constraint for the 3-D case, whereas the corresponding 1-D condition is a much more complicated and length expression, which may appear counterintuitive. The main reason for this difference is the fact that, in 3-D, we have considered a PEC scat-

terer: the absence of internal fields in the object to be concealed greatly simplifies the calculations. This observation also shows how difficult it is, in general, to define analytical stability criteria for generic scattering problems.

Eq. (3.17) is schematically represented in Fig. 3.11, indicating how the passive/active and stable/unstable nature of the system depends on the parameter $f_2\omega_{p2}^2/\omega_{02}^2$. Clearly, if f_2 is positive, which means that the second Lorentzian resonance is passive, the overall system is always passive and stable. Instead, in the case of an active resonance, i.e., $f_2 < 0$, if $S < f_2\omega_{p2}^2/\omega_{02}^2 < 0$, the system is active and stable; conversely, if $f_2\omega_{p2}^2/\omega_{02}^2 < S$, the system is active and unstable.

The relative permittivity of the active medium, given by Eq. 3.6, can be approximated at the center of the flat region between the two resonances as $\varepsilon_{flat}/\varepsilon_0 \approx 1 - 4\omega_{p2}^2/\omega_{02}^2$, assuming the resonances are well separated and $\omega_{p1} \approx \omega_{p2}$ to have a symmetric dispersion. As discussed above, ε_{flat} needs to match the permittivity ε_2 derived from Eq. (3.1) in order to achieve a cloaking effect. However, since the ratio of ω_{p2} to ω_{02} cannot be large according to the stability condition Eq. 3.17), ε_{flat} cannot be $\ll \varepsilon_0$. This means that it is relatively easy to cloak a PEC scatterer using a stable active shell, as the required ε_2 is between zero and unity. Conversely, for a dielectric sphere, especially when its permittivity is large and positive, the required ε_2 needs to be very negative, which makes it difficult to realize stable broadband active cloaking for a dielectric scatterer. Moreover, if one attempts to broaden the cloaking bandwidth by further separating the two resonances in Eq 3.6 around the central frequency, it is always necessary to increase the ratio $\omega_{p2}^2/\omega_{02}^2$ to keep ε_{flat} matched to the required value, which is likely to push the system to the unstable phase according to Eq. 3.17).

Finally, we also note that Eq. (3.17), derived from quasi-static calculations, typically underestimates σ of Pole 2 with respect to exact dynamic calculations. As a result, Eq. (3.17) is a necessary but not sufficient condition to ensure stable operation. Stability also requires γ_2 to be larger than a small positive value, which should be determined case by case. Similar to the 1-D case, increasing γ_2 is typically beneficial in terms of stability, as it moves Pole 2 toward the left (stable) half plane, but it is detrimental to the cloaking performance since it increases Im $[\varepsilon_2]$.

3.5 Conclusion

In this work, we have explored the potential of active scattering-cancellation cloaks to realize broadband invisibility, based on the anomalous permittivity dispersion enabled by suitable active (gain) media. We have found, for the first time, that active planar cloaks can overcome the bandwidth limits (Bode-Fano limit) that hinder the performance of any passive cloak. This has been achieved with the simplest possible one-layer active cloak, which suggests that there may be significant room for improvement. We have then applied this strategy to a three-dimensional scattering problem, demonstrating significant scattering reduction for a spherical PEC scatterer over a much broader bandwidth than the one achievable with passive scattering-cancellation cloaks. Moreover, we have investigated the issue of stability for both 1-D and 3-D active cloaks. We have found that, in both cases, the active resonance linewidth is required to be larger than a system-dependent threshold to maintain system stability. In the 3-D scenario, we have also found a closed-form expression for an additional stability constraint on the plasma frequency with respect to the active resonance

frequency. Our findings confirm that stability is the main issue that prevents further broadening the bandwidth of active cloaks, but additional research is needed to quantify the ultimate limit imposed by stability in all cases of interest.

We also would like to note that the practical realization of active cloaks may be feasible with current technology. Active materials can be implemented at optical frequencies with gain media (for example dyes, or any material that can sustain population inversion, and therefore an active Lorentzian response) [36]–[39], or, at microwave frequencies, using so-called non-Foster circuit elements [28]–[34], able to implement negative resistances, capacitance, and inductance (which can be obtained using negative impedance converters). We refer the interested readers to [32], [28],[47], for some examples of experimentally implemented active metamaterials. We believe that our results represent important steps in the quest for ultrabroadband invisibility and, more generally, for the realization of active scattering systems with superior performance compared to their passive counterparts. In the context of antenna technology, in particular, active broadband cloaking may enable the realization of low-scattering antenna systems without incurring in the unavoidable bandwidth restrictions imposed by passive cloaks.

We also would like to mention that this work is part of an ongoing debate in the literature, triggered by a recent paper [109], on whether active cloaking based on fast-light propagation can be made ultra-broadband. We have published a separate Matters Arising article on Nature Communications [110], arguing that the cloaking designs in [109] are either non-causal or non-stable and, more broadly, invisibility cloaks made of fast-light media (i.e., materials

supporting superluminal phase and group velocity) cannot achieve arbitrarily broadband operation.

3.6 Appendix

The geometrical and material parameters are all given relative to the central frequency f_c, the central angular frequency ω_c, and the free-space wavelength at the central frequency λ_c. Parameters for 1-D cloaking: $d_1 = \lambda_c/40$, $d_2 = d_1/19.2$, $\varepsilon_1 = 10$, $f_1 = 1$, $\omega_{p1} = 1.72\omega_c$, $\omega_{01} = 0.133\omega_c$, $\gamma_1 = 0.0398\omega_c$, $f_2 = -1$, $\omega_{p2} = 38.5\omega_c$, $\omega_{02} = 3.09\omega_c$, $\gamma_2 = 1.18\omega_c$, $\omega_p = 13.8\omega_c$, $\gamma = 0.0398\omega_c$. Parameters for 3-D cloaking: $a_c = \lambda_c/15$, $a_s = a_c/10$, $f_1 = 1$, $\omega_{p1} = 0.63\omega_c$, $\omega_{01} = 0.283\omega_c$, $\gamma_1 = 0.0281\omega_c$, $f_2 = -1$, $\omega_{p2} = 0.675\omega_c$, $\omega_{02} = 1.41\omega_c$, $\gamma_2 = 0.0281\omega_c$, $\omega_p = 0.948\omega_c$, $\gamma = 0.0281\omega_c$.

CHAPTER 4

BROADBAND ABSORPTION LIMITS FOR ULTRA-THIN SOLAR CELLS

Solar cells with very small thicknesses are advantageous for decreasing materials use and, thus, the total cost per area, but their performance unavoidably deteriorates as the thickness is reduced. Light-trapping techniques have been extensively used to enhance the power absorbed by thin-film solar cells, and their fundamental limits have been investigated in several works. Conversely, less attention has been devoted to the seemingly simpler problem of establishing physical bounds on absorption enhancement based on conventional anti-reflection coatings. In this chapter, we study such bounds on solar power absorption, over the whole solar spectrum, for ultrathin solar cells made of different materials and with antireflection coatings of arbitrary complexity. To this aim, we model the light reflection and absorption problem using impedance concepts and equivalent circuits, and then use the well-established Bode-Fano limits for broadband impedance matching to find the maximum possible absorption. Our results provide relevant insight on the maximum attainable absorption in ultra-thin solar cells without light-trapping, as well as on the performance of different absorbing materials in this context.

4.1 Introduction

Solar energy is one of the most important clean energy technologies available today, and is expected to play a bigger and bigger role in the future. To understand the impact of solar energy for many applications, it is relevant to establish limits and physical bounds on solar energy absorption. Indeed, many different limits have been derived, from different viewpoints, since the inven-

tion of the solar cell, most notably the Shockley–Queisser limit [111] and the Yablonovitch Limit [112]. The Shockley–Queisser limit gives the upper bound on solar energy conversion efficiency of a solar cell made of a single p-n junction [111] (and it can be extended to multiple p-n junctions [113]), while the Yablonovitch limit establishes a bound on light trapping in thick-film solar cells with randomized surfaces. The most crucial step in Yablonovitch's derivation is the ergodicity assumption, according to which an arbitrary incident field will couple equally to all the modes of the solar panel. This equal distribution of energy can be obtained with a randomly roughened surface. Under these assumptions, Yablonovitch derived the maximum absorption enhancement by combining statistical-mechanical methods and ray optics [112].

In recent decades, solar panels have been designed with increasingly thin absorbing layers to decrease materials use and, thereby, lower the cost per aera. When the thickness of the solar panels is decreased to be comparable with the wavelength, or if the light-trapping effect is based on periodic structures with period comparable to the wavelength (nanophotonic regime), a ray optics analysis is no longer valid. To address this problem, Yu et al. derived a more general light trapping limit, valid also in the nanophotonic regime, using coupled-mode theory [114]. In addition, when the solar cell is even thinner, on the same order of the surface roughness, modes are not even well defined, in which case numerical methods are necessary to optimize light trapping design, as done by Ganapati et al. [115]. Note that the absorption enhancement limits mentioned above [112, 114, 115] are in the ergodic regime [112]. Instead, less attention has been devoted to the problem of establishing physical bounds on solar absorption enhancement based on conventional anti-reflection coatings, which are transversely invariant and, therefore, not ergodic [112]. In this case, it is im-

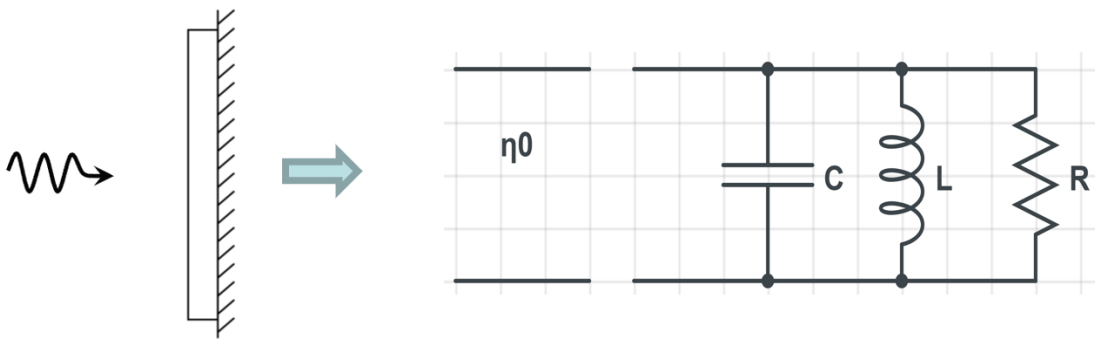

Figure 4.1: Schematic of an ultrathin solar panel under solar light irradiance. Circuit model to capture the local resonance of the solar power absorption.

portant to stress that the antireflection coating cannot be arbitrarily broadband, regardless of its complexity and thickness, as suggested by the Bode-Fano theory of broadband impedance matching [37, 38]. To understand this better, we model the problem of wave reflection from a grounded lossy thin slab with a circuit model that captures the local resonances of the structure. Then, by applying the Bode-Fano theory, we calculate a physical bound on reflection reduction and maximum power absorption over the whole solar spectrum.

4.2 Bode-Fano limits for ultrathin solar cells

As shown in Fig. 4.1, we study solar power absorption in an ultrathin (subwavelength) solar cell. We also assume that solar light is incident from the surface normal for simplicity and that the solar panel is backed by an ideal ground plane (perfect electric conductor) to enhance absorption. In our study, we consider eight typical materials used for solar panels: silicon, GaAs, GaInP, InP, CdTe, methyl ammonium lead iodide (MAPI), organic and copper indium gal-

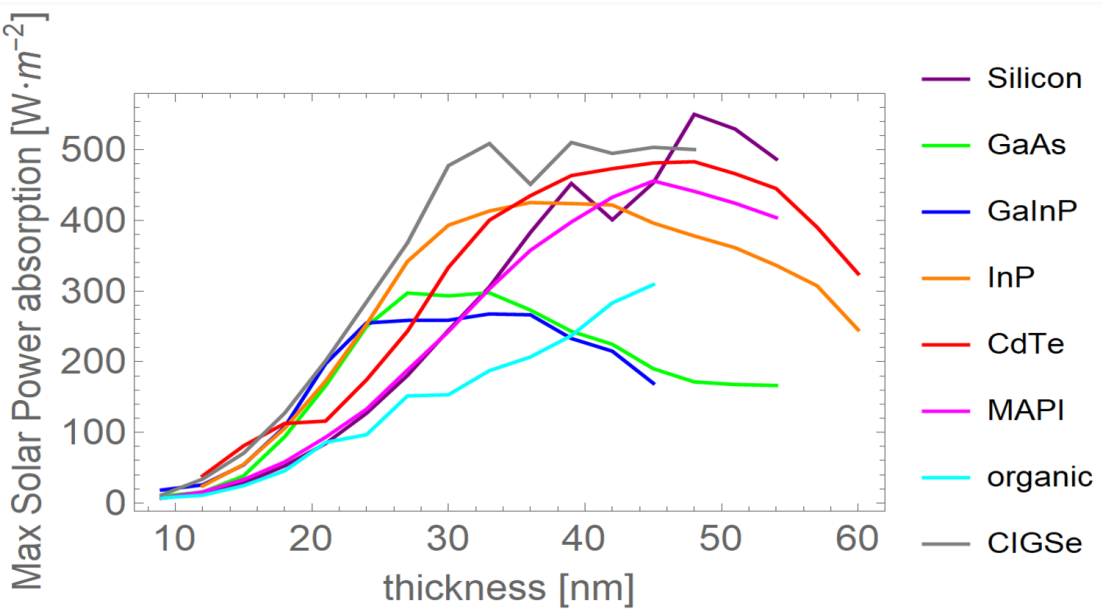

Figure 4.2: Maximum solar power absorption for ultrathin solar panels made of different materials as a function of the thickness of solar panels.

lium selenium (CIGSe). Because of wave impedance mismatch between free space and the absorbing layer, a significant amount of solar energy is reflected at the front face of the solar cell. Since the system has no transmission due to the ground plane, the energy that is not reflected is necessarily absorbed by the solar cell. The total solar power absorption over the whole solar spectrum can be calculated as

$$P = \int_{\lambda_1}^{\lambda_2} \left(1 - |\Gamma(\lambda)|^2\right) S(\lambda)\, d\lambda, \tag{4.1}$$

where Γ is the reflection coefficient, S is standard solar irradiance AM 1.5 [116], λ is the wavelength in free space, and λ_1 and λ_2 are the shortest and longest wavelength between which the solar panel works. Usually, λ_1 and λ_2 are approximately determined by the solar irradiance spectrum and the bandgap of the material.

As mentioned above, to increase solar power absorption, an engineered antireflection coating can be introduced in front of the solar cell, which acts as an impedance matching network between the free-space propagation channel and a load impedance (the grounded lossy slab). Simple anti-reflection-coating designs can easily suppress reflections and greatly enhance absorption at single frequencies or over narrow bandwidths. The situation, however, is much more complicated when trying to optimize solar power absorption over the whole solar spectrum, which spans the entire visible range and beyond. Indeed, the performance of antireflection coatings is bounded by fundamental limits, which can be quantified using the well-established Bode-Fano theory for broadband impedance matching, as typically done in microwave engineering. Considering that the thickness of the solar panel is subwavelength, a simple lumped RLC circuit model of the input impedance is sufficient to capture the local response of the structure. The circuit model is shown in Fig. 4.1, where the RLC load represents the solar cell (i.e., its input impedance), while a semi-infinite transmission line with free-space wave impedance η_0 represents the free-space propagation channel. For broadband impedance matching problems, Bode-Fano limits suggest a tradeoff between reflection suppression and bandwidth, independent of the properties of the matching network, which is just required to be lossless and linear. These limits can be expressed as integral inequalities:

$$\int_{\lambda_1}^{\lambda_2} \ln \frac{1}{|\Gamma(\lambda)|} \cdot \frac{2\pi c}{\lambda^2} d\lambda \leq \frac{\pi}{RC}, \tag{4.2}$$

$$\int_{\lambda_1}^{\lambda_2} \ln \frac{1}{|\Gamma(\lambda)|} \cdot \frac{1}{2\pi c} d\lambda \leq \frac{\pi L}{R}, \tag{4.3}$$

where c is the light speed in free space. When calculating the limits for broadband impedance matching based on these inequalities, one typically assumes a constant reflection coefficient within the frequency band of interest, and total reflection outside this band, to make full use of the integrals in Eqs. (4.2) and (4.3)

[37, 38]. However, in the case under consideration, a flat frequency response for the reflection coefficient is not necessarily optimal, as our goal is to maximize the total power absorbed over the whole solar spectrum taking into account the fact that the solar irradiance is not constant with frequency (it approximately follows a black-body curve). Thus, to maximally absorb the incident solar energy, the optimized reflection should be as low as possible for frequencies at which solar power is high, whereas the requirements on reflection reduction can be more relaxed for frequencies where solar power is low. Accordingly, we have suitably weighted the reflection function in the integrand.

Finally, we plot in Fig. 4.2 the obtained upper bound for the maximum absorbed power as a function of the thickness of the solar cell slab, for the eight materials considered in this study. Several relevant observations should be made: (i) For solar cells made of a specific material, maximum power absorption tends to increase as the thickness of the solar cell increases, up to a material-specific maximum, after which the absorbed power starts to decrease (this peak occurs when the first Fabry-Perot-like resonance of the slab and the material absorption resonance approach each other and overlap with the highest part of the solar spectrum). The value of thickness at which this maximum occurs is the optimal thickness for ultrathin solar cells made of the considered material. Using a larger thickness not only uses more material, but also decreases the performance limit of the solar panel (the maximum absorbed power is then expected to grow again for much larger thicknesses as more modes/resonances become accessible in the slab). (ii) Solar panels made of different materials reach the absorption peak for different thicknesses. We consider two commonly used semiconductor materials as an example. Solar cells made of silicon – an indirect-gap semiconductor exhibiting very weak absorption in the upper half of the visible range

and in the infrared – reach maximum solar power absorption when the thickness is 48 *nm*, while solar cells made of GaAs – a direct-gap semiconductor – can already reach, in theory, 300 W/m^2 when the thickness is only 26 *nm*. As shown in Fig. 4.2, other materials exhibit even better performance.

4.3 Conclusion

We have established broadband absorption limits for ultrathin solar panels made of various materials, where absorption is enhanced by arbitrary anti-reflection coatings, without any light-trapping strategy. The limits have been derived by applying the well-established Bode-Fano theory of broadband impedance matching. This work provides important information and insight for the design of optimal absorption for ultra-thin solar cells. The next step of this work would be to calculate the actual efficiency limit of the solar cell device, based on a Shockley-Queisser analysis for single [111] or multiple p-n-junctions [113], for the maximum optical absorptance allowed by the Bode-Fano limit.

CHAPTER 5

TOWARDS COMPACT ANALOG OPTICAL COMPUTING PLATFORMS BASED ON METASURFACES AND METAMATERIAL-WAVEGUIDE NETWORKS

5.1 Introduction

The invention and development of digital electronic computers is one of the most ground-breaking scientific and technological breakthroughs in human history. While digital electronic computers can perform information processing for general purposes, the ever-increasing demands for processing extraordinarily large amounts of data are testing the limits of digital electronic computing, especially in terms of bandwidth and energy consumption. To alleviate these problems, digital optics was proposed as a possible candidate for the next generation of logical elements [117]; however, at this stage, no optical switch can compete, qualitatively or quantitatively, with electronic transistors [118]. A much more promising direction is the design of *analog* optical information processors, which have been recently proposed for special computing purposes (image processing, vector-matrix multiplications, inference, etc.), potentially serving as hardware accelerators for current digital architectures [119, 120].

The past two decades have witnessed the advent and rapid progress of optical metamaterials and nanophotonic structures, which enable tailoring the flow of light with unprecedented flexibility over small footprints. Modulating the amplitude, phase and/or polarization of electromagnetic waves has been achieved successfully by different mechanisms, e.g., optical-resonator-based metasurfaces [121, 122], meta-transit-arrays [123], metamaterial Huygens sur-

faces [124], etc. This unprecedented degree of control has allowed designing metamaterials and nanophotonic structures that perform basic analog operations and image processing [2, 125, 126, 127, 128, 129, 130, 131, 132, 133]. Recently, compact optical designs have also been proposed to solve equations based on Fourier optics configurations [134, 135] or inverse designed metastructures [136].

The topic of wavefront manipulation, which is one of the main themes of this dissertation, is clearly very relevant within the context of optical analog computing. In this chapter, we discuss how to engineer the wavefront of propagating waves using a modular platform that implements more general analog computing operations. This platform is based on the framework of metamaterial-waveguide-networks [137], which include combinations of optical waveguides, graded-index (GRIN) lenses, mirrors, beam splitters, and, most importantly, metasurfaces. We propose and computationally demonstrate several representative design examples to perform fractional calculus of an arbitrary order, to calculate a weighted sum of proportional-integral-derivative (PID) operations on an input function, and to solve fractional calculus equations. The proposed designs mostly follow the conceptual blueprint of Fourier optics, with GRIN lenses to perform spatial Fourier transforms and metasurfaces as spatial-frequency filters, however all designs have a small footprint of only a few wavelengths, orders of magnitude smaller than conventional Fourier optics systems.

It should also be noted that the word "computing" is used here (as well as in most of the literature on analog optical computing) in a loose sense, encompassing also passive analog devices performing specific operations. Indeed, one of the main challenges of optical computing systems remains the inclusion of

strong nonlinearities and reprogrammabable elements; however, in recent years there have been some promising advances, such as hybrid electronic-photonic platforms that can be used as accelerators for inference tasks [138]. While the structures discussed in this chapter are still passive, we note that their modular designs may enable future extensions that include nonlinear, active, and reprogrammable elements.

5.2 Compact wave-based analog computing platform and device designs

For the present discussion, we assume monochromatic operation with a frequency of 100 THz (an $\exp(-i\omega t)$ time-harmonic convention is assumed for all field quantities). For simplicity, all our designs are analyzed in two dimensions in the x-O-y plane and we have assumed a transverse electric (TE) field, i.e., the electric field has only a non-zero z component. First, we show a design for the basic computational element for fractional calculus operations [139, 140] (including fractional integral and derivative) of an input signal, based on the proposed platform. This basic computational element serves as the central component in the following analog computing designs. There are many equivalent approaches to define fractional calculus based on different mathematical considerations. Here, we exploit the Fourier transform properties of fractional calculus, which are compatible with our compact Fourier optical implementation. Given an input field profile with zero spatial average (its spatial spectrum is zero for zero spatial frequency), its a^{th}-order fractional integration (derivative

also included) can be written as

$$ {}_{-\infty}D_y^{\alpha} f(y) = F^{-1}\left\{\left(ik_y\right)^{-\alpha}\left(F\{f(y)\}\right)\left(ik_y\right)\right\}, \tag{5.1} $$

where α is the order of fractional integration (an extra term should be added if the input field contains zero-spatial-frequency components). When α is positive, Eq. (5.1) represents a fractional order integration; when α is negative, it represents a fractional derivative; when α is 0, it gives the original function; $-\infty$ is the lower limit of the integration; F and F^{-1} represent Fourier and inverse Fourier transforms in spatial domain.

For the optical implementation of generic fractional calculus operations, we use a compact solid-state version of a Fourier optics setup, with two quadratic GRIN lenses [141] to perform Fourier transforms and a metasurface [123] sandwiched between the lenses acting as a spatial frequency filter [2]. The relative permeability of the GRIN lens is 1 and the relative permittivity follows [141]

$$ \varepsilon(y) = \varepsilon_c\left[1 - \left(\pi/2L_g\right)^2 y^2\right], \tag{5.2} $$

where ε_c is the relative permittivity at the center axis ($y = 0$) and L_g is the focal length of the GRIN lens. When a beam of light, whose transverse (y-direction) profile carries the input signal, is fed into the GRIN lens, the signal in real spatial domain converts into the spatial-frequency domain (momentum domain) after a propagation length equal to the focal length of the GRIN lens. After spatial frequency filtering by the metasurface, the signal is transformed back into the real spatial domain by another GRIN lens. For derivative and integral operations, the filters need to implement a low-pass and high-pass response with logarithm profiles, respectively. For simplicity, we use an idealized metasurface in the simulations, as in [2]. For the differentiator design, the relative permeability and relative permittivity of the idealized metasurface filter has a spatial

transverse profile along the y direction

$$\frac{\varepsilon(y)}{\sqrt{\varepsilon_c}} = \mu(y) \cdot \sqrt{\varepsilon_c} = \frac{i\alpha\lambda_0}{2\pi\Delta} \ln\left(-\frac{iW}{2y}\right), \tag{5.3}$$

where Δ is the thickness of the metasurface filter in the longitudinal direction x, and W is the width of the system, respectively. Similarly, for integrators, we have

$$\frac{\varepsilon(y)}{\sqrt{\varepsilon_c}} = \mu(y) \cdot \sqrt{\varepsilon_c} = \left\{\frac{i\alpha\lambda_0}{2\pi\Delta} \ln\left(-\frac{iy}{d}\right),\ |y| > d;\ -\frac{\lambda_0}{4\Delta}\text{sign}\left(\frac{y}{d}\right),\ |y| < d\right\}, \tag{5.4}$$

where d is the distance from the center of the filter along $\pm y$ direction at which the imaginary part of the relative permittivity is truncated to be 0 to maintain passivity of the system (therefore avoiding the need for gain media) [2].

An example of fractional calculus operational element is shown in Fig. 5.1. The real and imaginary parts of the relative permittivity of the metasurface are shown in Fig. 5.1 (a) and (b). The permeability parameters are equal to the permittivity parameters for impedance matching in this idealized scenario. We see that both the real and imaginary part of the relative permittivity change gradually as α increases from -1 to 1. As discussed above, we avoid using active (gain) materials in the system, so the imaginary part of the relative permittivity of the metasurface is always positive. Specifically, for the differentiator design, where the metasurface filter has a high pass response, we require that the loss is zero at the edges ($y = \pm W/2$) of the filter. Therefore, the metasurface filter is passive and energy loss is minimized when signal travels through the filter, ensuring a relatively high amplitude of the output signal. For integrators, it is not possible to realize perfect spatial filters while maintaining the passivity of the system. This is because the ideal spatial frequency response for an integrator is a low-pass filtering behavior with a logarithm profile; therefore, in the near-zero spatial frequency region ($|y| < d$), the spatial-frequency components should

be amplified. As is done in reference [2], we instead force the imaginary part of the relative permittivity in this region to be zero, as shown in Fig. 5.1(b). If the value of d is properly optimized, we get a relatively large output signal with negligible distortion. Figs. 5.1 (c) and (d) give the real and imaginary parts of the output of the fractional-order integration/differentiation, when the input signal is the first-order derivative of a Gaussian function. We see that the real part of the wave profiles matches the analytical results (purely real) very well, and the imaginary part of the wave profiles is correctly suppressed to very small values.

Next, we demonstrate manipulation of wave propagation in a metamaterial waveguide network designed to act as an analog wave-based PID (Proportional Integral Derivative) controller of arbitrary weights. The design schematics of the PID controller is shown in Fig. 5.2 (a). The input signal in real spatial domain is first transformed into spatial-frequency domain by a GRIN lens. Then, in the Fourier-domain region, there are three channels, individually performing proportional, integral and derivative operations. Finally, the signals from all three channels merge, and are transformed back into real spatial domain by another GRIN lens. The weight of each operational element is controlled by adjusting the losses of the metasurface filters. It should also be noted that phase adjustment is necessary to ensure the signals from all three channels add up constructively at the output. Fig. 5.2 (b)–(d) shows the input signal, the output signals through the three individual PID channels, and the output signal through the entire PID network, compared against analytical results. Good agreement is observed in all cases.

In the spatial-frequency domain, which is denoted in green in Fig. 5.2 (a),

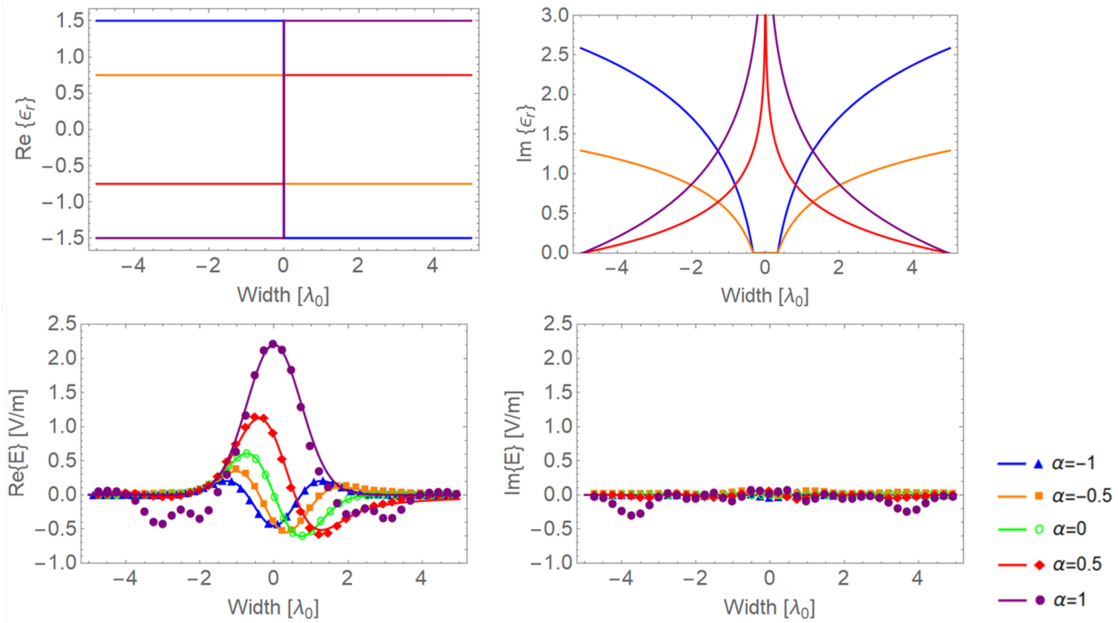

Figure 5.1: Real (a) and imaginary (b) parts of the relative-permittivity profiles of the metasurface filters for α^{th}-order fractional-calculus operations. Real (c) and imaginary (d) parts of the output of the wave-based operational elements against the analytical results, which are purely real. In all the figures in this chapter, solid lines represent analytical results, while markers represent simulation results from the RF module of COMSOL Multiphysics. The dimensions of the operational elements and the material parameters of the GRIN lens are the same as those in Ref. [2]. The input signal is the first-order derivative of a Gaussian function with expectation $\mu = 0\ \mu$m and standard deviation $\sigma = 2.2\ \mu$m.

waves propagate in a homogeneous medium, not a graded-index lens, and therefore suffer from diffraction and beam broadening. Beam broadening in spatial-frequency domain causes beam shrinking in real spatial domain, which explains the distortion of the output signals against the analytical results. To avoid waveform distortion from diffraction and simplify the structure at the same time, we could combine the functionality of the three metasurface filters into one, so that no dielectric waveguide would be needed. However, perform-

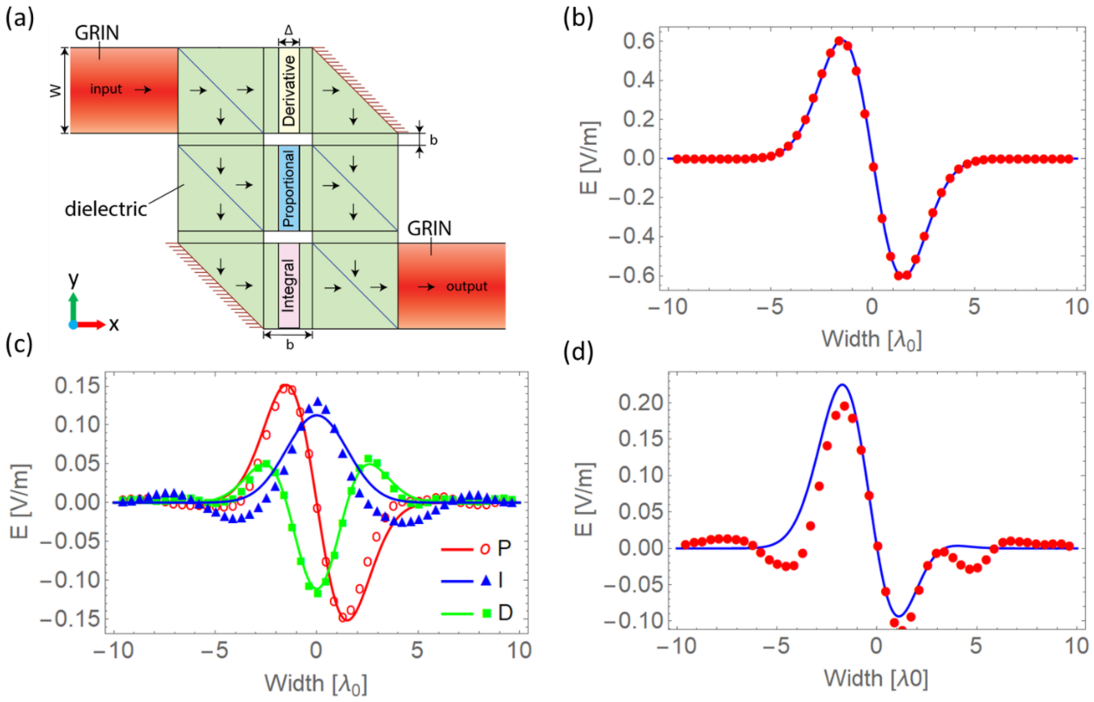

Figure 5.2: (a) Schematic of the compact wave-based PID controller. Directions of propagation are indicated with arrows. The width of the GRIN lens is 60 μm. (b) Input signal of the PID controller is the first-order derivative of a Gaussian function with standard deviation σ = 4.5 μm. (c) Output of the individual PID blocks. (d) Output of the entire PID controller.

ing proportional, integral and derivative operations separately makes it easier to adjust their specific weights without redesigning the filter.

Finally, we further demonstrate the power of this wave-based computational paradigm by designing fractional calculus equation solvers. A linear constant-coefficient ordinary fractional calculus equation can be expressed as

$$2O - HDO = I, \tag{5.5}$$

where I is the input signal (driving function); O is the output signal; D is a fractional calculus operator; and H is a constant coefficient. The block diagram

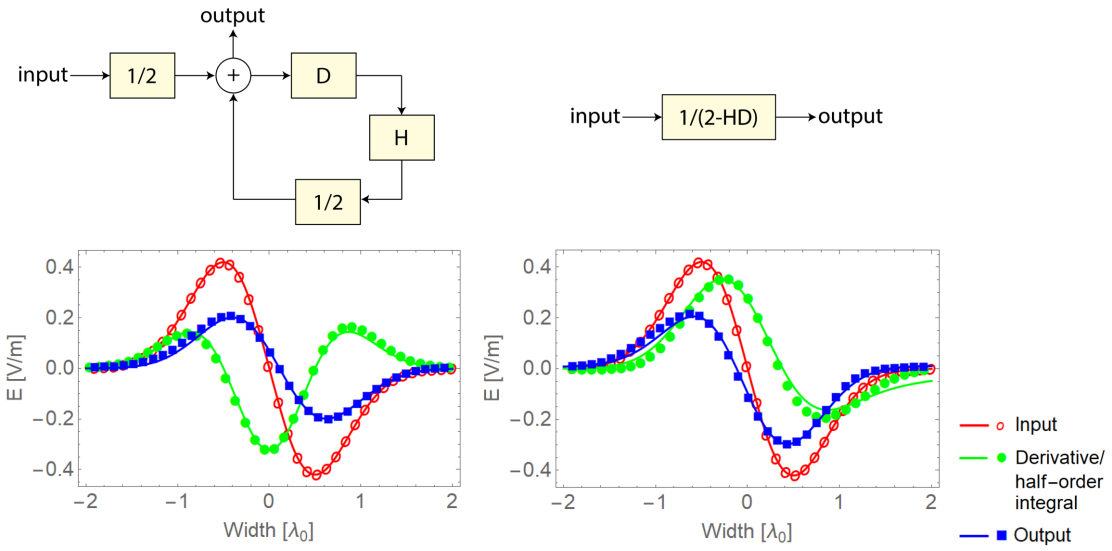

Figure 5.3: (a) Block diagram representation of the feedback system corresponding to Eq. (5.5). (b) Block diagram representation of the equivalent direct system. (c) Results of the first-order differential equation solver. (d) Results of the half-order integral equation solver. The excitation signal for both cases is the first-order derivative of a Gaussian function with standard deviation $\sigma = 1.5\ \mu$m.

representation of this equation is given in Fig. 5.3 (a), which is a feedback loop. To implement such an optical feedback network, the output of the fractional calculus operation should be routed back into the input. However, realizing this configuration with minimal wave diffraction and distortion would require four GRIN lenses to perform Fourier and inverse-Fourier transforms and relay the signal back to the input without diffraction, which would make the optical structure long and bulky. However, after a closer inspection of the system diagram, it is clear that the system can be designed in a more direct fashion by implementing the entire transfer function with a suitable spatial frequency filter, as shown in Fig. 5.3 (b) (the downside of this design solution is that it would be more difficult to vary the individual terms of the equation without redesign-

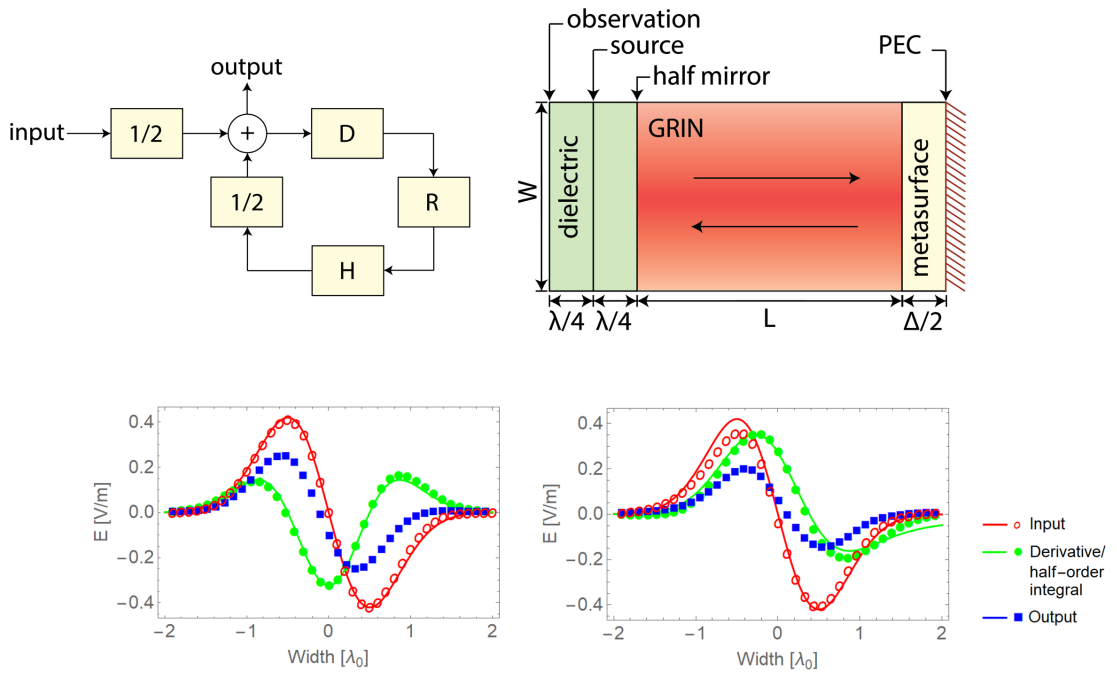

Figure 5.4: (a) Block diagram representation of the feedback system corresponding to Eq. (5.6). (b) Schematics of the cavity-based fractional-calculus equation solver. Dimensions of the optical structure are shown in the figure, where W, L and Δ are 12 μm, 14.45 μm and 0.5 μm, respectively. (c) Results of the first-order differential equation solver. (d) Results of the half-order integral equation solver. The excitation signal for both cases is the first-order derivative of a Gaussian function with standard deviation σ = 1.5 μm.

ing the filter). The results for a first-order differential equation and a half-order integral equation are shown in Figs. 5.3 (c) and (d).

Not all feedback systems corresponding to fractional calculus equations can be converted to a direct system as above. A simple example is when there is an argument inversion after the fractional calculus operation. Argument inversion R of a function $f(t)$ is defined as $R[f] : t \rightarrow f(-t)$. Consider an equation

$$2O - HRDO = I. \tag{5.6}$$

For such a problem, we resort to the optical feedback network in Fig. 5.4 (a). Instead of using a traditional optical feedback loop, which is bulky and may suffer from field distortions, we implement a feedback mechanism through a Fabry–Pérot interferometric cavity, essentially using the same GRIN lens twice. Our proposed structure shown in Fig. 5.4(b) – the topology of which can be shown to be equivalent to that of Fig. 5.4(a) – is drastically more compact and distortion-free because waves travel mainly inside the GRIN medium.

Let us analyze the optical path in the cavity structure. When the input beam hits the half mirror, half of the signal intensity enters the GRIN lens and is transformed into the spatial-frequency domain at the right side of the lens. It then enters the metasurface filter of half of the designed thickness, is reflected by the perfect (PEC) mirror, and travels another half of the metasurface thickness, thereby completing the required spatial-frequency-domain processing. The backward propagating wave travels through the GRIN lens for the second time to be transformed back into real spatial domain. At the half mirror, half of the signal bounces back into the GRIN medium as feedback, and half propagates through and reaches the observation plane together with half of the input signal. In Fig. 5.4 (c) and (d), in Figs. 3 (c)-(d), we give two examples of using this system to solve a first-order differential equation and a half-order integral equation. We observe very good agreement between simulated results for our wave-based equation solver and the analytical results.

In principle, there is no lower limit to the longitudinal size of the structure in Fig. 5.4, since diffraction is suppressed in the GRIN medium. However, in practice, the more compact the structure is, the more extreme the required permittivity profile of the GRIN lens becomes. In such a case, the wave impedances

at the center ($y = 0$) and the edge ($y = \pm W/2$) of the GRIN lens will have a significant contrast, leading to difficulties in impedance-matching the GRIN medium with the rest of the structure. In our design, the size of the system is chosen to be approximately $4\lambda_0 \times 4\lambda_0$, where λ_0 is the free-space wavelength.

5.3 Conclusion

In this chapter, we have discussed the design of basic fractional-calculus operational elements based on ultra-compact Fourier-optics configurations involving GRIN lenses and metasurfaces. Then, we have shown that these basic elements can be combined in a metamaterial waveguide network to act, for example, as an analog wave-based PID controller. Finally, we have presented and computationally demonstrated compact optical structures that solve linear constant-coefficient ordinary fractional calculus equations. The footprint of the wave-based solver is as small as approximately $4\lambda_0 \times 4\lambda_0$, orders of magnitude smaller than conventional Fourier-optics systems. We are currently planning the experimental demonstration of some of these designs. Moreover, further work may be done to extend the proposed analog computing platforms to solve nonlinear, variable-coefficient, partial differential equations.

5.4 Appendix: Analysis of wave propagation in a GRIN lens

In this section, we provide a detailed theoretical analysis of waves on 1-D GRIN lenses, and their ability to produce the spatial Fourier transform of an input function. A schematic of wave propagation in a GRIN lens is shown in Fig. 5.5.

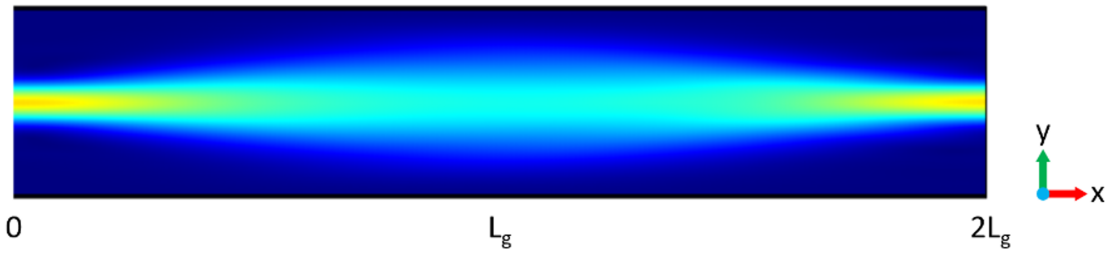

Figure 5.5: Gaussian beam propagation in a GRIN lens. In the figure, L_g is the focal length of the GRIN lens.

The wave equation in a 1-D GRIN lens is [142, 143]

$$\nabla^2 E_z + k_0^2 n^2 E_z = 0, \tag{5.7}$$

where

$$n^2 = \varepsilon_c \left[1 - \left(\pi/2L_g\right)^2 y^2\right], \tag{5.8}$$

Note that this equation is not exact, as it ignores the derivative of the material parameters [144, 145]. After proper approximations, this equation is of the same type as that of a quantum harmonic oscillators [146]. The solution of this differential equation is a weighted sum of transverse (y-direction) Hermite-Gaussian functions with a propagation factor in the longitudinal x-direction [142, 143]

$$E_z(x,y) = \sum_n A_n E_z^{(n)}(x,y) = \sum_n A_n \Psi_n(y) \exp(i\beta_n x), \tag{5.9}$$

where

$$\Psi_n(y) = H_n\left(\frac{\sqrt{2}y}{\Omega}\right)\exp\left(-\frac{y^2}{\Omega^2}\right), \tag{5.10}$$

with

$$\omega = 2\left(\frac{L_g}{\pi k}\right)^{1/2}, \tag{5.11}$$

and

$$\beta_n = k\left[1 - \frac{\pi}{kL_g}(n+1)\right]^{1/2} \simeq k - \frac{\pi}{2L_g}(n+1). \tag{5.12}$$

Here k is the wave number on the axis ($y = 0$) of the GRIN lens. As is shown in Refs. [142, 143], the Fourier transform of the n^{th} Hermite-Gaussian function is

$$\tilde{E}_z^{(n)}\left(0, k_y\right) = \int_{-\infty}^{+\infty} \Psi_n(y) \exp\left(-i2\pi k_y y\right) dy = s\Psi_n\left(k_y s^2\right) \exp\left(-in\pi/2\right), \tag{5.13}$$

where

$$s = \omega\sqrt{\pi}, \tag{5.14}$$

and $\Psi_n(y)$ and $\tilde{\Psi}_n\left(k_y\right)$ are input signals in real spatial domain and spatial-frequency domain, respectively. If the nth mode propagates a distance of L_g, the focal length of the GRIN lens, we obtain

$$E_z^{(n)}\left(L_g, y'\right) = \exp\left(ikL - i\frac{\pi}{2}\right)\Psi_n(y') \exp\left(-in\frac{\pi}{2}\right), \tag{5.15}$$

where we have used y' to represent the transverse position at $x = L_g$. If we take this quantity to represent a scaled version of the transverse wavenumber:

$$y' = k_y s^2, \tag{5.16}$$

then we have

$$E_z^{(n)}\left(L_g, y'\right) = -\frac{i\exp\left(ikL_g\right)}{s}\tilde{E}_z^{(n)}\left(0, k_y\right) = -\frac{i\exp\left(ikL_g\right)}{s}\tilde{E}_z^{(n)}\left(0, y'/s^2\right). \tag{5.17}$$

This shows that, for any mode n, the GRIN lens produces its spatial Fourier transform at $x = L_g$, with only a uniform amplitude and phase difference compared to the exact solution. Considering the completeness and orthogonality of Hermite-Gaussian functions, which can therefore be used to represent a generic field distribution, the GRIN lens produces the spatial Fourier transform, at $x = L_g$, for any input functions. However, while for each eigenmode of order n the width of the field profile does not change when propagating in the GRIN lens, for generic input functions we observe beam broadening or shrinking, since different modes have different wavenumbers and, therefore, they superpose constructively and destructively as they propagate.

Next, we show that a wave profile in the real spatial domain returns to the real spatial domain, but mirrored along the y axis, after propagating in a GRIN lens for a distance of $2L_g$, with no amplitude scaling but with a phase factor. This can be seen in two different ways. First, when an input signal propagates for a distance of $2L_g$

$$E_z^{(n)}\left(2L_g, y''\right) = E_z^{(n)}(0, y)\exp\left(i\beta_n 2L_g\right) = (-1)^{n+1}\exp\left(ik2L_g\right)\Psi_n(y''). \tag{5.18}$$

where we have represented the transverse position at $2L_g$ with y''. According to the properties of Hermite functions, when n is odd, $\Psi_n(y)$ is odd; when n is even, $\Psi_n(y)$ is even, so

$$E_z^{(n)}\left(2L_g, y''\right) = -\exp\left(ik2L_g\right)\Psi_n(-y''), \tag{5.19}$$

which proves that the output is the same as the input, but mirrored along the y direction and with an additional phase factor.

We can also prove this directly from the Fourier transform properties of the GRIN lens. We have shown above that at $x = L_g$,

$$E_z^{(n)}\left(L_g, y'\right) = -\frac{i\exp\left(ikL_g\right)}{s}\tilde{E}_z^{(n)}\left(0, y'/s^2\right) \tag{5.20}$$

$$= -\frac{i\exp\left(ikL_g\right)}{s}\int_{-\infty}^{+\infty}\Psi_n(y)\exp\left(-i2\pi yy'/s^2\right)dy, \tag{5.21}$$

so, at $x = 2L_g$,

$$E_z^{(n)}\left(2L_g, y''\right) = -\frac{i\exp\left(ikL_g\right)}{s}\tilde{E}_z^{(n)}\left(L_g, y''/s^2\right) \tag{5.22}$$

$$= -\frac{\exp\left(i2kL_g\right)}{s^2}\int_{-\infty}^{+\infty}\int_{-\infty}^{+\infty}\Psi_n(y)\exp\left(-i2\pi yy'/s^2\right)dy\exp\left(-i2\pi y'y''/s^2\right)dy' \tag{5.23}$$

$$= -\frac{\exp\left(i2kL_g\right)}{s^2}\int_{-\infty}^{+\infty}\int_{-\infty}^{+\infty}\Psi_n(y)\exp\left(-i2\pi yk_y\right)dy\exp\left(-i2\pi y'y''/s^2\right)d\left(s^2k_y\right) \tag{5.24}$$

$$= -\exp\left(i2kL_g\right)\int_{-\infty}^{+\infty}\left[\int_{-\infty}^{+\infty}\Psi_n(y)\exp\left(-i2\pi yk_y\right)dy\right]\exp\left[i2\pi k_y(-y'')\right]dk_y \tag{5.25}$$

$$= -\exp\left(i2kL_g\right)\Psi_n(-y''), \tag{5.26}$$

which is the same as Eq. (5.19).

CHAPTER 6

NONLOCAL METASURFACES FOR SPACE COMPRESSION

6.1 Introduction

Optical systems aim to control the flow of light for different applications, such as imaging, spectroscopy, sensing, light concentration, etc. Lenses, which are the essential component of most optical systems, control light by locally molding the phase of a propagating wave through its interaction with a transversely inhomogeneous structure. Alternatives to conventional curved lenses have been investigated for centuries to miniaturize optical systems and/or achieve better optical performance (a notable example is the Fresnel lens) [144]. However, drastic progress in lens miniaturization has only been achieved recently with the advent of the field of flat optics and the introduction of increasingly advanced metasurfaces and metalenses [147, 121, 122, 148, 123, 124, 149, 150, 151, 152, 153, 154, 22, 155, 156, 21, 23]. Regardless of the specific design, the local phase profile that a metalens needs to implement to realize focusing is

$$\varphi(r) = -k_0\left(\sqrt{F^2 + r^2} - F\right) + g, \tag{6.1}$$

where k_0 is the wavenumber in the surrounding medium at the operating frequency ω_0, r is the radial coordinate in the transverse direction, F is the focal length of the metalens and g is a reference phase, independent of position but possibly dependent on frequency. Throughout this work we assume a $e^{-i\omega t}$ time-harmonic convention for all field quantities.

While the field of metasurfaces holds promise to revolutionize optics by replacing bulky conventional lenses with compact planarized devices, simply

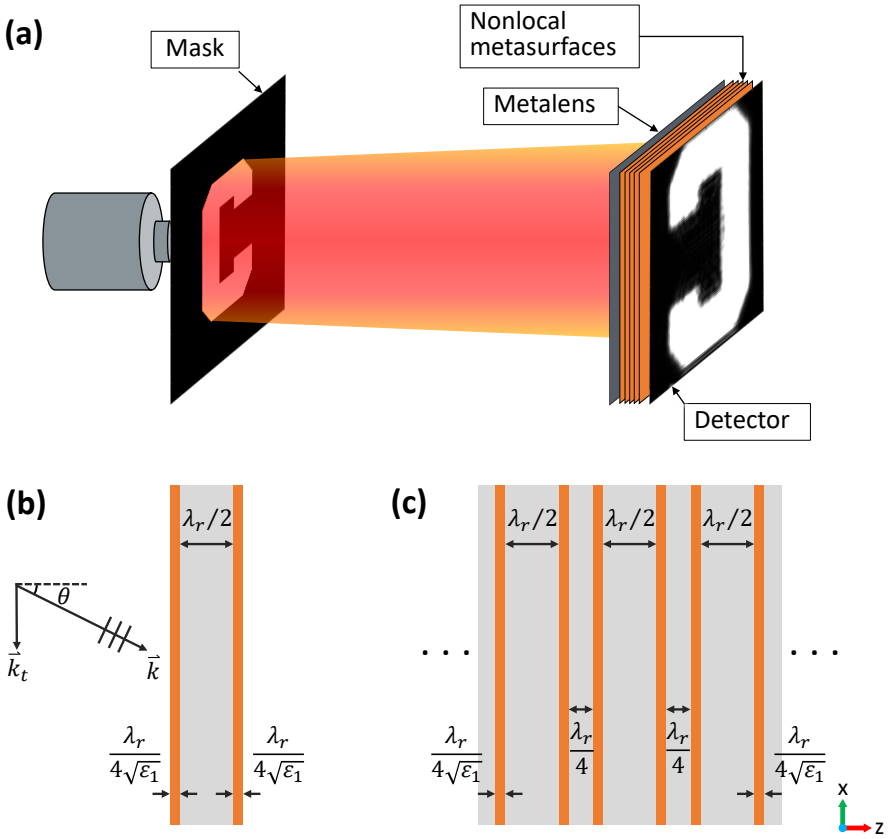

Figure 6.1: (a) Illustration of a ultra-thin, fully solid-state, flat-optics imaging system, in which nonlocal metasurfaces replace and compress the entire free-space volume between a flat metalens and the detector on the observation plane, hence miniaturizing the entire optical system without affecting the imaging performance. (b) Planar dielectric structure supporting a guided-mode resonance, as an example of the simplest possible design that can implement the nonlocal response in Eq. (6.2). The two dielectric plates (orange) have moderately high relative permittivity ε_1 and are separated by a material with relative permittivity close to unity (grey). Relevant dimensions are shown in the figures, where λ_r is the free-space wavelength at the resonant frequency, ω_r, of the first even Fabry-Pérot-like resonance of the structure. (c) n-layer structure acting as a nonlocal metasurface, in which individual resonators are separated by quarter-wavelength spacers to obtain approximately uniform transmission amplitude and linear phase with respect to frequency, as discussed in the text.

making lenses flat and thin is not sufficient to miniaturize the vast majority of real-world optical systems. In fact, a significant percentage of the volume of an optical system (for example, a microscope, a telescope, or a Fourier optical processor) is composed of free space. Empty space between lenses is needed to allow light to propagate, acquire an angle-dependent phase delay, and achieve focusing at a desired point. However, only very recently attention has started to be given towards the problem of systematically miniaturizing this empty space between solid-state optical components, e.g., lenses and detectors [157, 158].

To better understand how to approach this problem, let us consider the transfer function for plane waves propagating through a free-space volume of length L. While the transmission amplitude is unity for propagating waves in free space, the transmission phase is a function of the transverse wavenumber (momentum) k_t as

$$\varphi(k_t) = L\sqrt{k_0^2 - k_t^2} \approx k_0 L - \frac{L}{2k_0}k_t^2, \tag{6.2}$$

where the expression on the right is a Taylor expansion of the transmission phase for small k_t. Thus, in order to replace a free-space segment of length L with a planar device of thickness $T << L$, the designed structure should have the same optical response. Then, a "squeezing ratio" can be defined as $R = L/T$. Most importantly, it is clear from Eq. (6.2) that the required transmission phase response of such a "space-squeezing device" depends directly on the transverse momentum k_t, and not on the spatial location r, indicating that the response of the desired device should be "nonlocal" [7].

To clarify the terminology further, conventional metasurfaces and metalenses are "local" in the sense that they control the wave transmission/reflection as a function of position (locally and pointwise) as in Eq. (6.1), based on an

engineered *transversely inhomogeneous* structure, to achieve for example beam focusing or deflection. In this regard, while huge research efforts have been devoted to metasurfaces in recent years, their operation is not fundamentally different from other transversely inhomogeneous optical devices, such as conventional lenses and gratings. In drastic contrast with such local devices, a nonlocal metasurface is a planar device designed to control the transmission as a function of the transverse wavenumber k_t, based on a transversely homogeneous but *longitudinally inhomogeneous* (e.g., layered) structure. In other words, since the k_t-dependent transmission function corresponds to the angular transfer function of the device, nonlocal flat optics aims to provide a novel approach to systematically control the angular transmission response. While three-dimensional nonlocal metamaterials, with wavevector-dependent constitutive parameters, have been studied extensively in the past, the field of nonlocal flat optics – which was pioneered in the context of wave-based analog optical computing [2, 103, 133, 159] – is still in its infancy.

The idea of applying nonlocal flat structures to the problem of compressing empty space in optical systems was originally proposed, very recently, in Refs. [157] and [158]. Specifically, Ref. [157] demonstrated a space-squeezing effect using low-index isotropic and anisotropic slabs in a high-index background, as well as using optimized multilayered structures, whereas Ref. [158] considered a modified photonic-crystal slab achieving the same effect. However, these early designs suffer from fundamental and practical problems, which hinder their practical potential and applicability. The structures proposed in [157] operate over a moderately large range of transverse wavenumbers (angular range), but can only replace a limited length of free space (in addition, the only reported experimental demonstration was based on a high-index background, making it

impractical for most applications). Conversely, the photonic-crystal device in [158] can replace a much longer free-space volume, but the angular range of the device is very limited.

Within this context, the goal of this work is three-fold: (i) We first discuss why some of these limitations are fundamental for a broad class of nonlocal metasurfaces based on a single guided-mode resonance. Specifically, we derive a quantitative trade-off between the length of replaced free space L and the operating range of transverse momentum k_t, which explains the limited performance achieved in previous works. (ii) We then propose a solution to relax this trade-off, based on a stack of suitably coupled dielectric resonators, realizing a nonlocal metasurface device that can replace free-space regions of arbitrary length over a wide angular range. (iii) Finally, we theoretically and computationally demonstrate, for the first time, the potential of combining local and nonlocal metasurfaces to realize fully solid-state structures for focusing and imaging, as illustrated in Fig. 6.1(a), in which the actual distance where focusing is achieved is fundamentally decoupled from the focal length of the lens (and hence its magnifying power).

6.2 Fundamental Trade-offs and Nonlocal Metasurface Design

6.2.1 Nonlocal structures based on a single guided-mode resonance – Operational principle and trade-offs

In order to better understand the physics and design trade-offs of nonlocal space-squeezing devices, we first consider one of the simplest possible planar structures that can implement the nonlocal phase function in Eq. (6.2), by relying on a guided-mode resonance, as in Ref. [158]. Fig. 6.1(b) shows the structure under consideration, which is essentially a simple dielectric resonator comprised of two quarter-wavelength-thick dielectric plates (acting as mirrors with relatively large, real, reflection coefficient), spaced by half a wavelength at the resonant frequency, ω_r, of the first even Fabry-Pérot-like resonance at normal incidence. The spacer layer is assumed to be made of a material with relative permittivity equal to unity (but any transparent material that provides enough contrast with the dielectric plates would also work, as further discussed below). Under oblique plane-wave incidence with transverse wavenumber $k_t = k_0 \sin\theta$, at a frequency near ω_r the transmission coefficient can be described locally by a single-resonance model (see Eq. (6.17))

$$t(\omega, k_t) = \frac{\gamma_0}{\gamma_0 - i(\omega - \omega(k_t))}, \tag{6.3}$$

where γ_0 is the resonance linewidth, which is assumed to be invariant with k_t, and $\omega(k_t)$ is the dispersion relation of the resonant mode, namely, the dispersion relation of the guided leaky mode responsible for the Fabry-Pérot-like resonance. The transmission phase at frequencies near the eigenfrequency $\omega(k_t)$ of

the guided mode is

$$\arg(t) = \arctan\frac{\omega - \omega(k_t)}{\gamma_0} \approx \frac{\omega - \omega(k_t)}{\gamma_0}. \tag{6.4}$$

from which we see that the near-resonance transmission phase is approximately a linear function with respect to ω or $\omega(k_t)$. Considering the exact expression in Eq. (6.4), we also note that the phase varies around the resonance (varying either ω or k_t) in a limited range from $-\pi/2$ to $\pi/2$, as expected. This already indicates the inherent limitation of using a single guided-mode resonance to implement the phase function in Eq. (6.2), which generally requires an available phase range much wider than π to replace a free-space volume of large length over a wide range of k_t.

As detailed in the Appendix, it can be shown that the dispersion relation of the considered resonance of the structure in Figure 6.1(b) is approximately a quadratic function for relatively small values of k_t (small incidence angles) (see Eq. (6.26)):

$$\omega(k_t) \approx \omega_r + \alpha k_t^2. \tag{6.5}$$

An approximate expression for the coefficient α of the second-order term for the structure under consideration is given in the Appendix, Eq. (6.27). Combining Eqs. (6.4) and (6.5), we get

$$\arg(t) \approx \frac{\omega - \omega_r}{\gamma_0} - \frac{\alpha}{\gamma_0}k_t^2. \tag{6.6}$$

Thus, the transmission phase of the considered structure, acting as a nonlocal k_t-dependent metasurface, has the same form as that of free space, given by Eq. (6.2). We also note that, similar to Eq. (6.2), Eq. (6.6) only has even-order terms, which is expected since both free space and the considered structure are transversely mirror-symmetric, hence the transmission response is the same for plane waves with opposite transverse wavenumbers, k_t and $-k_t$.

As noted in [157] and [158], a global k_t-independent transmission-phase difference between the space-squeezing device and free space is irrelevant. Thus, we neglect the zero-order terms and, comparing the coefficients of the quadratic terms in Eqs. (6.2) and (6.6), we find that a near-resonance structure of this type can replace a portion of free space of length

$$L = \frac{2\alpha k_0}{\gamma_0}. \tag{6.7}$$

A space-squeezing effect is then obtained if the length L is greater than the actual thickness T of the nonlocal structure. Most importantly, we can determine a fundamental limit to this effect by noting again that the transmission phase, $\arg(t)$, in Eq. (6.4) is limited in the range $[-\pi/2, \pi/2]$ due to its single-resonance nature. If we then set the constant term in Eq. (6.6) to $(\omega - \omega_r)/\gamma_0 = \pi/2$, which corresponds to operating slightly off-resonance, the quadratic term is bounded in the range $-\pi < -\alpha k_t^2/\gamma_0 < 0$, provided that all higher-order terms are zero. Hence, if k_t^2 is outside the range $[0, \pi\gamma_0/\alpha]$, there must be higher-order terms in Eq. (6.6) to guarantee that the left-hand-side remains limited in the range $[-\pi/2, \pi/2]$; therefore, in this case, $\arg(t)$ can no longer be considered quadratic with respect to k_t. Thus, the maximum allowed value, $k_{t,\max}$, for which the phase function can be assumed quadratic within the range $k_t \in [0, k_{t,\max}]$ is given by $k_{t,\max}^2 = \pi\gamma_0/\alpha$. Finally, using Eq. (6.7), we obtain a quantitative trade-off between the replaced length L/λ_0 and the maximum operating range of transverse momentum $k_{t,\max}/k_0 = \sin\theta_{\max}$ (maximum angular range):

$$\frac{L}{\lambda_0} \cdot \left(\frac{k_{t,\max}}{k_0}\right)^2 \leq 1. \tag{6.8}$$

which indicates that a larger L can only be obtained at the expense of a smaller angular range. The trade-off is written as an inequality since the assumptions leading to it may not be satisfied by a generic guided-mode resonance. In addition, it can be verified from the above derivation that different choices for the

constant term in Eq. (6.6) (different from $(\omega - \omega_r)/\gamma_0 = \pi/2$), which corresponds to operating at slightly different frequencies, always lead to a narrower angular range.

Although the structure considered here is different from the photonic-crystal slab in [158], the trade-off still holds, because both structures rely on essentially the same mechanism, namely, a single guided-mode resonance with an approximately quadratic dispersion relation. This trade-off explains why, in the designs proposed in Ref. [158], the squeezing ratio R is very high, whereas the angular range is very limited. We also note that the results in Ref. [158] are far from the limit defined by Eq. (6.8) because, while this design similarly uses a single-mode resonance, the resonance corresponds to a minimum of transmission, instead of a maximum, and therefore the structure needs to be operated at a frequency far from this minimum, where the available transmission-phase variation (as a function of wavenumber) is much more limited than around resonance. This leads to a poor utilization (only a few percents) of the total available phase range provided by the resonance. Moreover, while the nonlocal metamaterial in Ref. [157] is based on optimization and not enough information is available about its guided-mode distribution, the published results suggest it also follows a qualitatively similar trade-off. In light of the theoretical results of this section, we argue that more sophisticated nonlocal space-squeezing structures, perhaps based on optimization or inverse design, would not offer any major advantage compared to the very simple structure in Fig. 6.1(b) if they are still based on a single resonance, as they would still be constrained by the same performance trade-off.

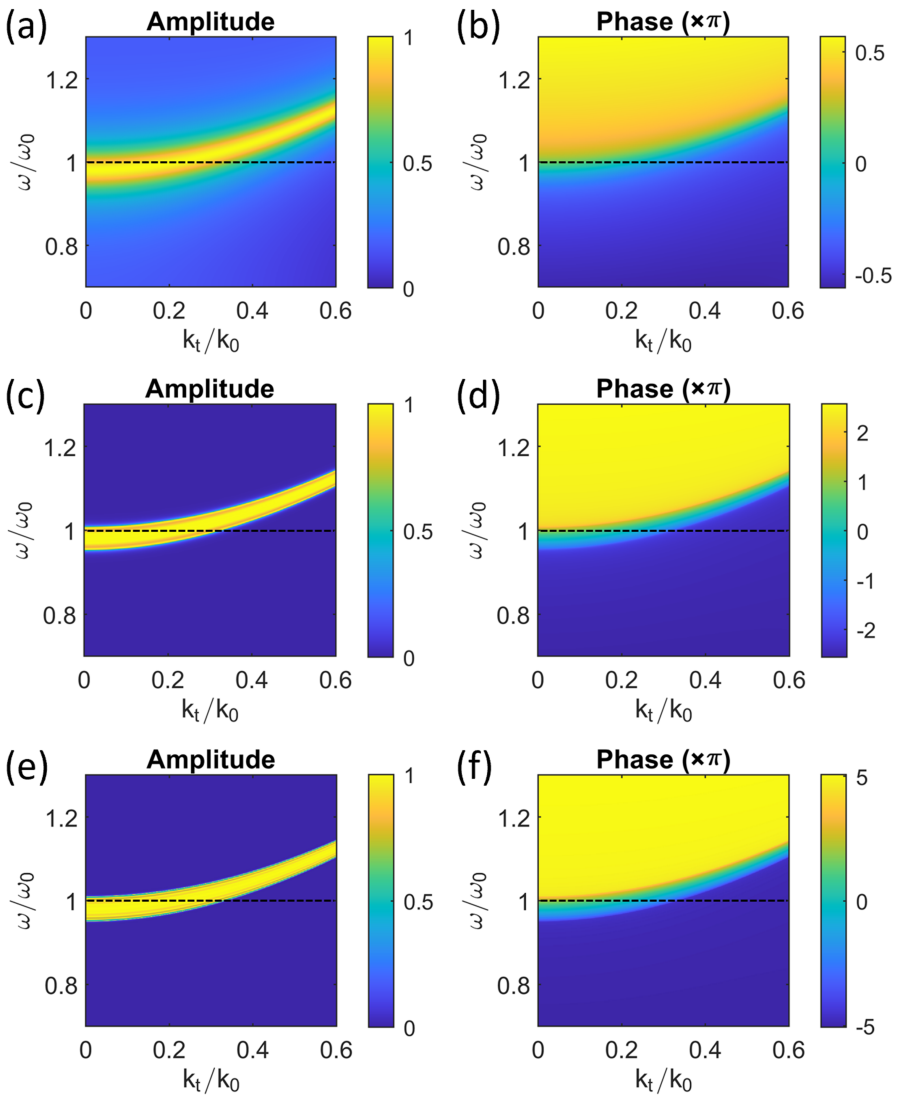

Figure 6.2: Density plots of the transmission amplitude (left column) and phase (right column) for the proposed n-layer structure acting as a nonlocal metasurface (details in the text), for TE polarization, as a function of frequency ω and transverse momentum k_t. (a) and (b) $n = 1$; (c) and (d) $n = 5$; (e) and (f) $n = 10$. Since the guided modes responsible for this resonance are well-confined and with low radiation loss (the eigenfrequency has small imaginary part), the bright band in the transmission amplitude plots is a good approximation of the modal dispersion relation. The horizontal dashed lines indicate the operational frequency ω_0, which is chosen to be slightly off-resonance at normal incidence, i.e., $\omega_0 = 1.02\omega_r$, in order to utilize the widest possible angular range over which the transmission phase is a quadratic function of k_t.

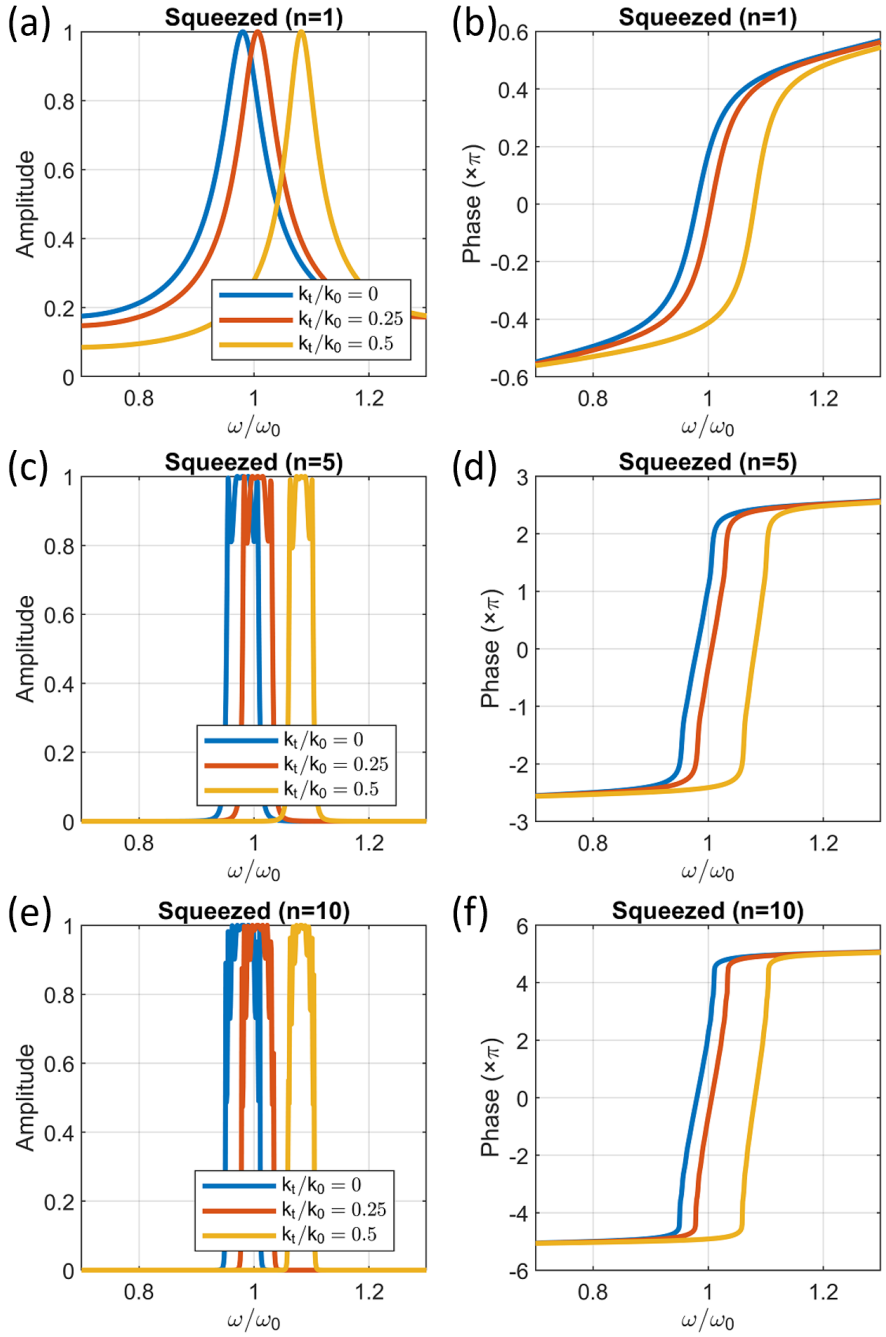

Figure 6.3: Transmission amplitude (left column) and phase (right column) of the proposed n-layer structure acting as a nonlocal metasurface (details in the text), for TE polarization, plotted as a function of frequency ω for three different values of transverse wavenumber k_t/k_0 = 0, 0.25 and 0.5.

6.2.2 Nonlocal structures inspired by coupled-resonator-based band-pass filters

Despite being an approximate and loose bound (due to the assumptions discussed above), the trade-off in Eq. (6.8) is already quite stringent: as an example, a space-compression effect with $L = 5\lambda_0$ could be achieved only over a ±25 degrees angular range, even in the best possible scenario. In order to attain significantly better performance, which would make nonlocal flat-optics systems of this type more appealing in practical scenarios, we seek to relax this trade-off between the length of replaced free space and the operating range of transverse momentum. To this aim, we need an arbitrarily large transmission phase range (not limited to π) that is linear with ω or $\omega(k_t)$ and, therefore, quadratic with respect to k_t over a much broader range $[0, k_{t,\max}]$ (indeed, $k_{t,\max}$ depends on the available phase range as discussed above). Hence, the single-resonance transmission response in Eqs. (6.3), (6.4) is clearly inadequate.

A seemingly simple solution to break the trade-off is to stack n resonant structures of the type in Fig. 6.1(b), exploiting the larger total phase range of a n-resonator system. Indeed, Ref. [158] suggests considering nonlocal space-squeezing metasurfaces in cascade. However, it is crucial to note that a generic coupling between resonators would typically hinder the performance of the nonlocal structure because, while the total transmission-phase range of n coupled resonators is $n\pi$, the phase function would generally not remain linear with frequency as a result of coupling-induced resonant-frequency splitting [160] (for example, for the case of two resonators of the type in Fig. 6.1(b) cascaded back-to-back with no separation, it is easy to verify that the resonant frequency of the individual resonators does no longer correspond to a transmission maxi-

mum of the two-resonator system, and the phase is no longer linear around this frequency). Hence, arranging n space-squeezing devices in cascade may be used to increase the length of replaced free space, but usually at the expense of further decreasing the operating angular range, since a strongly non-linear transmission-phase response with respect to frequency would result in a strongly non-quadratic phase response with respect to k_t, except perhaps in a very small range. In other words, Eq. (6.6) would be valid only over a very small range of k_t since the linear approximation in Eq. (6.4) would be valid only over a very small range of frequencies.

To overcome this problem, we took inspiration from conventional microwave band-pass filters, which are typically designed by suitably coupling multiple resonators in cascade [161, 162, 39]. In particular, if several resonators (the structures in Fig. 6.1(b)) are separated by quarter-wavelength spacers, as illustrated in Fig. 6.1(c), the resulting coupling produces new resonance peaks that are suitably distributed over a certain frequency window, providing a relatively uniform in-band transmission amplitude. To elaborate on this point, the rationale for using quarter-wavelength spacers comes directly from linear circuit theory and transmission-line/waveguide theory. At low frequencies, where lumped-element circuit theory is a valid approximation, a band-pass maximally-flat filter can be realized by using resonant branches (lumped LC resonators) connected alternately in series and in parallel [39]. A configuration more suitable for high-frequency systems (e.g., microwave waveguides) is obtained by stacking parallel resonant cavities spaced a quarter wavelength apart. This design strategy makes use of the impedance-inverting property of a quarter-wave segment, which converts series-connected elements into parallel-connected elements, thereby avoiding the necessity of using both series and

parallel branches [161, 162, 39] (series elements are more difficult to implement at high frequencies). This design can then be directly translated for optical frequency operation, in the form of resonant layers separated by quarter-wavelength spacers, as in Fig. 6.1(c), to obtain the desired uniform transmission window. An approximately uniform transmission amplitude then translates into an approximately linear transmission phase within the pass-band (especially toward the center), consistent with Kramers-Kronig-like relations between amplitude and phase of the transmission coefficient of causal passive linear systems [163]. With this strategy, therefore, one can obtain a transmission phase that covers a range of $n\pi$ and varies linearly around the resonant frequency ω_r of the individual resonators. From a simple analysis, it can be shown that the transmission phase of the multilayered structure around resonance ($\omega \approx \omega(k_t)$) can be approximated as

$$\arg(t) \approx n \cdot \frac{\omega - \omega(k_t)}{\gamma_0}. \tag{6.9}$$

In addition, while the coupling between resonators generates different resonance peaks covering a certain pass-band, as discussed above, the original transmission peak is still present since, exactly at resonance, each resonator looks transparent to the other resonators, and this resonance peak evolves with k_t as in the single-resonator case, following the same dispersion relation (this can be seen in the examples in Figs. 6.2 and 6.3 discussed in the following). Thus, the transmission phase of the n-layer structure can be approximated as,

$$\arg(t) \approx n \cdot \frac{\omega - \omega_r}{\gamma_0} - n \cdot \frac{\alpha}{\gamma_0} k_t^2, \tag{6.10}$$

and, by comparing again the quadratic terms in Eqs. (6.2) and (6.10), we find that the length of replaced free space by this n-layer nonlocal structure is

$$L = n \cdot \frac{2\alpha k_0}{\gamma_0}. \tag{6.11}$$

Finally, following the same reasoning as before, the trade-off limit in Eq. (6.8) becomes

$$\frac{L}{\lambda_0} \cdot \left(\frac{k_{t,\max}}{k_0} \right)^2 \leq n, \tag{6.12}$$

which shows that, as we increase the number n of suitably coupled elements, the product of replaced length and angular range can become arbitrarily large.

To demonstrate the potential and simplicity of this strategy to implement the optical response of free space over a much smaller length, and a wide angular range, we designed a multilayered structure acting as a nonlocal metasurface using simple dielectric plates with relative permittivity $\varepsilon_1 = 15$, separated by layers with relative permittivity equal to unity, as in Fig. 6.1(c). We stress that this high value for the permittivity ε_1 is not a requirement for the operation of the space-compression device and is considered here just as an example; materials with lower refractive index would also work, with some advantages and disadvantages. Indeed, a moderately high contrast between the dielectric layers contributes to a relatively high Q factor and a small linewidth γ_0 for the Fabry-Pérot-like resonance, which determines an increase in the replaced length according to Eq. (6.11), but a decrease in the operating angular range due to the trade-off in Eq. (6.8).

The calculated transmission coefficient around the first even Fabry-Pérot-like resonances of this n-layer nonlocal structure is plotted, for different numbers of layers/resonators, as a function of both transverse momentum k_t and frequency ω in Fig. 6.2, and as a function of ω for different values of k_t in Fig. 6.3. We first consider transverse-electric (TE) polarization as an example, while transverse-magnetic (TM) can be similarly analyzed and will be discussed in the following. From these plots, we see that the total phase range of the n-

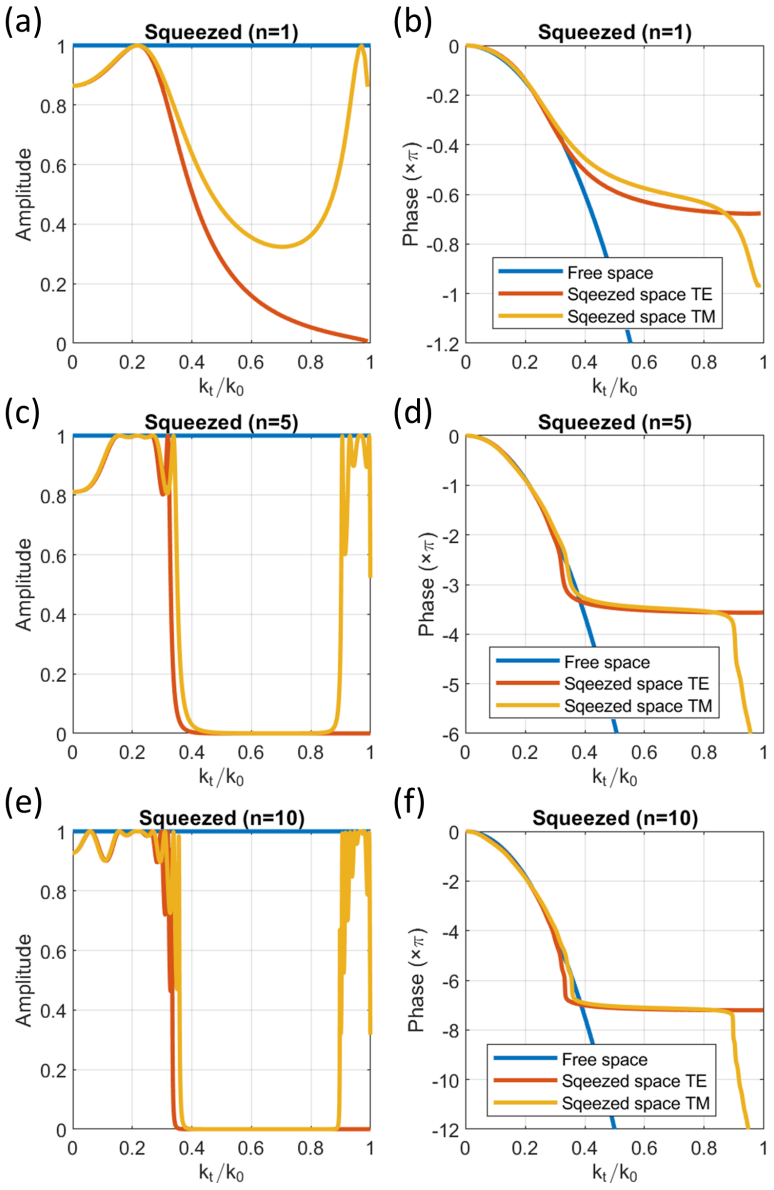

Figure 6.4: Transmission amplitude (left column) and phase (right column) of the proposed n-layer structure acting as a nonlocal metasurface, for both TE and TM polarizations, compared with the transmission response of the replaced free-space volume of length: $3.6\lambda_0$ (first row), $21.8\lambda_0$ (second row) and $44.9\lambda_0$ (third row). The transmission coefficient is plotted as a function of transverse wavenumber k_t, at a fixed near-resonance frequency $\omega_0 = 1.02\omega_r$. All transmission phases are adjusted to start from 0 at $k_t = 0$ since a global phase difference with respect to free space is irrelevant.

layer structure is $n\pi$, as expected. Importantly, near resonance the transmission phase as a function of frequency can be well approximated by a linear function, whose slope linearly increases with n, as seen in Fig. 6.3. The transmission amplitude becomes sharper and more "box-like" as n increases, characterized by a frequency window within which the amplitude is large and increasingly uniform, corresponding to the frequency range where the phase is approximately linear. This behavior for the transmission amplitude and phase of the proposed n-layer nonlocal structure near resonance is indeed analogous to that of standard band-pass filters [161, 39, 162]. We also observe that the dispersion relation of the guided modes of the n-layer structure (corresponding to the bright band in Figs. 6.2(a,c,d)) has an approximate quadratic shape with respect to k_t, consistent with Eq. (6.5). Note that this dispersion relation remains essentially identical as the number of layers n increases since, as mentioned above, exactly at resonance each resonator looks transparent to the other resonators (its input impedance is identical to the wave impedance of the host medium) and, therefore, the original transmission peak evolves with k_t as in the single-resonator case.

Since the transmission phase is quadratic with k_t at frequencies both slightly above and below resonance (where the phase is linear with respect to frequency before saturating), we operate slightly off-resonance, setting the operating frequency to $\omega_0 = 1.02\omega_r$, so that we can utilize a wider range of k_t over which the phase is quadratic, consistent with our discussion around Eq. (6.8) (this can also be understood by tracking the phase along the horizontal dashed lines in Fig. 6.2). The downside of this choice is that the transmission amplitude is no longer unity for $k_t = 0$, as seen in Fig. 6.2; however, if we are not too far away from resonance, the amplitude remains high, especially if multiple lay-

ers are employed. This is further demonstrated in Fig. 6.4, which shows the transmission amplitude and phase of the n-layer nonlocal structure as a function of transverse momentum k_t, at the operating frequency ω_0. The analytical results are calculated using the standard transfer-matrix method. We observe that the k_t-dependent transmission phase of these nonlocal structures matches that of free space, with high accuracy, over a moderately wide angular range $-0.33 < k_t/k_0 < 0.33$. This means that, with for example $n = 10$ layers, corresponding to a thickness $T \approx 9\lambda_0$, we can replace a length of free space $L \approx 45\lambda_0$ over a reasonably large angular range. These numbers correspond to approximately 50% of the limit in Eq. (6.12), indicating good utilization of the available phase range. Furthermore, within this operating angular range, the transmission amplitude remains large, with a minimum of 0.8 for the single-resonator metasurface in Fig. 6.4(a) (this is much higher than the transmission amplitude of the nonlocal metamaterial in Ref. [157]). We also note that the transmission response does not change much with polarization within the operating range of k_t. This is because (i) the transmission coefficients for TE and TM polarizations converge at normal incidence, and (ii) for moderately small incidence angles, the TE and TM transmission peaks are almost identical since the Fabry-Pérot-like resonances only depend on the phase delay inside the resonators, which is polarization independent, and on the reflection coefficients of the dielectric plates, which in our case remain approximately real for moderately small k_t.

Most importantly, the total transmission phase range provided by the n-layer nonlocal structure keeps increasing linearly with n (see the different phase ranges in Fig. 6.4(b,d,f)), with no observable increase of relative phase error and with clear improvements in terms of transmission amplitude. Since these multilayered nonlocal structures are able to mimic the response of free space for an

arbitrary range of transmission phases, they can be used to replace free-space volumes of arbitrary length, as further demonstrated in the context of focusing and imaging in the next section.

We also note that, because the replaced length of free space increases linearly with n, but the thickness of the n-layer nonlocal structure does not, due to the extra quarter-wavelength space between resonators, the squeezing ratio R is not constant. For our one-layer nonlocal metasurface, the squeezing ratio is $R = 5.6$, while it slightly decreases to $R = 5.15$ when n is large. This compression ratio and angular range are better than the ones reported in Ref. [157] ($R = 4.9$ and $k_{t,\max}/k_0 = 0.27$), even without optimization, and with a much simpler, regular, and scalable design with higher transmission amplitude. In addition, if we target a much smaller angular range, for example $k_{t,\max}/k_0 = 0.01$, using a 40-layer structure, as in one of the designs in Ref. [158], the total length of replaced free space L/λ_0 allowed by the trade-off in Eq. (6.12) would be more than fifty times larger than what was obtained in Ref. [158], due to the fact that these earlier designs only utilize a few percents of the available phase range around a transmission resonance (compared to 50% for our structures). We stress again that our results are obtained with only dielectric materials and no optimization, which suggests that there is very large room for improvement in terms of compression ratio (for a fixed L and $k_{t,\max}$) if the resonators are miniaturized using optimization and inverse design, and perhaps by employing high-index dielectrics combined with plasmonic materials.

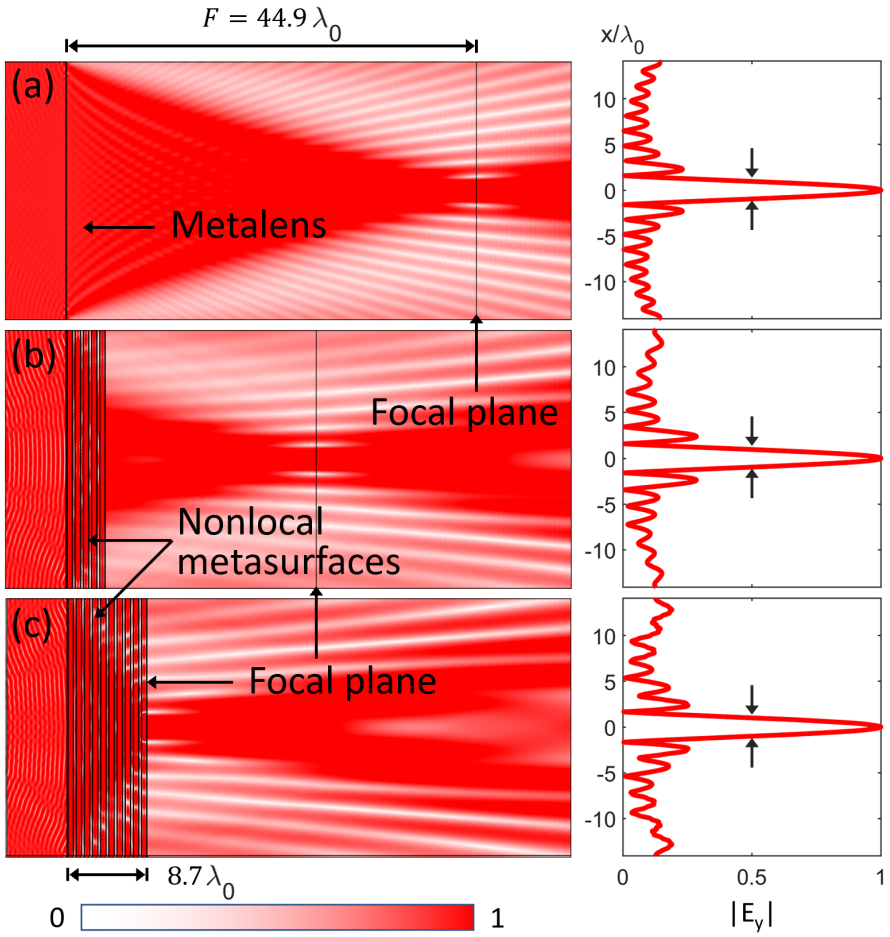

Figure 6.5: Normalized distribution of the electric field amplitude for the focusing of a TE-polarized plane wave by (a) a local idealized metalens, and (b,c) the same metalens followed by nonlocal metasurfaces with 5 layers (panel b) and 10 layers (panel c). The dielectric nonlocal structure moves the focal plane closer and closer to the metalens, with minimal distortions and without changing the focal length of the metalens (which is a property of the local metalens itself). The insets on the right show the field amplitude distribution on the focal plane. In panel (c), all space between the lens and the focal plane has been replaced and compressed by the nonlocal structure, realizing a compact solid-state flat-optics focusing system.

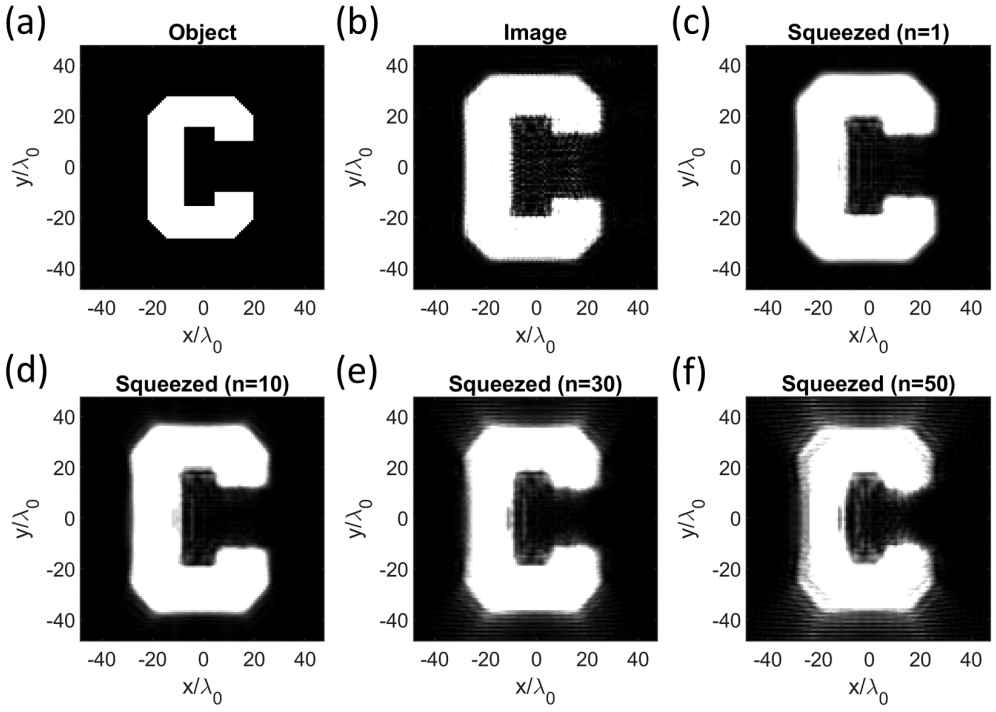

Figure 6.6: Imaging and magnification with dielectric nonlocal metasurfaces inserted between a metalens and the observation plane (as illustrated in Fig. 6.1 (a)). (a) Object to be imaged: a uniformly illuminated aperture with the shape of the letter "C" from Cornell University's logo. (b) Magnified image intensity, at the observation plane, formed by a metalens without nonlocal metasurfaces. (c)-(f) Magnified images formed by the same metalens followed by multilayered structures acting as nonlocal space-squeezing metasurfaces, as in Fig. 6.5, for different numbers of layers n. The same magnification is obtained in all panels since the focal length of the metalens remains the same, whereas the image forms at closer distances, thereby overcoming the trade-off between propagation length and magnification, as discussed in the text. The distance between lens and observation plane in panels (b) to (f) is, respectively, $230.6\lambda_0$, $226.6\lambda_0$, $193.4\lambda_0$, $119\lambda_0$ and $44.6\lambda_0$. The focal length of the metalens is $100\lambda_0$. The considered lateral size of the object, flat-optics device, and observation plane is $96\lambda_0 \times 96\lambda_0$. All of the transverse planes are discretized into 120×120 pixels, hence the size of each pixel is $0.8\lambda_0 \times 0.8\lambda_0$. In panel (f), all space between the lens and the observation plane has been replaced by the designed dielectric nonlocal device.

6.3 Nonlocal Flat-Optics for Focusing, Imaging, and Magnification

In this section, we theoretically demonstrate, for the first time, the potential of combining local metalenses and nonlocal space-squeezing metasurfaces for focusing and imaging. First, we apply these ideas to the problem of focusing a TE-polarized plane wave within a much more compact volume. The results are shown in Fig. 6.5 (obtained via full-wave numerical simulations [106]). Because local metalenses have been studied extensively in the literature and the design of a specific metalens is not the topic of this chapter, we use an idealized metasurface that implements the local transmission-phase response in Eq. (6.1) (an idealized planar thin slab with a suitable distribution of constitutive parameters); however, this may be replaced by any of the realistic metalenses demonstrated in the recent literature. We have also verified that, if the local metalens is not ideally impedance-matched to the surrounding medium, the resulting reflections and interactions between metalens and nonlocal metasurface reduce the overall transmission efficiency but, even in the presence of moderately high reflections, the functionality of the system is not affected too negatively (see supplementary information). This is mainly because the designed nonlocal structure exhibits very low reflection within its operating bandwidth and angular range (see, e.g., Fig. 6.4(e)), therefore minimizing any unwanted interaction with a mismatched metalens.

As shown in Fig. 6.5(a), when the space beyond the metalens is occupied by free space, the transmitted plane wave is focused on a focal plane at a distance equal to the focal length F of the local metalens, as for any conventional

thin lens. On the focal plane, the field profile largely follows a sinc function, as expected for this two-dimensional focusing setup, with a nearly diffraction-limited focal spot of width $1.67\lambda_0$, for a numerical aperture $NA = 0.3$. Then, we insert a 5-layer and a 10-layer structure acting as nonlocal space-compression metasurfaces as in Fig. 6.1, between the lens and the focal plane. The results shown in Fig. 6.5(b,c) clearly demonstrate that the entire field distribution behind the lens is shifted towards the lens by a distance $L-T$, and with low distortions, leading to a drastic reduction of the focal plane distance from the metalens. Particularly striking is the case with the 10-layer nonlocal device, in which light is focused on the back face of the stack of local and nonlocal structures. This means that all free space between the lens and the focal plane has been replaced and compressed, realizing a compact, planar, solid-state, focusing device. Furthermore, comparing the field distributions at the focal plane for these three cases in Fig. 6.5, we note that the width of the main lobe and the position of the first zeros are nearly identical, suggesting good focusing performance with small monochromatic aberrations. This is obtained thanks to the good angular transmission response of the nonlocal structure (see Fig. 6.4), which closely mimics the response of a free-space volume both in amplitude and phase.

Most importantly, we stress that, while focusing is obtained at a much shorter distance, as seen in Fig. 6.5(b,c), the focal length of the lens is the same (since the nonlocal structure is transversely homogeneous it cannot change the focal length of the metalens). Thus, the nonlocal device fundamentally decouples the actual distance at which focusing is achieved from the focal length of the lens, and hence its magnifying power. Indeed, this hybrid system combining local and nonlocal metasurfaces may realize magnification of an object without the need for a large propagation length. Fig. 6.6 shows an example demonstrat-

ing this exciting opportunity for imaging and magnification. The object to be imaged is an illuminated aperture with the shape of the letter "C" in Cornell University's logo. We calculated the resulting image, produced by a composite flat-optics device as in Fig. 6.5(b,c), using the well-established scalar diffraction theory [145]. We assume the electric field is uniform in the y direction on the aperture in Fig. 6.6(a) and zero outside (note that this assumption is not physical as it violates the continuity of tangential electric field, but the results under this assumption are in good agreement with experimental measurements for sufficiently large objects [145]; for separation of TE and TM polarizations, we refer to Ref. [159] (Supplemental material)). The imaging system is set up to obtain a magnified image, with a magnification factor of 1.3 (but larger values can be easily obtained by playing with the object distance and the focal length of the metalens). The image produced by the metalens alone, without nonlocal metasurfaces, is shown in Fig. 6.6(b) at a distance ($230.6\lambda_0$) dictated by the focal length of the lens and the desired magnification factor. Then, as in Fig. 6.5, we insert the designed nonlocal structure, with increasing number of layers, right after the metalens. The resulting images, shown in Fig. 6.6(c-f), form on planes that are closer and closer to the metalens. When the inserted number of layers reaches 50, all free space is replaced by the much thinner nonlocal device, and the image forms on the back face of the structure. The distance between lens and observation plane has been decreased from $230.6\lambda_0$ to $44.6\lambda_0$; however, since the focal length of the metalens is unaltered, the same magnification is obtained as in the original case.

In the results reported in Fig. 6.6, we observe larger distortions when n is large because, although the relative phase error (with respect to the maximum transmission phase for a certain n) remains approximately constant, the abso-

lute error increases with n. Then, when the absolute error is comparable with an odd-multiple of π, maximum distortion occur on the observation plane. However, the image is still clearly visible and, thanks to the high transmission amplitude of the proposed nonlocal structure, the image intensity remains high even for a cascade of 50 layers. We also note that the functionalities discussed in this section, in particular the fully solid-state focusing and imaging systems in Figs. 6.5(c) and 6.6(f), would not be realizable with earlier nonlocal designs as they either exhibit an angular range that is too narrow [158] or they are not scalable to many layers without further optimization, or drastic design changes, to obtain a high transmission amplitude [157]. Despite its simplicity, our proposed design is the first to enable a much wider operating angular range and to offer the possibility to replace, in a scalable manner, an arbitrarily long free-space volume with high transmission amplitude. Thanks to these advances, we have theoretically demonstrated, for the first time, the potential of suitably combining local and nonlocal flat optics for focusing and imaging beyond some of the trade-offs of conventional optics.

6.4 Conclusion

In summary, we have proposed a solution to realize fully solid-state ultra-thin optical systems in which all conventional lenses are replaced by flat local metalenses and all free-space volumes between lenses and detectors are replaced by the proposed dielectric structures acting as nonlocal metasurfaces. From an analysis of the response of generic single-resonance-based nonlocal metasurfaces, we have derived a quantitative trade-off between the total length of replaced free space and the operating range of transverse momentum (angu-

lar range). This trade-off explains some of the inherent limitations and constraints of previous works [157, 158]. To relax this trade-off and realize nonlocal space-compression optics with performance more suitable for practical applications, we have designed and theoretically/computationally demonstrated a nonlocal flat-optics structure composed of n resonant layers separated by quarter-wavelength spacers, inspired by coupled-resonator-based microwave band-pass filters. This design strategy guarantees high transmission amplitude and highly linear transmission phase vs. frequency, without compromising the operating range of transverse momentum, hence enabling the possibility of replacing free-space volumes of arbitrary length. With our proposed design, we have demonstrated, theoretically and computationally, that nonlocal flat optics may allow realizing planar ultra-thin structures for light focusing and imaging that overcome some of the limits and trade-offs of conventional imaging systems, with intriguing implications for photography, augmented/virtual reality, microscopy, et cetera.

The proposed nonlocal metasurfaces are based on a simple stack of homogeneous dielectric slabs, in which the high-permittivity layers could be made of silicon, separated by layers made of a transparent material with lower permittivity (for example silica). However, different materials could be considered as long as a moderately high refractive-index contrast between layers is obtained (the contrast would affect the linewidth of the resonances, and hence the replaced length of free space). We stress that since the Q factor of the resonant layers is modest (Q = 15 in the considered example), the operating bandwidth of the nonlocal device is not too narrow (fractional bandwidth of few percent) and the device is expected to be moderately robust to losses, fabrication tolerances, and resonator detuning. These properties make our design particularly

suitable for fabrication and integration between a metalens and an imaging sensor. Indeed, the fabrication of multi-layer dielectric optical coatings is a mature technology [164] that can be leveraged for the future realization of these devices. We also would like to reiterate that the proposed structures have been obtained without any optimization, and hence we are confident there is still very large room for improvement, especially in terms of miniaturization of the coupled resonators composing the nonlocal device.

Besides optical applications, our proposed nonlocal metasurfaces may also be used at RF and microwave frequencies, e.g., for antenna miniaturization, and an experimental proof-of-concept in this area is currently under way. More broadly, we strongly believe that the vast opportunities offered by combining local and nonlocal metasurfaces may have far-reaching applications in different areas of wave physics and engineering.

6.5 Appendix: approximate analytical models for nonlocal metasurfaces and the impact of impedance mismatch

6.5.1 Lumped circuit models for frequency response

To calculate the transmission response of the layered structures acting as nonlocal metasurfaces, we resort to transmission-line theory [39], which provides an exact and simple formulation of the problem since the metasurface structures are transversely invariant. Each layer of the metasurfaces (dielectric plates and space in between) is modeled as a segment of transmission-line, where the prop-

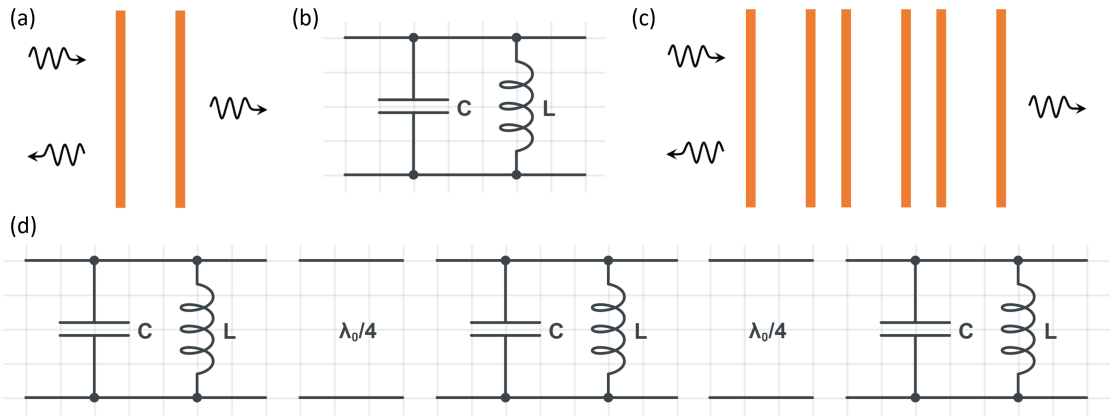

Figure 6.7: Circuit models for the considered layered structures acting as nonlocal metasurfaces. The local frequency response of the resonant element in (a) near the first even Fabry-Pérot-like resonance is modeled with a parallel LC resonator in (b). The local frequency response of n quarter-wavelength-spaced resonant elements in (c) is modeled by n LC resonators with quarter-wavelength-spaced transmission lines in between (d).

agation constant and the characteristic impedance, for transverse electric (TE) polarization, are

$$\begin{aligned} k_{z,TE} &= k\sqrt{1-\frac{k_t^2}{k^2}}, \\ Z_{TE} &= \eta/\sqrt{1-\frac{k_t^2}{k^2}}, \end{aligned} \tag{6.13}$$

and for transverse magnetic (TM) polarization, are

$$\begin{aligned} k_{z,TM} &= k\sqrt{1-\frac{k_t^2}{k^2}}, \\ Z_{TM} &= \eta\sqrt{1-\frac{k_t^2}{k^2}}, \end{aligned} \tag{6.14}$$

where k and η are the wave number and wave impedance in the corresponding homogeneous media and k_t is the transverse wave number (transverse momentum). Then the transmission response of the layered metasurfaces is calculated through transmission-line network analysis [39].

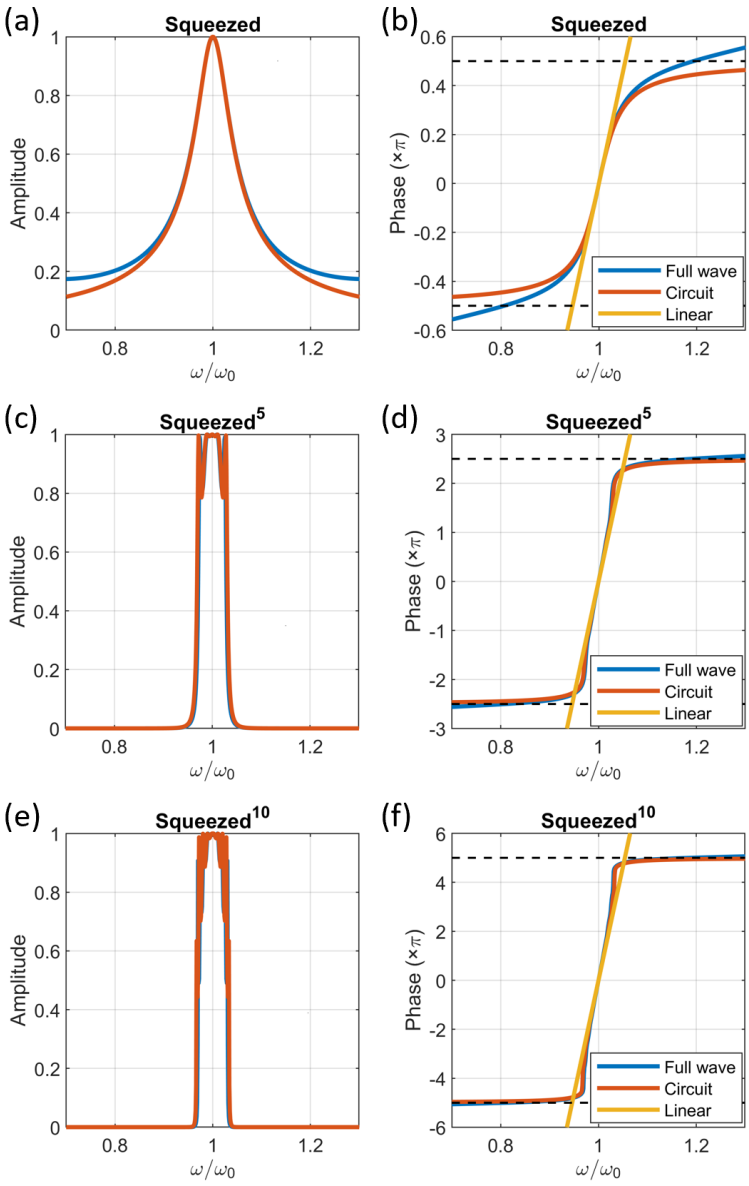

Figure 6.8: Transmission amplitude and phase of the multilayered structures composed of different numbers of resonators, obtained from the exact transmission-line model, the equivalent LC circuit model, and the linear approximation near resonance, using the parameters in the main text. The bounds of the phase range around resonance are indicated in the panels with dashed lines.

The results from full-wave transmission-line theory are exact. However, the final expressions are lengthy and opaque to intuition. To get more concise and revealing closed-form expressions for the transmission response of these nonlocal structures, we use approximate analytical models for the resonant elements. Specifically, near the frequency of the first even Fabry-Pérot-like resonance, we model the resonant elements of the nonlocal structures in Fig. 6.7 as parallel LC resonant circuits, and the quarter-wavelength spacers as quarter-wavelength transmission lines, as shown in Fig. 6.7. These spacers provide a $\pi/2$ phase shift, and we have assumed that this $\pi/2$ phase shift is approximately frequency-independent in a narrow band around resonance. The values of the LC elements can be obtained by comparing the resonant frequency and the Taylor expansion coefficients of the frequency-domain transmission (or reflection) coefficient of the actual resonant structure and of the circuit model (see Supplementary material of [16]). With this approach, we obtain

$$\begin{aligned} L &= \frac{2\varepsilon_1\eta_0}{\pi\omega_r\left(\varepsilon_1-1\right)\left(1+\sqrt{\varepsilon_1}+\varepsilon_1\right)}, \\ C &= \frac{\pi\left(\varepsilon_1-1\right)\left(1+\sqrt{\varepsilon_1}+\varepsilon_1\right)}{2\varepsilon_1\eta_0\omega_r}. \end{aligned} \tag{6.15}$$

The transmission coefficient of the parallel LC resonator is

$$t = \frac{-2i\omega L}{-2i\omega L+\eta_0-LC\eta_0\omega^2}. \tag{6.16}$$

Then, considering $\omega \approx \omega_r$, we can write the transmission coefficient as

$$t \approx \frac{\gamma_0}{\gamma_0 - i\left(\omega-\omega_r\right)}, \tag{6.17}$$

where

$$\omega_r = \frac{1}{\sqrt{LC}}, \tag{6.18}$$

and (assuming γ_0 is invariant with frequency)

$$\gamma_0 = \frac{\omega_r^2 L}{\eta_0} = \frac{1}{C\eta_0} = \frac{\omega_r}{2Q} = \frac{2\varepsilon_1\omega_r}{\pi\left(\varepsilon_1-1\right)\left(1+\sqrt{\varepsilon_1}+\varepsilon_1\right)}, \tag{6.19}$$

where Q is the quality factor of the resonator. Thus, the transmission phase of a single LC resonator is

$$\arg(t) = \arctan\left(\frac{\omega - \omega_r}{\gamma_0}\right) = \frac{\omega - \omega_r}{\gamma_0} + O\left[\frac{\omega - \omega_r}{\gamma_0}\right]^3. \tag{6.20}$$

For a chain of n quarter-wavelength-spaced resonators, the resonators can be assumed to be approximately decoupled if $\omega \approx \omega_r$ since, at resonance, each resonator looks transparent to the others (its input impedance is identical to the free-space wave impedance). Hence, the transmission coefficient, assuming $\omega \approx \omega_r$, is

$$t = \frac{2y(\gamma_0\omega_r)^n}{(iy - \gamma_0\omega_r)\left[\omega_r(\omega_r - \omega) - y\right]^n + (iy + \gamma_0\omega_r)\left[\omega_r(\omega_r - \omega) + y\right]^n}, \tag{6.21}$$

where

$$y = \omega_r\sqrt{(\omega - \omega_r)^2 - \gamma_0^2}. \tag{6.22}$$

This expression is still cumbersome, so we expand it in Taylor series to obtain

$$t = (i)^{n-1}\left[1 + in\left(\frac{\omega - \omega_r}{\gamma_0}\right) + O(\omega - \omega_r)^2\right], \tag{6.23}$$

where $(i)^{n-1}$ accounts for the $\pi/2$ phase contributions of the quarter-wavelength spacers, while the rest of the expression represents the response of the n cascaded resonators, which contribute to a total phase variation of $n\pi$. We ignore the phase factor introduced by the quarter-wavelength transmission lines, which, under our approximations, is a global phase independent of frequency (in reality, this phase depends on frequency, but more weakly than the resonant contribution). Then, the transmission phase of the n-resonator structure is approximately given by

$$\arg(t) \approx \arctan\left(n \cdot \frac{\omega - \omega_r}{\gamma_0}\right) = n \cdot \frac{\omega - \omega_r}{\gamma_0} + O\left[n \cdot \frac{\omega - \omega_r}{\gamma_0}\right]^3. \tag{6.24}$$

We note that, near resonance, the slope of the linear coefficient is proportional to n. In Fig. 6.8, we plot the transmission amplitude and phase of the multilayered structures composed of different numbers of resonators, obtained from the exact transmission-line model, the equivalent circuit model, and the linear approximation near resonance, using the parameters in the main text. We clearly see that the transmission coefficients from full-wave calculations, lumped circuit model, and linear approximation match very well near resonance. In addition, we observe that the total phase variation of n Fabry-Pérot-like resonances is indeed bounded by $n\pi$.

We also would like to stress that the linearity of the transmission phase near resonance improves with the number of layers because the transmission amplitude becomes more and more uniform within a certain pass-band, consistent with the implications of Kramers-Kronig-like relations between amplitude and phase of the transmission coefficient of causal passive linear systems, as mentioned in the main text.

The circuit models and expressions above have been derived under the assumption of normal incidence, i.e., when the transverse momentum $k_t = 0$. However, for oblique incidence, the profile of the transmission spectrum remains nearly unchanged near resonance, except for a change of resonance frequency with k_t, namely, $\omega(k_t)$ (with $\omega(k_t = 0) = \omega_r$), which corresponds to the dispersion relation of the guided mode responsible for the transmission resonances (the guided mode is assumed well confined, so that its eigenfrequency is almost real and is approximately equal to the resonance frequency).

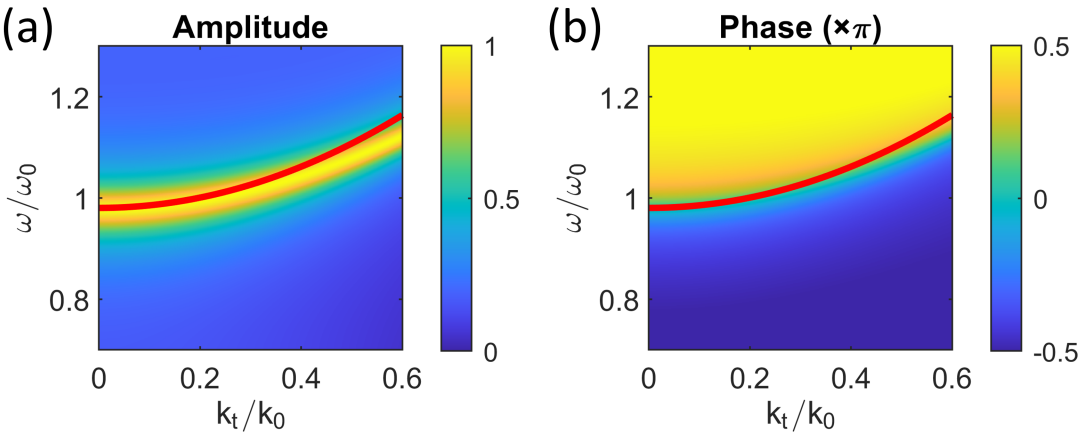

Figure 6.9: Transmission amplitude and phase for a one-layer nonlocal metasurface as a function of transverse momentum k_t and frequency ω, compared with the approximate dispersion relation (red lines) given by Eq. (6.26).

6.5.2 Approximate expressions for the dispersion relation and the length of replaced free space

At normal incidence, $k_t = 0$, the input impedance of the quarter-wavelength-thick dielectric plates is real, because of the quarter-wavelength impedance-transformation effect [39], and thus their partial reflection coefficients are also real. At oblique incidence, this is not strictly true, however we can still use this fact to make some useful approximations. Specifically, because the resonant frequency $\omega(k_t)$ does not change significantly with k_t when k_t is small, and the permittivity of the dielectric plates is much larger than that of free space, we assume that the field profiles within the dielectric elements do not change with k_t, and their partial reflection coefficient remain approximately real. Thus, the resonant frequency is solely determined by the length of space between two dielectric plates, and the dispersion relation can be calculated based on the optical

path length between them to have constructive interference

$$\sqrt{\omega^2(k_t)\mu_0\varepsilon_0 - k_t^2} \cdot \frac{\lambda_r}{2} = \pi. \tag{6.25}$$

Hence, we obtain

$$\omega(k_t) = c\sqrt{\omega_r^2/c^2 + k_t^2} = \omega_r + \alpha k_t^2 + O[k_t^4], \tag{6.26}$$

where

$$\alpha = \frac{c^2}{2\omega_r}. \tag{6.27}$$

Although this approximation is rough, the result is reasonable, as shown in Fig. 6.9, with just a slight overestimation of the quadratic coefficient α. As discussed in the main text, this dispersion relation remains essentially identical as the number of layers n increases since, as mentioned above, exactly at resonance each resonator looks transparent to the other resonators, and, therefore, the original transmission peak evolves with k_t as in the single-resonator case.

Finally, with the approximate expression of α above, we can write the full expression for the length of free space replaced by a n-layer nonlocal metasurface device

$$L = n \cdot \frac{2\alpha k_0}{\gamma_0} \approx n \cdot \frac{c}{\gamma_0} = n \cdot \frac{\lambda_r(\varepsilon_1 - 1)\left(1 + \sqrt{\varepsilon_1} + \varepsilon_1\right)}{4\varepsilon_1}, \tag{6.28}$$

where k_0 is the free space wave number at the operating frequency ω_0. With this formula, the calculated length of replaced free space is slightly overestimated, because of the aforementioned overestimation of α. However, this formula provides a good approximation, as well as qualitative intuition for the design of our nonlocal metasurface devices.

6.5.3 Impedance mismatch and reflections

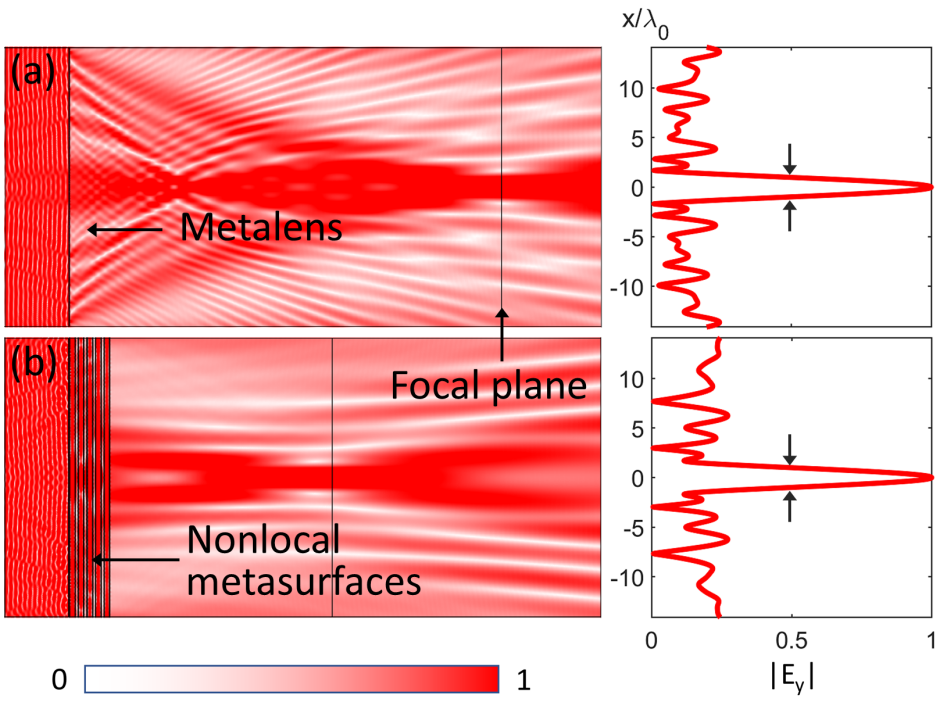

Figure 6.10: Normalized distribution of the electric field amplitude for the focusing of a TE-polarized plane wave by (a) a largely impedance-mismatched metalens with wave impedance $5\eta_0$, and (b) the same metalens followed by a nonlocal metasurface structure with 5 layers. By comparing this figure with Fig. 5(a,b) of the main text, we see that moderately high impedance mismatch and reflections reduce the overall transmission efficiency but the functionality of the system (in this case, focusing) is not affected too negatively.

CHAPTER 7

CONCLUSION AND OUTLOOK

In this dissertation, we studied meta-electromagnetics, the sub-field of electromagnetics focused on metamaterials or metamaterials-inspired designs, for scattering engineering and wavefront manipulation. As discussed in the Introduction, these concepts are intimately related through the optical theorem of scattering theory. We started with a brief review of the topic of invisibility cloaking, which was among the first applications of metamaterials. We compared transformation-based cloaking and scattering-cancellation cloaking, which are the most popular approaches to realize scattering suppression and invisibility. We stressed that for scattering-cancellation cloaking, the scatterer is still polarized, while the total scattering is suppressed. This property enables the design of "cloaked sensors" [51], preserving the ability to sense the local field profile under study while minimizing the scattering-induced perturbation. In this dissertation, we proposed a solution for cloaking a NSOM tip, minimizing its scattering cross section by carving properly engineered slits on the aluminum shell of an aperture-type probe, so that the probe tip is able to capture the near-field information under study with minimized artifacts [43]. Experimental work by our collaborators has shown the effectiveness of our design idea.

We then tackled the fundamental problem of the narrow bandwidth of linear passive cloaks for scattering suppression, which stems from physical bounds related to the Bode-Fano limit of broadband impedance matching [16]. We also theoretically demonstrated that, even if the cloak is nonreciprocal, Bode-Fano limits are still valid. To find possible approaches to achieve broadband invisibility, we have to break at least one of the assumptions of the Bode-Fano limit

(linearity, passivity, and causality), among which breaking passivity is the most promising. We extensively studied the broadband scattering-cancellation properties of active cloaks and the associated stability issues. We concluded that active cloaking can indeed broaden the operating bandwidth over which scattering is reduced to a specified level, with the potential of breaking Bode-Fano limits. However, stability, namely, the absence of unbounded oscillations, imposes another limit on the bandwidth. Thus, even if we break passivity, it is still fundamentally difficult to design broadband active scattering-cancellation cloaks [36]. This work is part of an ongoing debate in the literature, triggered by a recent paper [109], on whether active cloaking based on fast-light propagation can be made ultra-broadband. We argue that superluminal group and phase velocity do not enable arbitrarily broadband invisibility, and that the active cloaking designs in [109] are either not causal or not stable [110].

We then applied Bode-Fano limits to the problem of broadband reflection reduction in lossy thin-films and, specifically, to ultra-thin solar cells to determine their maximum solar power absorption. Solar panels tend to be designed thinner and thinner to decrease materials usage and thus the cost per area. In the ultra-thin regime, when the thickness of the absorption region reaches a few tens of nm, antireflection coatings are usually employed to enhance solar power absorption instead of more complicated light-trapping strategies. We studied the maximum solar power absorption limit, over the entire solar spectrum, for ultrathin solar cells made of different materials with arbitrary antireflection coatings. To this aim, we modeled the light reflection and absorption problem with equivalent lumped circuits, and then used Bode-Fano limits to find the maximum solar power absorption. Two main results have been obtained: (i) For solar cells made of a specific material, the maximum solar power

absorption increases as the thickness of the solar panel increases. However, when the thickness reaches a certain threshold, the maximum absorbed power starts to decrease. This threshold is the optimal thickness for ultrathin solar cells made of a given material, and it corresponds to optimal tuning with respect to the given material response (the maximum absorbed power is then expected to grow again for much larger thicknesses as more modes/resonances become accessible in the slab). (ii) In the ultrathin single-mode regime, solar panels made of different materials reach their respective maximum absorption peak for different thicknesses, for example, silicon at a thickness of 48 nm, and GaAs at a thickness of 26 nm. Thus, when the thickness of the lossy layer is extremely small, GaAs performs better, whereas silicon exhibits one of the worst performance in terms of absorption, as shown in Chapter 4, as expected due to its indirect bandgap and lower losses within the solar spectrum [165].

In the second part of the dissertation, we focused on wavefront manipulations based on engineered metasurfaces for analog optical computing and miniaturization of complex optical systems. Analog optical computing units are expected to serve as hardware accelerators for existing digital electronic computers to alleviate their emerging problems in terms of heat generation and bandwidth limits for specific applications. Within this context, we proposed a compact analog optical computing platform based on the framework of metamaterial-waveguide networks. A metamaterial-waveguide network contains optical waveguides, graded-index (GRIN) lenses, metasurfaces and other compatible elements, enabling beam splitting, merging, Fourier transforms, filtering, feedback etc., with compact structures. Based on this platform, we computationally demonstrated representative design examples to perform fractional calculus of an arbitrary order, to calculate a weighted sum of

proportional-integral-derivative (PID) operations on an input function, and to solve fractional calculus equations. The proposed designs have a very small footprint of only a few wavelengths, which is promising for their potential integration with existing micro-electronic systems. This work may pave the way toward new metamaterials-inspired designs for analog optical computing and hardware acceleration.

Finally, we studied nonlocal metasurfaces for space compression and optics miniaturization. Most optical systems involve a combination of lenses separated by free-space regions where light acquires the required angle-dependent phase delay for a certain functionality. We first derived a fundamental trade-off between the length of compressed free space and the operating angular range, which explained some of the limitations of earlier designs, and we then proposed a solution to break this trade-off using nonlocal metasurface structures composed of suitably coupled resonant layers. This strategy, inspired by coupled-resonator-based pass-band filters, allows replacing free-space volumes of arbitrary length over wide angular ranges, and with high transmittance. Finally, we theoretically demonstrated, for the first time, the potential of combining local and nonlocal metasurfaces to realize compact, fully solid-state, planar structures for focusing, imaging, and magnification, in which the focal length of the lens (and hence its magnifying power) does not dictate the actual distance at which focusing is achieved. Our findings are expected to extend the reach of the field of metasurfaces and open new unexplored opportunities [166].

We predict two promising directions for future research in the area of meta-electromagnetics in general, and scattering engineering and wavefront manipulation in particular. On the one hand, academic researchers will keep extending

the complexity of constitutive relations of engineered materials, to incorporate novel properties and explore new exotic phenomena of wave propagation. One example is the emerging field of space-time metamaterials [9, 10, 167, 168]. With the new degrees of freedom offered by temporal or spatio-temporal modulations, some of the constraints and limitations of scattering engineering could in principle be relaxed, realizing for example nonreciprocal metasurfaces, or scattering engineering in the spectral domain [168], or ultra-broadband devices for impedance matching and absorption. On the other hand, many of the recent research advances in the field of meta-electromagnetics are still in the stage of purely theoretical research or experimental proof-of-concept. Thus, another promising direction is represented by efforts to turn these research achievements into devices and industrial products. These efforts are currently ongoing, especially for metasurfaces and metalenses (e.g., Lumotive [169], Metalenz [170] and Oblate Optics [171]) and analog optical computing for hardware acceleration (e.g., Lightmatter [172]), and we expect more commercialization efforts are on the horizon. To conclude, we believe the future of this broad area of research is bright, both for its basic scientific interest and for its technological implications.

BIBLIOGRAPHY

[1] Andrew Zangwill. *Modern electrodynamics*. Cambridge University Press, 2013.

[2] Alexandre Silva, Francesco Monticone, Giuseppe Castaldi, Vincenzo Galdi, Andrea Alù, and Nader Engheta. Performing Mathematical Operations with Metamaterials. *Science*, 343(6167):160–163, 2014.

[3] N Engheta. Meta-electromagnetics and meta-optics. In *2013 International Symposium on Electromagnetic Theory*, pages 1–2, 2013.

[4] John David Jackson. *Classical electrodynamics*. Wiley, New York, USA, 1999.

[5] Robert W Boyd and Barry R Masters. *Nonlinear optics, third edition.* Academic, New York, USA, 2008.

[6] Roger F Harrington. *Time-harmonic electromagnetic fields*. McGraw-Hill, 1961.

[7] L. D. Landau, E. M. Lifshitz, and L. P. Pitaevskii. Electrodynamics of continuous media, 1984.

[8] Ismo V Lindell, AH Sihvola, AJ Viitanen, and SA Tretyakov. *Electromagnetic waves in chiral and bi-isotropic media*. Artech House on Demand, 1994.

[9] C Caloz and Z Deck-Léger. Spacetime Metamaterials—Part I: General Concepts. *IEEE Transactions on Antennas and Propagation*, 68(3):1569–1582, 2020.

[10] C. Caloz and Z. Deck-Léger. Spacetime metamaterials—part ii: Theory and applications. *IEEE Transactions on Antennas and Propagation*, 68(3):1583–1598, 2020.

[11] Nader Engheta and Richard W Ziolkowski. *Electromagnetic Metamaterials: Physics and Engineering Explorations*. Wiley-IEEE Press, New York, USA, 2006.

[12] J. B. Pendry. Negative refraction makes a perfect lens. *Physical Review Letters*, 85(18):3966–3969, 2000.

[13] Zhaowei Liu, Hyesog Lee, Yi Xiong, Cheng Sun, and Xiang Zhang. Far-Field Optical Hyperlens Magnifying Sub-Diffraction-Limited Objects. *Science*, 315(5819):1686, 2007.

[14] J B Pendry, D Schurig, and D R Smith. Controlling Electromagnetic Fields. *Science*, 312(5781):1780–1782, 2006.

[15] Andrea Alù and Nader Engheta. Achieving transparency with plasmonic and metamaterial coatings. *Phys. Rev. E*, 72(1):16623, jul 2005.

[16] Francesco Monticone and Andrea Alù. Invisibility exposed: physical bounds on passive cloaking. *Optica*, 3(7):718–724, jul 2016.

[17] Mário G. Silveirinha. Trapping light in open plasmonic nanostructures. *Phys. Rev. A*, 89:023813, Feb 2014.

[18] Francesco Monticone and Andrea Alù. Embedded Photonic Eigenvalues in 3D Nanostructures. *Phys. Rev. Lett.*, 112(21):213903, may 2014.

[19] Chia Wei Hsu, Bo Zhen, A Douglas Stone, John D Joannopoulos, and Marin Soljačić. Bound states in the continuum. *Nature Reviews Materials*, 1(9):16048, 2016.

[20] W D Heiss. The physics of exceptional points. *Journal of Physics A: Mathematical and Theoretical*, 45(44):444016, oct 2012.

[21] Wei Ting Chen, Alexander Y. Zhu, and Federico Capasso. Flat optics with dispersion-engineered metasurfaces. *Nature Reviews Materials*, 2020.

[22] Ming Lun Tseng, Hui-Hsin Hsiao, Cheng Hung Chu, Mu Ku Chen, Greg Sun, Ai-Qun Liu, and Din Ping Tsai. Metalenses: Advances and Applications. *Advanced Optical Materials*, 6(18):1800554, sep 2018.

[23] Federico Presutti and Francesco Monticone. Focusing on bandwidth: achromatic metalens limits. *Optica*, 7(6):624–631, 2020.

[24] Akira Ishimaru. *Electromagnetic wave propagation, radiation, and scattering: from fundamentals to applications*. Wiley – IEEE Press, Piscataway, NJ, USA, 2nd ed edition, 2017.

[25] S A Hassani Gangaraj, M G Silveirinha, and G W Hanson. Berry Phase, Berry Connection, and Chern Number for a Continuum Bianisotropic Ma-

terial From a Classical Electromagnetics Perspective. *IEEE Journal on Multiscale and Multiphysics Computational Techniques*, 2:3–17, 2017.

[26] Ling Lu, John D Joannopoulos, and Marin Soljačić. Topological photonics. *Nature Photonics*, 8(11):821–829, 2014.

[27] Tomoki Ozawa, Hannah M Price, Alberto Amo, Nathan Goldman, Mohammad Hafezi, Ling Lu, Mikael C Rechtsman, David Schuster, Jonathan Simon, Oded Zilberberg, and Iacopo Carusotto. Topological photonics. *Rev. Mod. Phys.*, 91(1):15006, mar 2019.

[28] Frank W J Olver, Daniel W Lozier, Ronald F Boisvert, and Charles W Clark. *NIST handbook of mathematical functions*. Cambridge university press, New York, USA, 2010.

[29] Andrea Alu and Nader Engheta. How does zero forward-scattering in magnetodielectric nanoparticles comply with the optical theorem? *Journal of Nanophotonics*, 4(1):1–18, may 2010.

[30] Roger F Harrington. *Field computation by moment methods*. Wiley-IEEE Press, 1993.

[31] Zhichao Ruan and Shanhui Fan. Superscattering of light from subwavelength nanostructures. *Phys. Rev. Lett.*, 105:013901, Jun 2010.

[32] Craig F Bohren and Donald R Huffman. *Absorption and scattering of light by small particles*. John Wiley & Sons, New York, USA, 2008.

[33] Herch Moyses Nussenzveig. *Causality and dispersion relations*. Academic Press, 1972.

[34] Roger G Newton. Optical theorem and beyond. *American Journal of Physics*, 44(7):639–642, jul 1976.

[35] Ronald M Foster. A reactance theorem. *Bell System technical journal*, 3(2):259–267, 1924.

[36] A Chen and F Monticone. Active Scattering-Cancellation Cloaking: Broadband Invisibility and Stability Constraints. *IEEE Transactions on Antennas and Propagation*, 68(3):1655–1664, 2020.

[37] Hendrik Wade Bode. *Network analysis and feedback amplifier design*. David Van Nostrand, New York, USA, 1945.

[38] Robert M Fano. Theoretical limitations on the broadband matching of arbitrary impedances. *Journal of the Franklin Institute*, 249(1):57–83, 1950.

[39] David M Pozar. *Microwave engineering*. John Wiley & Sons, New York, USA, 2009.

[40] Dimitrios L Sounas and Andrea Alù. Non-reciprocal photonics based on time modulation. *Nature Photonics*, 11(12):774–783, 2017.

[41] Tomohiro Amemiya, Masato Taki, Toru Kanazawa, Takuo Hiratani, and Shigehisa Arai. Optical lattice model toward nonreciprocal invisibility cloaking. *IEEE Journal of Quantum Electronics*, 51(3):1–10, 2015.

[42] S Darlington. Synthesis of Reactance 4-Poles Which Produce Prescribed Insertion Loss Characteristics: Including Special Applications To Filter Design. *Journal of Mathematics and Physics*, 18(1-4):257–353, apr 1939.

[43] A Chen, F Monticone, and A Alù. Invisible near-field probes at infrared frequencies based on impedance engineering at the nanoscale. In *2017 IEEE International Symposium on Antennas and Propagation & USNC/URSI National Radio Science Meeting*, pages 1055–1056, 2017.

[44] Romain Fleury, Francesco Monticone, and Andrea Alù. Invisibility and Cloaking: Origins, Present, and Future Perspectives. *Phys. Rev. Applied*, 4(3):37001, sep 2015.

[45] Ulf Leonhardt. Optical Conformal Mapping. *Science*, 312(5781):1777–1780, 2006.

[46] Vladimir M Shalaev. Transforming Light. *Science*, 322(5900):384–386, 2008.

[47] Huanyang Chen, C T Chan, and Ping Sheng. Transformation optics and metamaterials. *Nature Materials*, 9:387, apr 2010.

[48] Andrea Alù and Nader Engheta. Plasmonic materials in transparency and cloaking problems: mechanism, robustness, and physical insights. *Opt. Express*, 15(6):3318–3332, mar 2007.

[49] Andrea Alù. Mantle cloak: Invisibility induced by a surface. *Phys. Rev. B*, 80(24):245115, dec 2009.

[50] Pai-Yen Chen and Andrea Alù. Mantle cloaking using thin patterned metasurfaces. *Phys. Rev. B*, 84(20):205110, nov 2011.

[51] Andrea Alù and Nader Engheta. Cloaking a Sensor. *Phys. Rev. Lett.*, 102(23):233901, jun 2009.

[52] Andrea Alù and Nader Engheta. Cloaked near-field scanning optical microscope tip for noninvasive near-field imaging. *Physical Review Letters*, 105(26):1–4, 2010.

[53] A Monti, J Soric, A Alu, F Bilotti, A Toscano, and L Vegni. Overcoming Mutual Blockage Between Neighboring Dipole Antennas Using a Low-Profile Patterned Metasurface. *IEEE Antennas and Wireless Propagation Letters*, 11:1414–1417, 2012.

[54] J C Soric, A Monti, A Toscano, F Bilotti, and A Alù. Dual-Polarized Reduction of Dipole Antenna Blockage Using Mantle Cloaks. *IEEE Transactions on Antennas and Propagation*, 63(11):4827–4834, 2015.

[55] Tatiana V Teperik and André de Lustrac. Electromagnetic cloak to restore the antenna radiation patterns affected by nearby scatter. *AIP Advances*, 5(12):127225, dec 2015.

[56] Alessio Monti, Jason Soric, Mirko Barbuto, Davide Ramaccia, Stefano Vellucci, Fabrizio Trotta, Andrea Alù, Alessandro Toscano, and Filiberto Bilotti. Mantle cloaking for co-site radio-frequency antennas. *Applied Physics Letters*, 108(11):113502, mar 2016.

[57] David A B Miller. On perfect cloaking. *Opt. Express*, 14(25):12457–12466, dec 2006.

[58] Huanyang Chen, Zixian Liang, Peijun Yao, Xunya Jiang, Hongru Ma, and C T Chan. Extending the bandwidth of electromagnetic cloaks. *Phys. Rev. B*, 76(24):241104, dec 2007.

[59] Baile Zhang, Bae-Ian Wu, Hongsheng Chen, and Jin Au Kong. Rainbow and Blueshift Effect of a Dispersive Spherical Invisibility Cloak Impinged On by a Nonmonochromatic Plane Wave. *Phys. Rev. Lett.*, 101(6):63902, aug 2008.

[60] Andrea Alù and Nader Engheta. Effects of size and frequency dispersion in plasmonic cloaking. *Phys. Rev. E*, 78(4):45602, oct 2008.

[61] Efthymios Kallos, Christos Argyropoulos, Yang Hao, and Andrea Alù. Comparison of frequency responses of cloaking devices under non-monochromatic illumination. *Phys. Rev. B*, 84(4):45102, jul 2011.

[62] Francesco Monticone and Andrea Alù. Do Cloaked Objects Really Scatter Less? *Phys. Rev. X*, 3(4):41005, oct 2013.

[63] M Selvanayagam and G V Eleftheriades. An Active Electromagnetic Cloak Using the Equivalence Principle. *IEEE Antennas and Wireless Propagation Letters*, 11:1226–1229, 2012.

[64] Michael Selvanayagam and George V Eleftheriades. Experimental Demonstration of Active Electromagnetic Cloaking. *Phys. Rev. X*, 3(4):41011, nov 2013.

[65] Pai-Yen Chen, Christos Argyropoulos, and Andrea Alù. Broadening the Cloaking Bandwidth with Non-Foster Metasurfaces. *Phys. Rev. Lett.*, 111(23):233001, dec 2013.

[66] Lukas Novotny and Bert Hecht. *Principles of nano-optics*. Cambridge university press, 2012.

[67] Viktor A Podolskiy and Evgenii E Narimanov. Near-sighted superlens. *Optics Letters*, 30(1):75–77, 2005.

[68] Xing-Xiang Liu and Andrea Alu. Limitations and potentials of metamaterial lenses. *J. of Nanophotonics*, 5:53509–53514, 2011.

[69] E. H. Synge. A suggested model for extending microscopic resolution into the ultra-microscopic region. *Phil. Mag.*, 6:356–362, 1928.

[70] D. W. Pohl, W. Denk, and M. Lanz. Optical stethoscopy: Image recording with resolution $\lambda/20$. *Applied Physics Letters*, 44(7):651–653, 1984.

[71] A. Lewis, M. Isaacson, A. Harootunian, and A. Muray. Development of a 500 spatial resolution light microscope: I. light is efficiently transmitted through $\lambda/16$ diameter apertures. *Ultramicroscopy*, 13(3):227–231, jan 1984.

[72] Yasushi Inouye and Satoshi Kawata. Near-field scanning optical microscope with a metallic probe tip. *Opt. Lett.*, 19(3):159–161, feb 1994.

[73] E Betzig, J K Trautman, T D Harris, J S Weiner, and R L Kostelak. Breaking the Diffraction Barrier: Optical Microscopy on a Nanometric Scale. *Science*, 251(5000):1468–1470, 1991.

[74] Eric Betzig and Robert J Chichester. Single Molecules Observed by Near-Field Scanning Optical Microscopy. *Science*, 262(5138):1422–1425, 1993.

[75] Bert Hecht, Beate Sick, Urs P. Wild, Volker Deckert, Renato Zenobi, Olivier J.F. Martin, and Dieter W. Pohl. Scanning near-field optical microscopy with aperture probes: Fundamentals and applications. *Journal of Chemical Physics*, 112(18):7761–7774, apr 2000.

[76] M Burresi, D van Oosten, T Kampfrath, H Schoenmaker, R Heideman, A Leinse, and L Kuipers. Probing the Magnetic Field of Light at Optical Frequencies. *Science*, 326(5952):550–553, 2009.

[77] Lars Neumann, Yuanjie Pang, Amel Houyou, Mathieu L Juan, Reuven Gordon, and Niek F van Hulst. Extraordinary Optical Transmission Brightens Near-Field Fiber Probe. *Nano Letters*, 11(2):355–360, feb 2011.

[78] Youngkyu Lee, Andrea Alu, and John X J Zhang. Efficient apertureless scanning probes using patterned plasmonic surfaces. *Opt. Express*, 19(27):25990–25999, dec 2011.

[79] Caner Guclu, Mehdi Veysi, and Filippo Capolino. Photoinduced Magnetic Nanoprobe Excited by an Azimuthally Polarized Vector Beam. *ACS Photonics*, 3(11):2049–2058, nov 2016.

[80] Ruei-Han Jiang, Chi Chen, Ding-Zheng Lin, He-Chun Chou, Jen-You Chu, and Ta-Jen Yen. Near-Field Plasmonic Probe with Super Resolution and High Throughput and Signal-to-Noise Ratio. *Nano Letters*, dec 2017.

[81] Jian Yuan, Weiliang Ma, Lei Zhang, Yao Lu, Meng Zhao, Hongli Guo, Jin Zhao, Wenzhi Yu, Yupeng Zhang, Kai Zhang, Hui Ying Hoh, Xiaofeng Li, Kian Ping Loh, Shaojuan Li, Cheng-Wei Qiu, and Qiaoliang Bao. Infrared Nanoimaging Reveals the Surface Metallic Plasmons in Topological Insulator. *ACS Photonics*, 4(12):3055–3062, dec 2017.

[82] Pieter Neutens, Pol Van Dorpe, Iwijn De Vlaminck, Liesbet Lagae, and

Gustaaf Borghs. Electrical detection of confined gap plasmons in metal-insulator-metal waveguides. *Nature Photonics*, 3(5):283–286, apr 2009.

[83] R. Esteban, R. Vogelgesang, and K. Kern. Full simulations of the apertureless scanning near field optical microscopy signal: achievable resolution and contrast. *Optics Express*, 17(4):2518, feb 2009.

[84] Filiberto Bilotti, Francesco Pierini, and Lucio Vegni. Employment of metamaterial cloaks to enhance the resolution of near-field scanning optical microscopy systems based on aperture tips. *Metamaterials*, 5(2-3):119–124, 2011.

[85] Filiberto Bilotti, Simone Tricarico, Francesco Pierini, and Lucio Vegni. Cloaking apertureless near-field scanning optical microscopy tips. *Optics letters*, 36(2):211–213, jan 2011.

[86] Andrea Alù and Nader Engheta. Cloaking a receiving antenna or a sensor with plasmonic metamaterials. *Metamaterials*, 4(2):153–159, 2010.

[87] RA Waldron. Perturbation theory of resonant cavities. *Proceedings of the IEE-Part C: Monographs*, 107(12):272–274, 1960.

[88] A Femius Koenderink, Maria Kafesaki, Ben C Buchler, and Vahid Sandoghdar. Controlling the Resonance of a Photonic Crystal Microcavity by a Near-Field Probe. *Phys. Rev. Lett.*, 95(15):153904, oct 2005.

[89] Shumin Xiao, Vladimir P Drachev, Alexander V Kildishev, Xingjie Ni, Uday K Chettiar, Hsiao-Kuan Yuan, and Vladimir M Shalaev. Loss-free and active optical negative-index metamaterials. *Nature*, 466:735, aug 2010.

[90] O Hess, J B Pendry, S A Maier, R F Oulton, J M Hamm, and K L Tsakmakidis. Active nanoplasmonic metamaterials. *Nature Materials*, 11:573, jun 2012.

[91] Nikolay I Zheludev. The Road Ahead for Metamaterials. *Science*, 328(5978):582 LP – 583, apr 2010.

[92] Silvio Hrabar, Igor Krois, and Aleksandar Kiricenko. Towards active dispersionless ENZ metamaterial for cloaking applications. *Metamaterials*, 4(2):89–97, 2010.

[93] Silvio Hrabar, Igor Krois, Ivan Bonic, and Aleksandar Kiricenko. Negative capacitor paves the way to ultra-broadband metamaterials. *Applied Physics Letters*, 99(25):254103, dec 2011.

[94] E Ugarte-Munoz, S Hrabar, D Segovia-Vargas, and A Kiricenko. Stability of Non-Foster Reactive Elements for Use in Active Metamaterials and Antennas. *IEEE Transactions on Antennas and Propagation*, 60(7):3490–3494, 2012.

[95] Silvio Hrabar, Igor Krois, Ivan Bonic, and Aleksandar Kiricenko. Ultra-broadband simultaneous superluminal phase and group velocities in non-Foster epsilon-near-zero metamaterial. *Applied Physics Letters*, 102(5):54108, feb 2013.

[96] Amnon Yariv. *Quantum electronics*. Wiley, New York, USA, 1989.

[97] David C Burnham and Raymond Y Chiao. Coherent Resonance Fluorescence Excited by Short Light Pulses. *Phys. Rev.*, 188(2):667–675, dec 1969.

[98] Raymond Y Chiao. Superluminal (but causal) propagation of wave packets in transparent media with inverted atomic populations. *Phys. Rev. A*, 48(1):R34—-R37, jul 1993.

[99] Yi-Fan Chen, Peer Fischer, and Frank W Wise. Sign of the refractive index in a gain medium with negative permittivity and permeability. *Journal of the Optical Society of America B*, 23(1):45–50, 2006.

[100] Reza Safian, Mohammad Mojahedi, and Costas D Sarris. Asymptotic description of wave propagation in an active Lorentzian medium. *Phys. Rev. E*, 75(6):66611, jun 2007.

[101] Sergei Tretyakov. *Analytical modeling in applied electromagnetics*. Artech House, Norwood, MA, USA, 2003.

[102] A A Zyablovsky, A P Vinogradov, A V Dorofeenko, A A Pukhov, and A A Lisyansky. Causality and phase transitions in PT-symmetric optical systems. *Physical Review A*, 89(3):33808, 2014.

[103] Francesco Monticone, Constantinos A Valagiannopoulos, and Andrea Alù. Parity-Time Symmetric Nonlocal Metasurfaces: All-Angle Negative Refraction and Volumetric Imaging. *Phys. Rev. X*, 6(4):41018, oct 2016.

[104] Charles Herach Papas. *Theory of electromagnetic wave propagation*. Dover, New York, USA, 1988.

[105] J Mikulski and E Murphy. The computation of electromagnetic scattering from concentric spherical structures. *IEEE Transactions on Antennas and Propagation*, 11(2):169–177, 1963.

[106] COMSOL MULTIPHYSICS ver. 5.5, COMSOL AB, Stockholm, http://comsol.com.

[107] Francesco Monticone and Andrea Alu. Scattering at the Extreme with Metamaterials and Plasmonics. In *World Scientific Handbook of Metamaterials and Plasmonics*, World Scientific Series in Nanoscience and Nanotechnology, pages 295–335. World Scientific, jun 2017.

[108] J E Sipe and J Van Kranendonk. Macroscopic electromagnetic theory of resonant dielectrics. *Phys. Rev. A*, 9(5):1806–1822, may 1974.

[109] K L Tsakmakidis, O Reshef, E Almpanis, G P Zouros, E Mohammadi, D Saadat, F Sohrabi, N Fahimi-Kashani, D Etezadi, R W Boyd, and H Altug. Ultrabroadband 3D invisibility with fast-light cloaks. *Nature Communications*, 10(1):4859, 2019.

[110] Mohamed Ismail Abdelrahman, Zeki Hayran, Aobo Chen, and Francesco Monticone. Can fast-light cloaks achieve arbitrarily broadband invisibility? *arXiv preprint arXiv:2011.02333*, 2020.

[111] William Shockley and Hans J Queisser. Detailed Balance Limit of Efficiency of p-n Junction Solar Cells. *Journal of Applied Physics*, 32(3):510–519, mar 1961.

[112] Eli Yablonovitch. Statistical ray optics. *J. Opt. Soc. Am.*, 72(7):899–907, jul 1982.

[113] C H Henry. Limiting efficiencies of ideal single and multiple energy gap terrestrial solar cells. *Journal of Applied Physics*, 51(8):4494–4500, 1980.

[114] Zongfu Yu, Aaswath Raman, and Shanhui Fan. Fundamental limit of nanophotonic light trapping in solar cells. *Proceedings of the National Academy of Sciences*, 107(41):17491–17496, 2010.

[115] V Ganapati, O D Miller, and E Yablonovitch. Light Trapping Textures Designed by Electromagnetic Optimization for Subwavelength Thick Solar Cells. *IEEE Journal of Photovoltaics*, 4(1):175–182, jan 2014.

[116] Reference Solar Spectral Irradiance: ASTM G-173.

[117] H. John Caulfield and Shlomi Dolev. Why future supercomputing requires optics. *Nature Photonics*, 4(5):261–263, 2010.

[118] David A B Miller. Are optical transistors the logical next step? *Nature Photonics*, 4:3, jan 2010.

[119] Daniel R. Solli and Bahram Jalali. Analog optical computing. *Nature Photonics*, 9(11):704–706, oct 2015.

[120] B Jalali and A Mahjoubfar. Tailoring Wideband Signals With a Photonic Hardware Accelerator. *Proceedings of the IEEE*, 103(7):1071–1086, 2015.

[121] Nanfang Yu, Patrice Genevet, Mikhail A Kats, Francesco Aieta, Jean-Philippe Tetienne, Federico Capasso, and Zeno Gaburro. Light Propagation with Phase Discontinuities: Generalized Laws of Reflection and Refraction. *Science*, 334(6054):333–337, 2011.

[122] Y Zhao, M A Belkin, and A Alù. Twisted optical metamaterials for planarized ultrathin broadband circular polarizers. *Nature Communications*, 3:870, may 2012.

[123] Francesco Monticone, Nasim Mohammadi Estakhri, and Andrea Alù. Full Control of Nanoscale Optical Transmission with a Composite Metascreen. *Phys. Rev. Lett.*, 110(20):203903, may 2013.

[124] Carl Pfeiffer and Anthony Grbic. Metamaterial Huygens' Surfaces: Tailoring Wave Fronts with Reflectionless Sheets. *Phys. Rev. Lett.*, 110(19):197401, may 2013.

[125] Leonid L Doskolovich, Dmitry A Bykov, Evgeni A Bezus, and Victor A Soifer. Spatial differentiation of optical beams using phase-shifted Bragg grating. *Opt. Lett.*, 39(5):1278–1281, mar 2014.

[126] Sajjad AbdollahRamezani, Kamalodin Arik, Amin Khavasi, and Zahra Kavehvash. Analog computing using graphene-based metalines. *Opt. Lett.*, 40(22):5239–5242, nov 2015.

[127] Anders Pors, Michael G Nielsen, and Sergey I Bozhevolnyi. Analog Computing Using Reflective Plasmonic Metasurfaces. *Nano Letters*, 15(1):791–797, jan 2015.

[128] Ata Chizari, Sajjad Abdollahramezani, Mohammad Vahid Jamali, and Jawad A Salehi. Analog optical computing based on a dielectric meta-reflect array. *Opt. Lett.*, 41(15):3451–3454, aug 2016.

[129] Amir Youssefi, Farzad Zangeneh-Nejad, Sajjad Abdollahramezani, and Amin Khavasi. Analog computing by Brewster effect. *Opt. Lett.*, 41(15):3467–3470, aug 2016.

[130] Tengfeng Zhu, Yihan Zhou, Yijie Lou, Hui Ye, Min Qiu, Zhichao Ruan, and Shanhui Fan. Plasmonic computing of spatial differentiation. *Nature Communications*, 2017.

[131] Wenhui Wu, Wei Jiang, Jiang Yang, Shaoxiang Gong, and Yungui Ma. Multilayered analog optical differentiating device: performance analysis on structural parameters. *Opt. Lett.*, 42(24):5270–5273, dec 2017.

[132] Yisheng Fang, Yijie Lou, and Zhichao Ruan. On-grating graphene surface plasmons enabling spatial differentiation in the terahertz region. *Opt. Lett.*, 42(19):3840–3843, oct 2017.

[133] Cheng Guo, Meng Xiao, Momchil Minkov, Yu Shi, and Shanhui Fan. Photonic crystal slab Laplace operator for image differentiation. *Optica*, 5(3):251–256, mar 2018.

[134] Weixuan Zhang, Che Qu, and Xiangdong Zhang. Solving constant-coefficient differential equations with dielectric metamaterials. *Journal of Optics*, 18(7):75102, 2016.

[135] Sajjad Abdollahramezani, Ata Chizari, Ali Eshaghian Dorche, Mohammad Vahid Jamali, and Jawad A Salehi. Dielectric metasurfaces solve differential and integro-differential equations. *Opt. Lett.*, 42(7):1197–1200, apr 2017.

[136] Nasim Mohammadi Estakhri, Brian Edwards, and Nader Engheta. Inverse-designed metastructures that solve equations. *Science*, 363(6433):1333 LP – 1338, mar 2019.

[137] Nasim Mohammadi Estakhri, Brian Edwards, and Nader Engheta. Solv-

ing Integral Equations with Optical Metamaterial-Waveguide Networks. In *Conference on Lasers and Electro-Optics*, page FTh1G.2. Optical Society of America, 2017.

[138] Gordon Wetzstein, Aydogan Ozcan, Sylvain Gigan, Shanhui Fan, Dirk Englund, Marin Soljačić, Cornelia Denz, David A B Miller, and Demetri Psaltis. Inference in artificial intelligence with deep optics and photonics. *Nature*, 588(7836):39–47, 2020.

[139] Igor Podlubny. *Fractional differential equations: an introduction to fractional derivatives, fractional differential equations, to methods of their solution and some of their applications*, volume 198. Elsevier, 1998.

[140] N Engheia. On the role of fractional calculus in electromagnetic theory. *IEEE Antennas and Propagation Magazine*, 39(4):35–46, 1997.

[141] Amnon Yariv and Pochi Yeh. Photonics: optical electronics in modern communications (the oxford series in electrical and computer engineering). *Oxford University Press, Inc*, 231:232, 2006.

[142] David Mendlovic and Haldun M Ozaktas. Fractional Fourier transforms and their optical implementation: I. *J. Opt. Soc. Am. A*, 10(9):1875–1881, sep 1993.

[143] Haldun M Ozaktas and David Mendlovic. Fractional Fourier transforms and their optical implementation. II. *J. Opt. Soc. Am. A*, 10(12):2522–2531, dec 1993.

[144] Max Born and Emil Wolf. *Principles of Optics: Electromagnetic Theory of Propagation, Interference and Diffraction of Light*. Cambridge University Press, Cambridge, 7 edition, 1999.

[145] Joseph Goodman. *Introduction to Fourier optics*. McGraw-hill, 2008.

[146] David J Griffiths and Darrell F Schroeter. *Introduction to quantum mechanics*. Cambridge University Press, 2018.

[147] Philippe Lalanne and Pierre Chavel. Metalenses at visible wavelengths: past, present, perspectives. *Laser & Photonics Reviews*, 11(3):1600295, may 2017.

[148] Lingling Huang, Xianzhong Chen, Holger Mühlenbernd, Guixin Li, Benfeng Bai, Qiaofeng Tan, Guofan Jin, Thomas Zentgraf, and Shuang Zhang. Dispersionless Phase Discontinuities for Controlling Light Propagation. *Nano Letters*, 12(11):5750–5755, nov 2012.

[149] Dianmin Lin, Pengyu Fan, Erez Hasman, and Mark L Brongersma. Dielectric gradient metasurface optical elements. *Science*, 345(6194):298–302, 2014.

[150] Amir Arbabi, Yu Horie, Mahmood Bagheri, and Andrei Faraon. Dielectric metasurfaces for complete control of phase and polarization with subwavelength spatial resolution and high transmission. *Nature Nanotechnology*, 10(11):937–943, 2015.

[151] Mohammadreza Khorasaninejad, Wei Ting Chen, Robert C Devlin, Jaewon Oh, Alexander Y Zhu, and Federico Capasso. Metalenses at visible wavelengths: Diffraction-limited focusing and subwavelength resolution imaging. *Science*, 352(6290):1190 LP – 1194, jun 2016.

[152] Shuming Wang, Pin Chieh Wu, Vin-Cent Su, Yi-Chieh Lai, Mu-Ku Chen, Hsin Yu Kuo, Bo Han Chen, Yu Han Chen, Tzu-Ting Huang, Jung-Hsi Wang, Ray-Ming Lin, Chieh-Hsiung Kuan, Tao Li, Zhenlin Wang, Shining Zhu, and Din Ping Tsai. A broadband achromatic metalens in the visible. *Nature Nanotechnology*, 13(3):227–232, 2018.

[153] Wei Ting Chen, Alexander Y Zhu, Vyshakh Sanjeev, Mohammadreza Khorasaninejad, Zhujun Shi, Eric Lee, and Federico Capasso. A broadband achromatic metalens for focusing and imaging in the visible. *Nature Nanotechnology*, 13(3):220–226, 2018.

[154] Mohammadreza Khorasaninejad and Federico Capasso. Metalenses: Versatile multifunctional photonic components. *Science*, 358(6367), 2017.

[155] Sourangsu Banerji, Monjurul Meem, Apratim Majumder, Fernando Guevara Vasquez, Berardi Sensale-Rodriguez, and Rajesh Menon. Imaging with flat optics: metalenses or diffractive lenses? *Optica*, 6(6):805–810, 2019.

[156] Jacob Engelberg, Chen Zhou, Noa Mazurski, Jonathan Bar-David, Anders Kristensen, and Uriel Levy. Near-IR wide-field-of-view Huygens metalens for outdoor imaging applications. *Nanophotonics*, 9(2):361–370, 2020.

[157] Orad Reshef, Michael P DelMastro, Katherine KM Bearne, Ali H Alhulaymi, Lambert Giner, Robert W Boyd, and Jeff S Lundeen. Towards ultra-thin imaging systems: an optic that replaces space. *arXiv preprint arXiv:2002.06791*, 2020.

[158] Cheng Guo, Haiwen Wang, and Shanhui Fan. Squeeze free space with nonlocal flat optics. *Optica*, 7(9):1133–1138, 2020.

[159] Hoyeong Kwon, Dimitrios Sounas, Andrea Cordaro, Albert Polman, and Andrea Alù. Nonlocal Metasurfaces for Optical Signal Processing. *Phys. Rev. Lett.*, 121(17):173004, oct 2018.

[160] Hermann A Haus. *Waves and fields in optoelectronics*. Prentice-Hall, Englewood Cliffs, New Jersey, 1984.

[161] W. M. Mumford. Maximally flat filters in waveguides. *Bell Syst. Tech. J.*, 27:684–714, 1948.

[162] A S Podgorski and R H Macphie. Quarter-Wavelength Coupled Dielectric Plate Resonators for High Selectivity TE/sub 10/-Mode Filters. *IEEE Transactions on Microwave Theory and Techniques*, 28(4):405–408, 1980.

[163] Boris Gralak, Michel Lequime, Myriam Zerrad, and Claude Amra. Phase retrieval of reflection and transmission coefficients from Kramers–Kronig relations. *J. Opt. Soc. Am. A*, 32(3):456–462, mar 2015.

[164] Hugh Angus Macleod. *Thin-Film Optical Filters*. Series in optics and optoelectronics. CRC Press, Boca Raton, FL, fifth edition edition, 2018.

[165] A. Chen and F. Monticone. Broadband absorption limits for ultrathin solar cells. In *2020 Fourteenth International Congress on Artificial Materials for Novel Wave Phenomena (Metamaterials)*, pages 183–185, 2020.

[166] Aobo Chen and Francesco Monticone. Truly solid-state flat optics with dielectric nonlocal metasurfaces. *arXiv preprint arXiv:2012.08613*, 2020.

[167] Nader Engheta. Metamaterials with high degrees of freedom: space, time, and more. *Nanophotonics*, 10(1):639–642, 2021.

[168] Zeki Hayran, Aobo Chen, and Francesco Monticone. Spectral causality and the scattering of waves. *arXiv preprint arXiv:2012.15796*, 2020.

[169] Lumotive, http://www.lumotive.com/.

[170] metalenz, http://www.metalenz.com/.

[171] Oblate Optics, https://www.oblateoptics.com/.

[172] Lightmatter, https://lightmatter.co/.